Experimental Investigation of Turbulence under the Influence of Confinement and Rotation

Vom Fachbereich Maschinenbau
an der Technischen Universität Darmstadt
zur
Erlangung des Grades eines Doktor-Ingenieurs (Dr.-Ing.)
genehmigte

D i s s e r t a t i o n

vorgelegt von

Dipl.-Ing. Matthias Kinzel

geb. in Frankenberg (Eder)

Berichterstatter:	Prof. Dr.-Ing. C. Tropea
Mitberichterstatter:	Prof. Dr.-Ing. W. Kinzelbach
Tag der Einreichung:	26.01.2010
Tag der mündlichen Prüfung:	31.03.2010

Darmstadt 2010
D17

Hiermit versichere ich, die vorliegende Doktorarbeit unter der Betreuung von Prof. Dr.-Ing. C. Tropea nur mit den angegebenen Hilfsmitteln selbständig angefertigt zu haben.

Darmstadt, den 25.01.2010

Abstract

In this thesis shear-free turbulence under the influence of confinement and rotation has been analyzed experimentally via Particle Image Velocimetry (PIV) and three-dimensional Particle Tracking Velocimetry (3D-PTV). The measurements have been carried out in a water tank placed on a rotating table in which the flow is mechanically forced from the top by an oscillating grid. 3D-PTV measurements were conducted in two different volume sizes, namely a large observation volume allowing to capture the large scale motions of the flow and a small observation volume, in which the spatial resolution was sufficient to assess all nine components of the velocity gradient tensor. One of the main achievements of this work is the simultaneous measurement in the large and small observation volume using two synchronized PTV systems and two types of seeding particles.

The spreading of turbulence has been investigated experimentally for three different cases, i.e. (i) free turbulent diffusion and spreading of turbulence under (ii) the influence of confinement and (iii) rotation and compared to the theoretical results of Oberlack and Günther (2003). In particular, for case (i) we observe that the turbulent/non-turbulent interface propagates according to a power law, $H \propto t^n$, where n is estimated to be $n = 0.6 \pm 0.1$. For case (ii) we confirm that the behavior changes to a logarithmic law with $H \propto \ell_c ln(t - t_0) + y_0$. Finally, for case (iii) we confirm the theory only in the sense that turbulence remains confined within a finite domain.

The flow was observed to change drastically under the influence of rotation. In particular it was found that the 3D turbulent flow remains confined to a distances $y < y^*$ and becomes quasi-2D for larger distances from the grid. The analysis of the region between the 3D and quasi-2D flow shows that the transition from one flow state to the other is more gradual and not as abrupt as for the turbulent/non-turbulent interface, which occurs in the free turbulent diffusion without rotation. The study of the alignments, which are formed by the rotation confirms that the quasi-2D regime is dominated by columnar vortices. A closer examination has demonstrated that this region can be divided into three parts: (i) the core of the vortex columns, (ii) the outer region of the vortex columns and (iii) the flow in-between the columnar structures. Fluid is transported upwards in cyclones and downwards in anticyclones due to Ekman pumping, while the velocity is primarily orientated normal to the rotation axis in the outer regions of the vortex columns and hence exhibits a quasi-2D flow pattern. In the intermediate region the flow remains three-dimensional. Both enstrophy and strain were found to be depleted under the influence of rotation. High levels of enstrophy seem to be confined to the regions of the vortex cores while regions of high strain are predominately located in the intermediate region. Vortex stretching also occurs less frequently and the ratio of vortex stretching to compression changes and can become even smaller than one within the columnar vortices. Also, the positive skewness of the Λ_2-PDF, which is characteristic for 3D-turbulence is nearly vanished in the quasi-2D regime. It was also found that generally these effects become stronger with angular velocity.

Kurzfassung

Diese Arbeit befasst sich mit Turbulenz ohne mittlerer Scherung unter dem Einfluss von räumlicher Begrenzung der Domäne und externer Rotation. Dafür wurden Particle Image Velocimetry (PIV) und dreidimensionale Particle Tracking Velocimetry (3D-PTV) Messungen in einem Wassertank auf einem rotierenden Tisch durchgeführt. Die Strömung wurde durch ein oszillierendes Gitter am oberen Tankende angeregt. Die 3D-PTV Experimente wurden mit zwei verschieden großen Messvolumen durchgeführt, um einerseits die großskaligen Strömungsmerkmale aufzuzeichnen und andererseits gleichzeitig alle neun Komponenten des Geschwindigkeitsgradiententensors zu erhalten. Eine große Weiterentwicklung ist dabei, dass beide Messungen simultan durchgeführt wurden, indem zwei PTV Systeme mit einander synchronisiert und zwei verschiedene Arten von Seedingpartikeln eingesetzt wurden.

Um die theoretische Analyse von Oberlack and Günther (2003) zu validieren, wurde die Ausbreitung der Turbulenz wurde für drei Fälle untersucht: (i) freie turbulente Diffusion und die Ausbreitung unter dem Einfluss von (ii) räumlicher Begrenzung und (iii) Rotation. Die Messungen zeigen, dass sich die Grenzfläche, welche turbulente von nicht-turbulenten Bereichen trennt, im Fall (i) nach einem Potenzgesetz, $H \propto t^n$ mit $n = 0.6 \pm 0.1$, fortbewegte. Für den Fall (ii) können wir bestätigen, dass sich das Ausbreitungsverhalten zu einem logarithmischen Gesetz mit $H \propto \ell_c ln(t - t_0) + y_0$ ändert. Im Fall (iii) bestätigen wir die Theorie nur in soweit, dass die Turbulenz auf den gitternahen Bereich beschränkt bleibt.

Die Strömung ändert sich drastisch unter dem Einfluss von Rotation. Der 3D-turbulente Teil bleibt auf die Entfernung $y < y^*$ vom Gitter begrenzt und verändert sich danach zu einer quasi-2D Strömung. Der Übergang zwischen den beiden Bereichen nicht abrupt, wie bei der Grenzfläche zwischen turbulenten und nicht-turbulenten Bereichen im Fall ohne Rotation. Eine Analyse der Ausrichtungen, die durch die Rotation verursacht werden, bestätigt, dass der quasi-2D Bereich hauptsächlich aus Wirbelröhren besteht. Bei näherer Betrachtung kann eine Unterteilung in drei Bereiche vorgenommen werden: (i) das Zentrum der Wirbelröhren, (ii) deren äußerer Bereich und (iii) die Region zwischen den Röhren. Fluid wird in Zyklonen nach oben und in Antizyklonen nach unten transportiert, während die Geschwindigkeit in den äußeren Bereichen der Wirbel näherungsweise senkrecht zur Rotationsachse ausgerichtet ist. Die Strömung zwischen den Wirbelröhren weist einen höheren Grad an Dreidimensionalität auf. Sowohl Enstrophy als auch Spannungen fallen unter dem Einfluss von Rotation ab. Bereiche, in denen die Enstrophy hoch ist, befinden sich vornehmlich im Zentrum der Wirbelröhren, während Bereich mit hohen Spannungen eher zwischen den Röhren auftreten. Wirbelstreckung wird reduziert und das Verhältnis von Wirbelstreckung zu -stauchung ändert sich dahingehend, dass es im Bereich der Wirbelröhren sogar kleiner als eins werden kann. Außerdem verschwindet die positive Schiefe der Λ_2-PDF, die eine Charakteristik von 3D-turbulenten Strömungen ist, fast vollständig. Im allgemeinen verstärken sich die Effekte, die durch die Rotation entstehen, wenn die Drehgeschwindigkeit erhöht wird.

Danksagung

Diese Arbeit ist im Rahmen des Schwerpunktprogramms 1147 ‘Bildgebende Messtechnik’ und des Forschungsantrages DFG 1941/37-1 ‘Turbulente Diffusion: Direkte Numerische Simulation, Modellierung und Experimentelle Untersuchung’ der Deutschen Forschungsgesellschaft finanziert worden.

Als erstes möchte ich Prof. Dr.-Ing. Cameron Tropea und Prof. Dr.-Ing. Wolfgang Kinzelbach für ihre Unterstützung bei dieser Arbeit danken. Beide haben mir großes Vertrauen entgegengebracht, mir Freiräume in meiner Forschung gewährt und waren dennoch jederzeit als Ansprechpartner für mich da. Ein weiterer Dank gebührt Prof. Dr.-Ing. Martin Oberlack und Prof. Dr. Akardy Tsinober für ihre Ratschläge und Erklärungen auf dem Gebiet der Turbulenzforschung.

Diese Arbeit wäre ohne die Anleitung und Hilfe von Dr.-Ing. Markus Holzner und Dr.-Ing. Beat Lüthi nicht möglich gewesen. Ich bin ihnen tief verbunden und möchte mich an dieser Stelle für ihre Unterstützung sowohl im Labor, als auch bei der theoretischen Arbeit, herzlich bedanken. Dies gilt auch für Dr.-Ing. Holger Nobach, der mich besonders im Bereich der Datenanalyse unterstützt hat und Dr.-Ing. Alexander Liberzon, der beim experimentellen Teil der Arbeit mitgewirkt hat.

Ich hatte das Glück mit einigen fähigen Studenten zusammenzuarbeiten, die mich als Hilfswissenschaftler und Diplomarbeiter unterstützt haben. Mein Dank gilt hier vor allem Dipl.-Ing. Marc Wolf, cand.-Ing. Dominik Krug, Tim Prangemeier, Miklos Galamb und Brian Jeffery.

Auch bei meinen Kollegen möchte ich mich für die gute Zusammenarbeit über die Jahre bedanken. Dies gilt sowohl für die Mitarbeiter der Werkstätten, hier vor allem Ilona Kaufhold, Toni Blunschi, Thomi Keller und Ernst Bleiker, als auch Dr. rer. nat. Hubert Marschall, Dr.-Ing Benjamin Balewski, Dr.-Ing. Nils van Hinsberg, Dipl.-Ing. Emir Sirbubalo, Dipl.-Ing. Gisa Kadavelil und Dipl.-Ing. Robert Maduta. An dieser Stelle möchte ich besonders Dr.-Ing. David E. Rival und Dipl.-Ing. Jochen Kriegseis für ihre Unterstützung und Kameradschaft danken. Die vielen Stunden, die wir mit Diskussionen, Sport und in der Wildnis verbracht haben, werden mir fehlen.

Zum Schluss möchte ich mich bei meinen Freunden und Familie für die Unterstützung und Geduld, die sie über die Jahre aufgebracht haben, bedanken.

Contents

List of Figures

List of Tables

Nomenclature

Symbol	Unit	Description
a	$\mathrm{m/s^2}$	Lagrangian acceleration
a_c	$\mathrm{m/s^2}$	convective acceleration
a_{cl}	$\mathrm{m/s^2}$	Coriolis acceleration
a_l	$\mathrm{m/s^2}$	local acceleration
Ar	-	Argon
B	-	constant of order unity
$curv$	$\mathrm{m^{-1}}$	curvature
d	m	bar diameter
d_0	m	mesh size
d_p	m	particle diameter
D	m	tube diameter
Ek	-	Ekman number
F_k	N	forcing
$H(t)$	m	mean position of the turbulent/non-turbulent interface
k_0	$\mathrm{m^2/s^2}$	kinetic energy in proximity of the grid
$k_\perp$	$\mathrm{m^2/s^2}$	kinetic energy in direction perpendicular to grid
$k_\parallel$	$\mathrm{m^2/s^2}$	kinetic energy in direction parallel to grid
ℓ	m	integral length scale
ℓ_0	m	integral length scale in proximity of the grid
ℓ_c	m	confinement length scale
L	m	characteristic length scale
M	-	measurement point
N	-	number of data
p	$\mathrm{N/m^2}$	pressure
P	-	arbitrary point
P	-	first invarient of $\partial u_i/\partial x_j$
q	-	arbitrary quantity
Q	-	second invarient of $\partial u_i/\partial x_j$
r	m	distance between two correlation points
R	-	third invarient of $\partial u_i/\partial x_j$
R	m	radial distance from vortex core
R	-	regression quality
$R_ii(r,t)$	-	autocorrelation function
$R_ij(r,t)$	-	two-point correlation function
Re	-	Reynolds number
Re_λ	-	Taylor micro scale Reynolds number
Ro	-	Rossby number
s_{ij}	$\mathrm{s^{-1}}$	rate of strain tensor
s^2	$\mathrm{s^{-2}}$	total strain

St	-	Stokes number
t	s	time
t_0	s	starting time
		virtual origin in time
u	m/s	velocity vector
u_{hor}	m/s	horizontal velocity component
u_m	m/s	velocity at measurement point M
u_{ver}	m/s	vertical velocity component
u_{rms}	m/s	root mean square velocity
$u^{'}$	m/s	fluctuating velocity
W	s^{-4}	vortex stretching vector
X, x	m	horizontal direction parallel to the grid
Y, y	m	vertical direction normal to the grid
y_0	m	virtual origin in space
y^*	m	equilibrium depth
Z, z	m	span-wise direction parallel to the grid

Greek Letters

Symbol	Unit	Description
α	-	regression parameter
α	$s^{-2}t^{-1}$	rate of enstrophy production
β	-	regression parameter
δ	-	regression parameter
δ	m	thickness of Ekmann layer
ϵ	m	grid amplitude
ϵ	s^{-4}	mean dissipation
$\epsilon_i jk$	-	Levi Civita tensor
Γ_1	-	angular momentum of velocity
Γ_2	-	second Galilean invariante
η	m	Kolmogorov length scale
λ	m	Taylor micro scale
λ_i	-	eigenvectors of the rate of strain tensor
Λ_i	-	eigenvalues of the rate of strain tensor
ρ_f	kg/m^3	fluid density
ρ_p	kg/m^3	particle density
ν	m^2/s	kinematic viscosity
τ_p	s	particle response time
τ_η	s	Kolmogorov timescale
τ_Ω	s	timescale of system rotation
ω	s^{-1}	vorticity
ω^2	s^{-2}	enstrophy
Ω	rad/s	angular velocity

Subscripts

Symbol	Description
i, j, k	indices
m, n	exponents
x, y, z	derivative with respect to x,y or z

Abbreviations

Symbol	Description
2D	two-dimensional
3D	three-dimensional
CAD	computer aided design
cos	cosine
DNS	direct numerical simulations
exp	exponential
log	logarithmic
LHS	left hand side
No.	number
PDF	probability density function
PIV	Particle Image Velocimetry
PTV	Particle Tracking Velocimetry
rms	root mean square
RHS	right hand side
STS	simultaneous two scale
TNTI	turbulent/non-turbulent interface
Tomo	tomographic

1 Introduction

The riddle of turbulence has puzzled scientists since the first studies by Leonardo da Vinci at the end of the 15th century. However, turbulence is still not fully understood and remains one of the last unsolved problems of classical physics (see, Feynman et al. (1963)). The majority of studies aimed at the understanding of turbulence have focused on rather simplified and ideal situations, e.g., homogeneous and isotropic turbulence. However, the aim of this thesis is to add to the understanding of some specific, but fundamentally and practically very important aspects. Namely, shear-free turbulence under the influence of confinement and rotation has been analyzed experimentally. The present Section provides a short review of the literature relevant for this work. It starts out with an overview on the spreading of turbulence under the influence of confinement and rotation with the focus on scaling relations. After that a general overview of previous work on the influence of system rotation on turbulence is given.

1.1 The Spreading of Turbulence

Many flows observed in nature are partly turbulent, e.g. Scorer (1978), where the turbulent regions are separated from surrounding irrotational (non-turbulent) regions by a sharp interface, the so-called turbulent/non-turbulent interface (TNTI). Common examples are smoke plumes from chimneys, jets from pollution outlets, clouds, volcanic eruptions and sea floor hydrothermal vents just to mention a few. Most pronounced is the behavior of the enstrophy, $\omega^2 = \omega_i\omega_i$, where ω_i (i=1,2,3) are the three components of the vorticity vector, which changes by orders of magnitude across the interface. A sudden change in the magnitudes of the velocity, u_i, and acceleration, a_i, is also observed (see, e.g., Westerweel et al. (2002), Holzner et al. (2007), Holzner et al. (2009)).

Typically in these flows the turbulence diffuses and the turbulent/non-turbulent interface advances into the ambient fluid, while fluid at rest is entrained into the turbulent flow regions. This mixing process is of importance, e.g., for the dispersion of contaminants. Spreading of turbulence is also important for industrial applications, such as combustion chambers, chemical technology, jets and wakes of aircraft and ships. Traditionally, most of the attention is paid to flows with significant mean shear, like canonical free shear flows (e.g., jets, wakes or mixing layers), see, e.g., Townsend (1976), Pope (2000) and Tsinober (2001).

This study focuses on the problem of shear-free turbulence that diffuses from a planar source of turbulent kinetic energy. Despite its fundamental importance, much less attention was dedicated to this problem compared to canonical shear flows. Hopfinger and Toly (1976) reported experiments, where shear-free turbulence was generated by a planar grid, which oscillated normally to its plane in a water tank. The flow produced by an oscillating grid is the result of interactions between the individual jets and wakes created by the motion of the grid bars. At a sufficient distance from the grid, these jets and wakes interact and break into turbulence that propagates away from the grid. Ideally, no mean flow exists and

the turbulence is considered nearly isotropic and homogeneous in planes parallel to the driving grid. The mean flow, which can arise in some of the experiments conducted within this study is briefly addressed in section 3.2.1. For the steady problem, Hopfinger and Toly (1976) (see also Silva and Fernando (1994) and references therein) measured that the r.m.s. velocity, u_{rms}, and the integral length scale, ℓ, change with the distance to the source, y, as $u_{rms} \propto y^{-1}$ and $\ell \propto y$. Hence the Reynolds Number, Re, does not change with distance from the grid. Based on dimensional analysis, Long (1978) predicted that the mean depth of the turbulent/non-turbulent interface, $H(t)$, grows in time, t, according to a power law $H(t) \propto t^{\frac{1}{2}}$. This was confirmed experimentally by Dickinson and Long (1978). In their studies, the turbulent/non-turbulent interface was detected visually from the recorded images. Recently, Holzner et al. (2006) used detailed flow measurements and a detection algorithm for the turbulent/non-turbulent interface to confirm the propagation law of $H \propto t^{\frac{1}{2}}$.

Spreading of Turbulence under the Influence of Confinement

Ideally, turbulence spreads into an undisturbed 'infinite' environment. However, most real flows do not develop freely, for example they can be bounded (by walls, stratification, etc.) so that there is an upper limit for the integral length scale, e.g., stratified layers in the ocean. A basis for this work is the Lie-group analysis of the infinite series of multi-point correlation equations performed by Oberlack and Günther (2003). Their main ideas are introduced in section 1.2 'New Scaling Laws'. For the spreading of turbulence under the influence of confinement their results yield a deceleration wave like solution. This means that $H(t) \propto ln(t - t_0)$ and thus a slower propagation of the turbulent/non-turbulent interface than in the case of turbulence, which diffuses freely from the source. Godeferd and Lollini (1998) simulated the influence of the walls in freely decaying turbulence using Direct Numerical Simulations, DNS, and found that the growth of the integral length scale is inhibited when compared to the non-confined case. They observed blocking of the integral length scale due to the finite size of the simulation domain and weaker vortex stretching in the direction normal to the walls.

While being present in many engineering applications, e.g., in the blade passages in turbo machinery, the effects of confinement are often negligible in comparison to the mean convection, temperature differences or buoyancy, which cause the flow to spread. Nevertheless for numerical simulations it is expensive to have large domains so that effects of confinement are often present in numerical results. Furthermore, as engineers are looking for the last 0.1% in efficiency in products like jet-engines, accounting for the effects of confinement becomes invariably more important.

Spreading of Turbulence under the Influence of Rotation

A second effect, which is commonly observed in turbulent flows in nature and engineering applications is the influence of system rotation, e.g., in meteorology or turbo machinery (see, e.g., Pedlosky (1987). However, the understanding of

this effect is currently incomplete, see for example the review by Hunt et al. (2006)

The spreading of turbulence under the influence of rotation was investigated in earlier experiments by Dickinson and Long (1982), who found that the propagation of the turbulent/non-turbulent interface can be described by a power law in the proximity of the energy source and then changes to a linear behavior further away. The transition from one regime to the other depends on the rotational velocity and occurs earlier in time with higher rotation rates. The linear regime is in agreement with the findings of Davidson et al. (2006) who also report a linear propagation in time of columnar vortices, which form and move away from the turbulent region when the flow is subject to system rotation. They attribute the spreading of energy to a transport mechanism associated with inertial waves.

1.2 New Scaling Laws

Oberlack and Günther (2003) studied shear-free turbulent diffusion applying Lie-group (symmetry) analysis to the infinite series of multi-point correlation equations. Their main results are briefly summarized here as they form the basis for the part of this study, which deals with the experimental investigation of spreading of turbulence. Oberlack and Günther (2003) consider turbulence, which is generated by a planar source of turbulent kinetic energy and diffuses normal to this plane, similar to the oscillating grid experiments described before. In agreement with the studies mentioned above they derived a diffusion like solution for the case in which turbulence diffuses freely into the adjacent calm fluid (hereafter referred to as case (i)). In their analysis they also found solutions for the case where the diffusion of the turbulent flow is hindered by an upper bound for the integral length scale (case (ii)) and the case when rotation is applied to the spreading flow (case (iii)). For the case influenced by confinement their results predict a deceleration wave like solution,i.e., $H(t) \propto ln(t - t_0)$. A finite domain solution, namely $H(t) \propto exp(-t/\tau_\Omega)$ on the other hand is their result for case (iii). Further details about the method used and the scaling laws, which were found for the propagation of the turbulent/non-turbulent interface for the three cases can be found in Appendix A.

Besides the above mentioned studies on turbulent diffusion there has been numerical work on the influence of confinement on the spreading of turbulence, e.g., Godeferd and Lollini (1998). This study provide experimental validation for the theoretical results of Oberlack and Günther (2003) and numerical results obtained by Godeferd and Lollini (1998). Therefore we have performed one shot experiments similar to those in which turbulence can diffuse freely but with the difference that the horizontal region in which the flow could spread out was confined by squared tubes of different diameters.

The influence, which rotation has on turbulent flows in general and spreading of turbulence in particular has been investigated both experimentally and numerically by Dickinson and Long (1982) and Davidson et al. (2006). They report a linear propagation in time for the spreading of turbulence under the in-

fluence of system rotation, i.e. for the formation of columnar vortices. Oberlack and Günther (2003) on the other hand investigated the spreading of turbulence under the influence of rotation theoretically and found a finite domain solution, namely that $H(t) \propto exp(-t/\tau_\Omega)$. We have performed experiments to investigate the difference between the experimental findings on the one hand and the predictions by Oberlack and Günther (2003) on the other. We focus on the two regimes found in the spreading velocity by Dickinson and Long (1982) and in the flow structure by Davidson et al. (2006), namely the 3D-turbulent flow in the proximity of the oscillating grid and the columnar structures, which form underneath.

1.3 Turbulence under the Influence of Rotation

Besides its influence on the spreading behavior of turbulence, system rotation has an impact on a number of other important features of turbulent flows. A well known (yet not completely understood) macroscopic effect of system rotation on turbulence is the appearance of large columnar structures (Hopfinger et al. (1982)). Extensive research, both experimentally (Hopfinger et al. (1982), Davidson et al. (2006), Morize et al. (2005)) and numerically (Godeferd and Lollini (1998), Mininni et al. (2009)) has been performed with focus on these structures that are commonly associated with a qualitative change of the flow from a three-dimensional to a more two-dimensional state. With higher Taylor micro scale Reynolds number, Re_λ, and rotational velocity, Ω, the number of columnar structures is known to increase, while their diameter decreases. Their formation has been associated with inertial waves, see, e.g., Hopfinger et al. (1982) and Davidson et al. (2006). According to Godeferd and Lollini (1998) an Ekman layer in which viscous forces and the Coriolis force are in equilibrium is formed at the interface with the solid boundaries, i.e. the bottom and side walls of the tank. The thickness of the Ekman layer is $\delta = \sqrt{\nu/\Omega}$ and the Ekman number is the ratio between the viscous and rotational forces, $Ek = \nu/\Omega L^2$, where ν is the kinematic viscosity of the fluid, Ω the angular velocity of rotation and L a characteristic macroscopic length scale of the flow. The rotational velocity of the columnar structures and the resulting pressure variation across the vortex column interact with the Ekman layer creating a vertical velocity component and a helical particle trajectory in the columnar vortices, see Godeferd and Lollini (1998). Depending on the direction of rotation of the vortex column this vertical velocity can be positive or negative. Thus fluid is transported upwards in cyclonic and downwards in anticyclonic columnar vortices. Asymmetry between cyclonic and anticyclonic vortices in rotating turbulence was found by Hopfinger et al. (1982) and confirmed by, e.g., Morize et al. (2005).

The formation of the columnar structures and the energy dispersion within and between them has been investigated in Davidson and Graham (2003) and Davidson et al. (2006). They showed that under the influence of rotation the axial component of angular momentum of a blob of vorticity disperses only along the rotation axis and stays confined in a cylinder the size of the original vortex blob. They calculate that the velocity decay is lower within the cylinder ($\propto$

t^{-1}) than outside ($\propto t^{-3/2}$) and that therefore the columnar structures become dominant. This mechanism even applies when the original vorticity of the blob is oriented normal to the axis of rotation. Less clear is the transition between the region of three dimensional turbulence and the region, which is dominated by the columnar structures. We want to add to the understanding of these columnar structures by measuring the three-dimensional velocity field as well as all components of the fully resolved velocity gradient tensor. This provides access to the Coriolis and Lagrangian acceleration together with quantities like vorticity and strain. We detect vortex columns in the quasi two-dimensional region of the flow and characterize them with respect to quantities associated with the large (e.g. velocity field and flow pattern) and small scale (e.g. vorticity and strain) structures of the flow.

Heijst and Clercx (2007) and van Bokhoven et al. (2009) worked on the behavior of both forced and decaying quasi-2D turbulent flows experimentally. Turbulence was forced electro-magnetically at the bottom of the experimental facility and they also found a reduction in the dissipation rate and a longer spatial and temporal correlation due to the influence of rotation. This reflects an increase in the integral length scales due to the Coriolis forces. In agreement with Hopfinger et al. (1982) they report that the flow statistics become independent of distance from the electro magnetic forcing for a local Rossby number smaller than 0.2. Furthermore, they found that the no-slip boundaries have a considerable effect on the flow, namely that vortex filaments, which were formed in the boundary layers are scraped off by neighboring vortices and transported into the interior of the quasi-2D flow. According to their experimental and numerical work this affects the evolution of the 2D flow region considerably also at larger distances from the walls. However, the focus in the work of Heijst and Clercx (2007) and van Bokhoven et al. (2009) is on the quasi-2D region of the flow and the columnar structures, which are dominant. In our measurements we focus on the aspect of how the flow field changes with distance from the energy source, especially with respect to how the transition from three- to two-dimensional flow occurs. Also the flow within the region, which is characterized by a low Rossby number, $Ro < 0.2$, is analyzed thoroughly, namely the regions of the vortex columns, their cores and the regions between the columns are characterized.

Within this thesis both evolving and stationary flows are investigated. Morize and Moisy (2006) on the other hand have performed groundbreaking experiments in the area of decaying turbulence, which shall be mentioned briefly. They looked at the decay of kinematic energy in grid generated turbulence in a rotating tank. They analyzed the decay rate with respect to Ro and found a transition from the classical $t^{-5/6}$ energy decay law to the $\Omega^{3/5}t^{-3/5}$ law proposed by Squires et al. (1994) at Ro=0.25. The research group reported a strong variation of the decay law even at low rotational velocities and attribute this to the increase in the integral length scale to the size of the experimental apparatus. This increase is explained using inertial wave theory, which Messio et al. (2008) further developed and validated using experiments with a small oscillating disk in a rotating water filled cylinder.

In Godeferd and Lollini (1998) two direct numerical simulations (DNS) are performed to analyze the effects of rotation on turbulent flows. In the first DNS they study freely decaying turbulence, with and without rotation. In this simulation they also considering the influence of walls on the evolution of the flow (see section 1.1 above). Their second DNS deals with a configuration similar to the experimental one of Hopfinger et al. (1982). For the rotating case they noted an increase in the correlation functions in the direction parallel to the rotation axis and a decrease perpendicular to it as well as a decrease in the energy transfer. In their results a correlation between the number of column vortices and the ratio Re/Ro (the inverse of the Ekman number) is apparent and the lifetime of the coherent structures increases with Re_λ. They also note an asymmetry between cyclonic and anticyclonic vortices and explain this observation using linear stability analysis for the case of isolated vortices, whereby anticyclones disappear due to their instability related to perturbations in the surrounding flow. These results are in agreement with the experimental findings of Heijst and Clercx (2007), van Bokhoven et al. (2009) and Morize and Moisy (2006).

Numerical results concerning turbulent scaling laws and energy transfer in rotating flow with Rossby numbers down to 0.03 and Reynolds numbers based on the Taylor micro scale of up to 1100 have been published by Mininni et al. (2009). They observed both a direct and an inverse cascade of energy for high enough rotation. The inverse cascade of energy is in $k_\perp$ direction and affects scales larger than the forcing scale, while the direct cascade of energy is present at smaller scales. As the Rossby number decreases the net flux to small scales decreases as well, while the amplitude of the flux to large scales increases. Mininni et al. (2009) found no inverse cascade in $k_\parallel$ direction.

We measure the full spatially resolved velocity gradient tensor with all its nine components. Thus we have the means to characterize the flow in a way it has not been done before, especially since we capture large and small scale quantities at the same time. This enables us to investigate how the predominant vortex stretching mechanism, i.e. positive mean enstrophy production, which is the motor of turbulence changes with the transition from three-dimensional turbulence in the proximity of the energy source to quasi-2D flow below. Within the quasi-2D flow differences in the enstrophy production are further analyzed for the regions of the vortex column cores, the outer regions of the vortex columns and regions in-between the columnar structures.

1.4 Governing Equations and Quantities of Interest

In the following the equations describing the fundamental quantities evaluated in this work are summarized and the important terms are discussed. Also the non-dimensional numbers necessary to characterize turbulent flows are listed. Throughout the thesis the Einstein Summation is applied. Turbulent flows are characterized by a high level of random temporal and spatial fluctuations in the flow quantities, which results in vortices with sizes distributed over a wide range of spatial scales. The main physical mechanisms that control fluid turbulence

at the smallest scales are commonly described in terms of strain and vorticity. These quantities, which represent the tendency of fluid parcels to deform and rotate, respectively. The transport equation for vorticity is defined as

$$\frac{D\omega_i}{Dt} = \omega_j s_{ij} + \nu\nabla^2\omega_i + \epsilon_{ijk}\frac{\partial F_k}{\partial x_j}, \tag{1}$$

where ϵ_{ijk} is the Levi-Civita-Symbol. The first term on the right hand side is the vortex stretching vector, $W_i \equiv \omega_j \frac{\partial u_i}{\partial x_j} = \omega_j s_{ij}$, which represents the interaction between vorticity and the rate of strain tensor. Positive W_i symbolizes vortex stretching and negative W_i vortex compression. The second term on the right hand side is the dissipation of vorticity and F_k represents the forcing. The square of vorticity ω^2 is called enstrophy and its transport equation reads

$$\frac{1}{2}\frac{D\omega^2}{Dt} = \omega_i\omega_j s_{ij} + \nu\omega_i\nabla^2\omega_i + \epsilon_{ijk}\omega_i\frac{\partial F_k}{\partial x_j}. \tag{2}$$

Here the first term on the right hand side, $\omega_i\omega_j s_{ij}$, is the enstrophy production term, which is positive in the mean. The average of the second term, $\nu\omega_i\nabla^2\omega_i$, is responsible for enstrophy destruction. The latter can not be called dissipation of enstrophy because enstrophy is not an inviscidly conserved quantity (see, Tsinober (2001)).

Another important quantity for the description of turbulent flows is the rate of strain tensor, $s_{ij} = \frac{1}{2}\left(\frac{\partial u_i}{\partial x_j} + \frac{\partial u_j}{\partial x_i}\right)$. The transport equation for the rate of strain tensor is given by

$$\frac{Ds_{ij}}{Dt} = -s_{ik}s_{kj} - \frac{1}{4}\left(\omega_i\omega_j - \omega^2\delta_{ij}\right) - \frac{\partial^2 p}{\partial x_i\partial x_j} + \nu\nabla^2 s_{ij} + F_{ij}, \tag{3}$$

where δ_{ij} is the Kronecker delta and $F_{ij} = \left(\frac{\partial F_i}{\partial x_j} + \frac{\partial F_j}{\partial x_i}\right)$. Analogously to enstrophy there is also an equation for the total strain

$$\frac{1}{2}\frac{Ds^2}{Dt} = -s_{ik}s_{jk}s_{ki} - \frac{1}{4}\omega_i\omega_j s_{ij} - s_{ij}\frac{\partial^2 p}{\partial x_i\partial x_j} + \nu s_{ij}\nabla^2 s_{ij} + 2s_{ij}F_{ij}. \tag{4}$$

Analogously to $\omega_i\omega_j s_{ij}$ in equation 2 the terms $-s_{ik}s_{jk}s_{ki} - \frac{1}{4}\omega_i\omega_j s_{ij} - s_{ij}\frac{\partial^2 p}{\partial x_i\partial x_j}$ represent the inviscid production of total strain while $\nu s_{ij}\nabla^2 s_{ij}$ is the viscous strain destruction term. The dynamics of 3D turbulence can be described based on the quantities ω_i and s_{ij} as discussed in Tsinober (2001).

In homogeneous, incompressible flows the generation of strain and enstrophy fulfill the relation

$$\langle -s_{ik}s_{jk}s_{ki}\rangle = 4\langle\omega_i\omega_j s_{ij}\rangle \tag{5}$$

and the pressure term vanishes

$$\left\langle s_{ij}\frac{\partial^2 p}{\partial x_i\partial x_j}\right\rangle = 0. \tag{6}$$

Some of the terms discussed above are not only part of the transport equations but also form invariant quantities. Geometrical invariants of the velocity gradient tensor are formed in such a way that they remain unchanged under the full group of rotations and reflections. The first order invariant, $P = \frac{\partial u_i}{\partial x_i}$ vanishes for incompressible flows, the second order invariant describes the relation between enstrophy and total strain, $Q = \frac{1}{4}\left(\omega^2 - 2s^2\right)$. The connection between the production terms of enstrophy and total strain is characterized by the third invariant, $R = -\frac{1}{3}\left(s_{ij}s_{jk}s_{ki} + \frac{3}{4}\omega_i\omega_j s_{ij}\right)$. As mentioned in Davidson (2007) joint probability density functions (PDFs) of the second and third invariant can be consulted to characterize the flow, see section 2.5. The three geometrical invariants are coefficients in the characteristic equation for the eigenvalues of $\frac{\partial u_i}{\partial x_j}$ given by the following equation

$$\alpha^3 + P\alpha^2 + Q\alpha + R = 0. \tag{7}$$

Geometrical quantities like the alignment between certain vectors are a manifestation of the dynamics and structure of turbulence Tsinober (2001). By their very definition, alignments are suitable for studying events of any magnitude, because they do not contain the amplitude of quantities and an additional property is that they are invariant in the sense that they are independent of the system of reference which makes them very appropriate to study physical processes in a general way, Tsinober (2001). The most prominent alignments are the cosine of the angle between the vorticity vector, ω, and the eigenvectors of the rate of strain tensor, λ_i, which is associated with enstrophy production and the cosine of the angle between ω and the vortex stretching vector, W. The vortex stretching vector characterizes the interaction between vorticity and strain, i.e., stretching ($W > 0$), compression ($W < 0$) and tilting of vorticity. Enstrophy production and vortex stretching are connected by the rate of enstrophy production, $\alpha = \Lambda_i cos(\omega, \lambda_i)$, see Equation 8 (Tsinober (2001)).

$$\omega_i\omega_j s_{ij} = \omega^2\Lambda_k cos^2(\omega, \lambda_k) = \alpha\omega^2;\ W^2 = \omega^2{\Lambda_k}^2 cos^2(\omega, \lambda_k), \tag{8}$$

where Λ_k are the Eigenvalues of the rate of strain tensor. From this equation it can be seen that the interaction between vorticity and the rate of strain tensor, which is essential for 3D-turbulence depends not only on the magnitude of vorticity and strain but also on the geometry of the field of velocity derivatives, i.e. the orientation of vorticity and the eigenframe of the rate of strain tensor. For 3D-turbulence a strong alignment between vorticity and the intermediate eigenvector, λ_2, is known, see Siggia (1981), Ashurst et al. (1987), Tsinober (1998). However, the largest contribution to the enstrophy production is associated with the largest eigenvalue, Λ_1. The reason can be found in the intermediate Eigenvalue, Λ_2, which assumes both positive and negative values thus also reducing the enstrophy production, while Λ_1 is positive and has a larger magnitude than Λ_2. Nevertheless, also Λ_2 adds to the production of enstrophy since it is known to be positively skewed in 3D-turbulence, Tsinober (1998). Negative values of enstrophy production, namely vortex compression is associated with an alignment between ω and λ_3 ($\Lambda_3 < 0$). The alignments between ω and λ_1, λ_2 and

λ_3, respectively correspond to regions of the flow, which are qualitatively different and will be discussed in Section 3.2 where PDFs of these quantities are presented. According to Tsinober (2001) the importance of the predominant vortex stretching and positive net enstrophy production can be characterized by the angle between the vorticity and the vortex stretching vectors, $cos(\omega, W)$. Tsinober (2001) introduces the relation

$$cos(\omega, W) = \frac{\Lambda_k cos^2(\omega, \lambda_k)}{({\Lambda_k}^2 cos^2(\omega, \lambda_k))^{1/2}}, \tag{9}$$

and illustrates that the alignment between ω and W and thus positive enstrophy production is realized when ω is aligned with λ_1 ($\Lambda_1 > 0$) or λ_2 ($< \Lambda_2 > > 0$). The relation also shows that an alignment between ω and λ_3 ($\Lambda_3 < 0$) corresponds to negative enstrophy production.

Further invariants, which are employed to characterize the transition from 3D to quasi-2D, which appears in rotating turbulent flows are the cosines $cos(u, \Omega)$, $cos(\omega, \Omega)$ and $cos(a_{cl}, a)$, namely the angles between the velocity vector, u, and the axis of rotation, Ω, the vorticity vector, ω, and the axis of rotation, the Coriolis acceleration, $a_{cl} = -2(\Omega \times u)$ and the material acceleration, a.

Finally the quantities necessary to characterize turbulent flows are introduced. The Kolmogorov length scale, η, is the characteristic length scale of the smallest eddies in the system and is defined as

$$\eta = \left(\frac{\nu^3}{\epsilon}\right)^{\frac{1}{4}}, \tag{10}$$

where ϵ is the mean dissipation rate which is defined as

$$\epsilon = 2\nu \langle s_{ij} s_{ij} \rangle \tag{11}$$

and ν the kinematic viscosity (see Kolmogorov (1941b), Kolmogorov (1941a)). Kolmogorov also defined a time scale τ_η which is characteristic for the smallest time scales that occur in a turbulent flow.

$$\tau_\eta = \left(\frac{\nu}{\epsilon}\right)^{\frac{1}{2}} \tag{12}$$

The Taylor micro scale, λ, relates the velocity fluctuations to velocity derivatives.

$$\lambda = \sqrt{\frac{\overline{{u_i}^2}}{\overline{\frac{\partial u_i}{\partial x_j}^2}}} \tag{13}$$

It is not related to any physical length scale in the flow and it is also not a dissipative scale because the definition is based on u which does not relate to the viscous eddies. Nevertheless the definition has historical reasons and it is convenient to estimate the dissipation using $s_{ij} \sim u/\lambda$. Also, it is common to

define the Reynolds number in isotropic turbulent flows based on the Taylor micro scale.

$$Re_\lambda = \frac{u\lambda}{\nu},\ with\ u = \sqrt{\frac{1}{3}\overline{u_i u_i}} \tag{14}$$

The largest scales of a flow are characterized by the integral length scale,

$$\ell = \int_0^\infty R_{ii}(r,t)dr, \tag{15}$$

where R_{ii} is the autocorrelation function defined as

$$R_{ii}(r,t) = \frac{\langle u_i(x_i,t)u_i(x_i+r,t)\rangle}{\langle u_i^2\rangle}. \tag{16}$$

The relation between the small and the large scales is a function of the Reynolds number in isotropic turbulence,

$$\frac{\eta}{\ell} = Re^{-3/4}. \tag{17}$$

Two more non-dimensional numbers that are important in the context of this work are the Rossby number, Ro, and the Stokes number St. Ro is defined as the ratio of inertial to rotational forces

$$Ro = \frac{U}{2\Omega L}, \tag{18}$$

where U and L are characteristic velocity and length scale and Ω is the rotational velocity. The Stokes number is the ratio of the response time of a particle in the fluid, τ_p, to a characteristic time scale of the flow. Since the particles have to follow even the smallest velocity fluctuations of the flow the characteristic time scale of the flow is chosen to be the Kolmogorov time scale.

$$St = \frac{\tau_p}{\tau_\eta} = \frac{\frac{(\rho_p/\rho_f){d_p}^2}{18\nu}}{\tau_\eta} = \frac{\rho_p {d_p}^2 \epsilon^{1/2}}{18\rho_f \nu^{3/2}}, \tag{19}$$

In Equation 19 ρ_p is the particle density, d_p the particle diameter and ρ_f the fluid density.

The curvature, $curv$, is the reciprocal value of the radius of curvature and will be used to characterize the flow trajectories. It can be calculated as the magnitude of the vector product between the Lagrangian acceleration and the velocity divided by magnitude of the velocity to the power of three.

$$curv = \frac{|a \times u|}{|u|^3} \tag{20}$$

In the following, u denotes the velocity vector with $u_{hor} = \sqrt{{u_x}^2 + {u_z}^2}/\sqrt{2}$ and $u_{ver} = u_y$ being the horizontal and vertical components, respectively.

1.5 Outline of the Thesis

As mentioned above the aim of this thesis is to analyze the effect of confinement and system rotation on shear-free turbulence. The problems are investigated experimentally in an oscillating grid chamber via optical measurement techniques. Section 2 describes the methods, experimental setup and techniques used in this study. In particular, the measurement techniques Pearlescence, Particle Image Velocimetry (2D-PIV) and Particle Tracking Velocimetry (3D-PTV) are introduced. In this thesis, the experimental setup of the 3D-PTV technique was extended in order to allow for simultaneous measurements of two different volume sizes, i.e. with two varying spatial resolutions. Accuracy checks for the spatial resolution in the different Particle Tracking Velocimetry measurements are presented. The Section closes with an overview over the experimental program.

With this the foundation is laid for the presentation of the results in section 3. In the first part the results of the spreading of turbulence are illustrated for three cases, which are free diffusion (case i), spreading under the influence of confinement (case ii) and rotation (case iii). The following part of the results deals with more general effects of system rotation on shear-free turbulence. These effects relate to the spatial transition region from three-dimensional to quasi-2D turbulence and associated columnar structures. First, the dependence of large and small scale quantities on the distance from the energy source is analyzed and compared to the non-rotating case. The emphasis is on magnitudes of quantities, but also on geometrical statistics, such as the alignment between certain vectors and the axis of rotation. Thereafter, results on the spatial transition region between three-dimensional and quasi-2D turbulence are presented and compared to results on its counterpart in the non-rotating case, namely the turbulent/non-turbulent interface. Next, the quasi-2D flow region and associated columnar vortices are analyzed in more detail. Again, this is done on the level of large and small scale quantities. The last section of the results deals with the influence of the magnitude of the rotational velocity on the alignments, which are formed in the flow by the Coriolis force as well as on the small scale quantities.

Finally conclusions are drawn and the main results summarized in Section4.

2 Method

This section describes the methods, experimental setup and techniques used for this study. It starts out with an illustration of the experimental apparatus, namely the oscillating grid and the rotating table, followed by the presentation of the measurement techniques used. All the techniques are based on high speed imaging of neutrally buoyant tracer particles seeded into the flow. We have used Pearlescence, Particle Image Velocimetry (2D-PIV) and Particle Tracking Velocimetry (3D-PTV). In this thesis, the 3D-PTV setup and processing was extended in order to allow for simultaneous measurements with two separate systems with different measurement volume sizes, which from here on is referred to as 'simultaneous two-scale measurements' (STS-3D-PTV). This Section summarizes the necessary information and parameters relevant for this work. For further details and broader background on the main principles and fundamentals of PIV and 3D-PTV, the reader is refered to Raffel et al. (1998), Maas (1996) and Tropea et al. (2007) for further details. After the presentation of the techniques, we show checks and verifications of the 3D-PTV and simultaneous two-scale 3D-PTV measurements. These allow judgment of the achieved spatial and temporal resolution in the conducted measurements and demonstrate the congruence between the different observation volumes in the simultaneous two-scale measurements. Thereafter the procedures for the post processing of the data obtained from the PIV and PTV analyses are explained. The first method is applied to identify and track the turbulent/non-turbulent interface from the measured instantaneous out-of-plane vorticity component. Next, a method to determine the position and size of the columnar structures from velocity fields measured in the experiments with system rotation is introduced. Finally, the experimental program is explained, where the main parameters for the different setups and experiments are also listed in Table 2.

2.1 Experimental Setup

The measurements have been carried out in a 200x200x300 mm^3 water tank in which the flow is mechanically forced from the top by an oscillating grid, see Figure 1. The apparatus is the same as the one described in Holzner et al. (2006) except for the geometry of the grid. Two different grid geometries were used, a regular grid with a bar diameter of d=1 mm and a mesh-size of d_0=4 mm and a fractal grid with the simplest cross-type fractal pattern, a maximum bar width of 4 mm and three fractal iterations (see Hurst and Vassilicos (2007) for details). While the first grid was used to force the flow in the studies concerned with the spreading of turbulence, the fractal grid was used for another set of experiments on turbulence under the influence of system rotation, where the flow was measured via 3D-PTV. The advantage of the fractal grid is that it injects more energy into the flow and forces a wider range of scales (see, Hurst and Vassilicos (2007)). A schematic of both grids is presented in Figure 2. In the experimental setup the grid is connected to a linear motor, which drives the vertical oscillation on a supporting frame connected to the grid by four

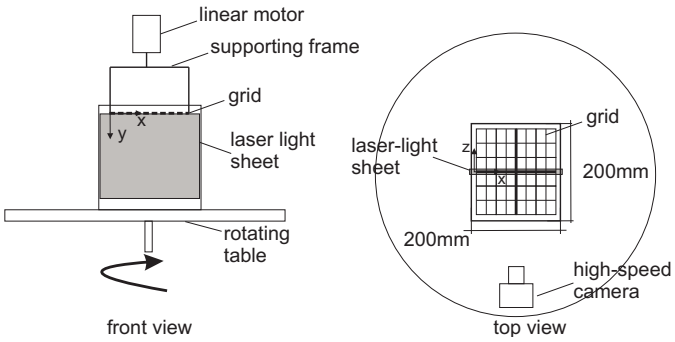

Figure 1: Schematic of the experimental setup with the position of the laser light sheet for the visualization and PIV measurements.

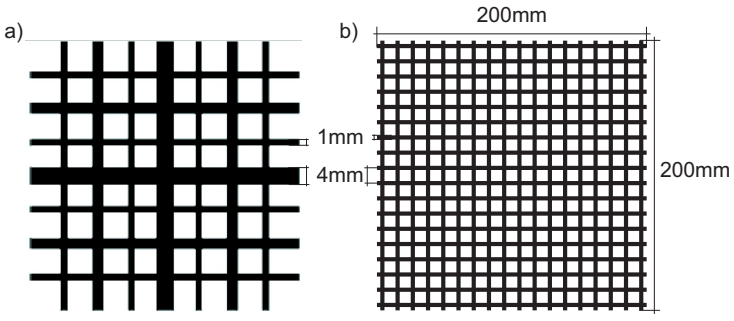

Figure 2: Schematic of the grid geometries

rods each 4 mm in diameter, Figure 1. The motor, operated in a closed loop with feedback from a linear encoder, was set at a frequency of 9 Hz and at an amplitude $\epsilon = \pm 4$ mm for all the experiments. For the fractal grid the measured r.m.s. velocity of the flow was about 10 mm/s and we estimated the Kolmogorov length scale to be η=0.4 mm using Equation 10, where the dissipation was directly measured via 3D-PTV. The Taylor microscale, λ, was about 6 mm and the Kolmogorov time scale, τ_η, was estimated as 0.3 s. The Taylor-microscale Reynolds number is Re_λ=60. The values for the regular grid are slightly lower resulting in Re_λ=50. Baffles were located at the bottom of the tank to minimize the large scale circulations inside the tank. For the studies in which the spreading of the turbulence is influenced by a confined integral length scale we placed a thin-walled transparent tube in the center of the tank, so that the length scales of the turbulent flow inside the tube were confined by its diameter. Also, the whole setup was placed on a rotating table with a diameter of 1 m, allowing for rotation rates up to 3.14 rad/s (see Figure 1). The power supply and the control of the grid are provided through a slip ring at the base of the rotating table.

2.2 Particle Image Velocimetry

In planar PIV the flow is seeded with tracer particles. The particles are illuminated, typically using a laser light sheet, and images are taken using high-speed cameras. From these images 2D Eulerian velocity information is extracted via correlation techniques applied to two subsequent exposures (see Raffel et al. (1998) and references therein).

In this work, time resolved PIV experiments were conducted using a high-speed camera (Photron Ultima APX, 1,024 x 1,024 pixels) at a frame rate of 50 Hz. The maximum recording time at this frame rate was 80 s. Both, camera and memory are located on the rotating table. The beam of a continuous 20 Watt Ar-Ion laser is circularly polarized, aligned with the axis of rotation and inserted into the rotating system. There it is expanded through a cylindrical lens and forms a planar laser sheet of about 1 mm in thickness, which passes vertically through the mid-plane of the tank, as can be seen schematically in Figure 1 and in the photograph shown in Figure 3. The camera was triggered by the onset of grid motion and recorded the light scattered by neutrally buoyant Polystyrene tracer particles with a diameter of 40 μm and a density of 1.05 kg/m^3. Sodium chloride was added to the water so that the density ratio between the working fluid and the tracer particles was approximately one. The particle size and seeding density lie within the range of diameters typically used for such configurations (see, e.g., Melling (1997)) and the Stokes number was calculated to be of the order of 10^{-3}, which ensures that the particles follow the flow reliably. The PIV images were processed by using the commercial software Flowmanager 4.71 by Dantec Incorporated. An interrogation window size of 32 x 32 pixels at 50% overlap was applied, yielding approximately 4000 two-component velocity vectors per image pair. During the post-processing the standard global outlier and local median filters were applied and about 2.8% of erroneous vectors were

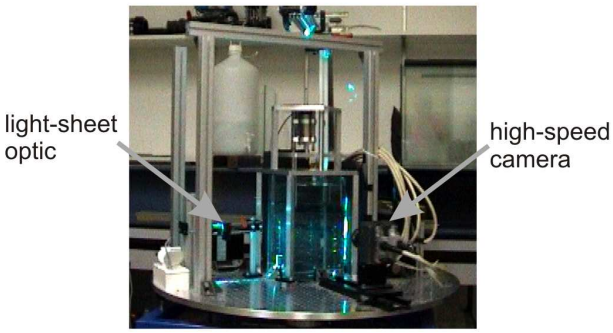

Figure 3: Photograph of the PIV-setup on the rotating table

found and replaced using linear interpolation. The accuracy of the measured displacements is estimated at 0.1-0.3 pixel, e.g., Tropea et al. (2007), Nobach and Bodenschatz (2009), which implies a measurement error on the order of 1 mm/s for the velocity. The typical displacement of the particle images in the proximity of the oscillating grid is about 6 pixels per frame. Since the r.m.s. velocity attenuates with distance from the grid, the typical displacement reduces to about 3 pixels per frame in the lower region of the field of view.

2.3 3D-Particle Tracking Velocimetry

Particle tracking velocimetry (3D-PTV) is an intrinsically Lagrangian measurement technique that has been established in an automated form as a valuable tool for 3D flow measurements over the last two decades or so, see, e.g. Maas et al. (1993) and references therein. The method relies on the stereoscopic recognition and subsequent tracking in time of tracer particles in an illuminated volume by using a multi-camera setup. A bottleneck of this technique lies in the maximum seeding density of tracer particles. In order to keep a low probability of false particle detection and of overlapping particle images the number of particles detected per frame is restricted to approximately 0.05 particles per pixel or a total number on the order of 10^3 particles per image respectively. Using a scanning light sheet the maximum seeding density could be increased to an order of 10^4, see Hoyer et al. (2005). Nevertheless, the number of particles, which can be recorded and identified on a camera chip is limited and therefore a trade off between the use of a large observation volume with a low seeding density and a small observation volume with a high seeding density is necessary. The advantage of a large observation volume is that it allows to capture large scale flow features at the expense of spatial resolution at the small scale level while, alternatively, it is possible to focus on a small observation volume and resolve the viscous scales, but then compromising the larger scales. In a recent further development, Lüthi et al. (2005) succeeded in obtaining a resolution that is high enough to allow the full tensor of velocity derivatives to be measured for the first time along particle trajectories. Due to the limitation on the seeding density per image, the Reynolds number was kept low, $Re_\lambda \approx 50$

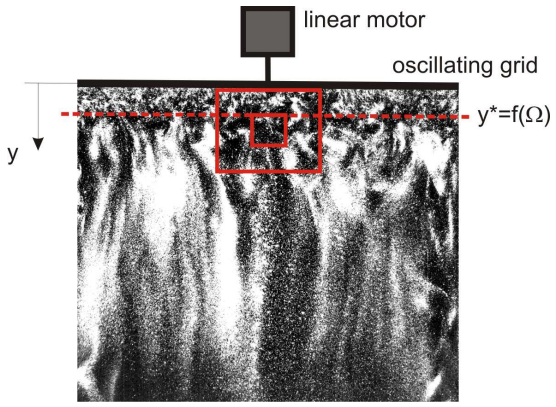

Figure 4: Visualization of the turbulent flow under the influence of rotation using Pearlescence. The locations of the large and small PTV observation volume are marked by the red squares.

and the observation volume small, $\approx 1cm^3$. A second limitation for the seeding density is the ratio between the mean displacement of a single particle between consecutive images and the mean inter particle distance within one image. This parameter should be small for good trackability, i.e., for an explicit allocation of a particle in two consecutive images.

In this study we want to measure both large scale features of the flow and obtain at the same time small scale quantities with sufficient spatial resolution. Therefore, in view of preparation for simultaneous measurements, 3D-PTV measurements were performed separately in a large and a small observation volume, to test the feasibility of capturing the large-scale structures of the flow with the former and relevant Lagrangian small-scale information with the latter measurements. The light beam of a continuous 20 Watt Argon-Ion laser is guided onto the rotating table as described in section 2.2 and expanded through spherical lenses to illuminate a large observation volume of size $50\times50\times40$ mm^3 or a small observation volume of size $15\times15\times15$ mm^3, respectively. The locations of the two observation volumes are presented in Figure 4 with respect to the oscillating grid and the flow topology. The snapshot is taken from preliminary flow visualization experiments by using Pearlescence (small plate like particles that align with shear and visualize the flow structure, see Savas (1985)).

Figure 5 displays the PTV-system with the 105 mm macro lens used for the small observation volume. Due to the limited space available on the rotating table the 3D-PTV system consists of a Photron APX high speed camera with 1024x1024 $pixels^2$ in combination with an image splitter that mimics a four-camera setup, see Figure 5 and Hoyer et al. (2005) for details. The camera can be triggered isochronously with the onset of the grid movement or at an arbitrary point in time.

With this setup interparticle distances of 8.5 η in the large and 2.5 η in the small observation volume could be achieved. The parameter η was estimated

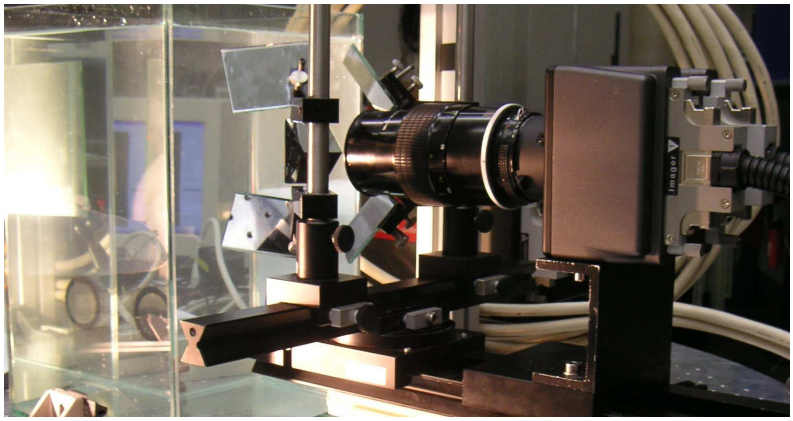

Figure 5: Photograph of the PTV-system for the small observation volume consisting of the high-speed camera, the 105 mm macro objective and the image splitter.

from an experiment without rotation, by direct measurement of the dissipation, ϵ, in the center of the measurement volumes. The light was scattered by Polystyrene particles with a diameter of 80 μm for the large and 40 μm for the small observation volume, respectively. Sample images can be seen in Figure 6 for the large (a) and small (b) observation volume. The seeding density in the large observation volume is relatively low, i.e. approximately 15 particles per $10mm^3$. The image from the measurement in the small observation volume shows a higher density of particles, i.e. approximately 200 particles per $10mm^3$. The dark area in the lower part of the image results from limitations due to the design of the image splitter, which in its present form is more suitable for larger fields of view. More precisely, the projection of the small volume only covers a small region in the center of the mirror pyramid of the image splitter. The high magnification of this image onto the camera chip also magnifies the small gap between the mirrors on the facing surfaces of the pyramid. For the measurements described in section 2.4 a new image splitter was manufactured with higher accuracy so that the dark areas are considerably smaller, see Figure 7. It can also be noticed that, although the particles in the small observation volume are smaller than the particles in the large observation volume, they appear larger in the images because of the higher optical magnification. We have added sodium chloride to the water to achieve neutral buoyancy of the seeding particles. The Stokes number based on τ_η was calculated to be of the order of 10^{-3} for both types of seeding particles which demonstrates their ability to follow the turbulent small scale motions of the flow. The measurement accuracies of the particle positions were found to be approximately 0.035 mm in x- and y- and 0.09 mm z-direction for the large and 0.02 mm and 0.045 mm for the small observation volume, respectively.

The velocity and velocity derivatives along particle trajectories were measured for the two types of experiments in the same way as described in Lüthi

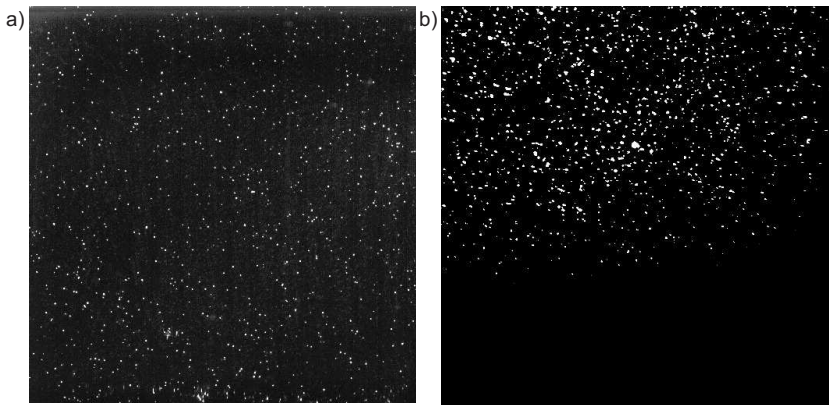

Figure 6: Typical 3D-PTV images from the large (a) and the small observation volume (b).

et al. (2005). The post processing was extended to allow for interpolation of the measurements on an Eulerian grid, similar to Holzner et al. (2007). The Eulerian data was filtered in time by using binomial coefficients to realize a compact but Gaussian weighting function. The applied filter width was about $0.1\tau_\eta$.

2.4 Simultaneous Two-Scale 3D-Particle Tracking Velocimetry

After the proof of concept described in the previous subsection, 3D-PTV measurements were performed simultaneously in a small and a large observation volume. In addition to the previously described PTV system with the Photron APX camera a second PTV system was set up on the opposite side of the tank. This second system also uses an image splitter but in connection with a Photron Fastcam high speed camera (1024x1024 $pixels^2$) and can be triggered by the same signal as the APX camera. A CAD drawing shows how the two systems are arranged on the rotating table, see Figure 8. A key element of the simultaneous two-scale measurements is the seeding which has to be different for the two observation volumes. Namely, the seeding particles have to be larger and the seeding density lower in the large observation volume. Thus it is necessary to apply two different kinds of seeding particles which not only have the appropriate size for each magnification but also can be separated by means of filters. Polystyrene particles with a diameter of 60 μm were employed for the large observation volume and Polystyrene Rhodamine B particles with a diameter of 80 μm for the small observation volume. The choice of the larger particle diameter in the seeding for the small observation volume is due to the loss in light intensity due to the absorption / emission and filter processes connected to the use of Rhodamine particles. Both cameras were equipped with color filters (green/550nm for the Polystyrene and red/590nm for the Polystyrene Rhodamine B particles)

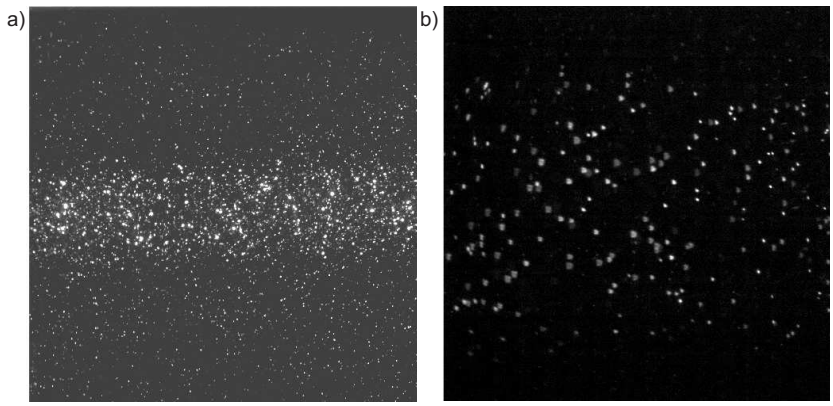

Figure 7: Typical simultaneous 3D-PTV images form the large (a) and the small observation volume (b).

to separate the two types of seeding particles. Sample images can be seen in Figure 7 for the large (a) and small (b) observation volume showing that the filters separate the different seeding particles reliably. Additionally, the illumination of the observation volumes has to be adapted since the light intensity needed for the illumination of the small observation volume is considerably higher than for the large observation volume and the available laser light was not sufficient to illuminate the large volume in the intensity needed for the small volume. Furthermore it is not an option to open the aperture of the cameras from the small PTV-system any further for loss of depth of focus. Since only one laser was available, the laser beam was expanded through spherical lenses to illuminate a small observation volume of size $15\times15\times15$ mm^3. After passing through the tank the beam is reflected, expanded further to the size of the large observation volume ($55\times55\times50$ mm^3) and sent back through the tank. The result can be observed in Figure 7 (a) where a typical picture of the seeding in the large observation volume is displayed. The seeding density is slightly higher than in the experiments where both scales are measured separately. The image field of the small observation volume is used more efficiently in comparison to the previous measurements. Nevertheless, the spatial resolution that could be achieved and the light intensity of the tracer particles are lower. The reason for the lower light intensity are the Rhodamine seeding particles in the small observation volume which emit less light than the polystyrene particles. The results are interparticle distances of 9.5 η and 2.5 η in the large and the small observation volume, respectively. Also, for these experiments the Stokes numbers of the two kinds of seeding particles were calculated to be of the order of 10^{-3}, assuring that the particles follow the flow reliably.

Guala et al. (2008) used a similar configuration to perform simultaneous measurements of the fluid and the solid phase in a two-phase PTV experiment. They constructed a planar calibration target for a multi plane cross calibration of

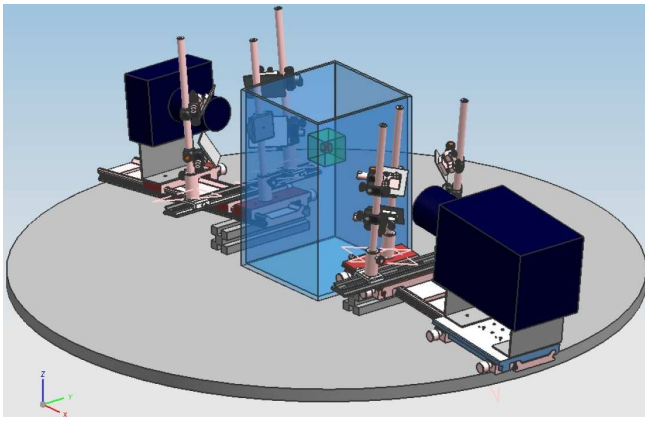

Figure 8: CAD sketch of the two PTV-systems including the large and the small observation volume

two PTV observation volumes. The target consisting of two identical aluminum plates with conical holes and aluminum foil with a thickness of less than $10\mu m$ between them. In this work the same device is used to focus both camera systems on the same x-y-plane in the center of the observation volume. In contrast to Guala et al. (2008), each PTV-system was then calibrated with a separate three dimensional calibration target, namely the ones used by Lüthi (2002). Both targets were positioned with a 3D-traversing system inside the tank. The offset between them is thus known and the data from the small observation volume can be easily transformed to the coordinate system of the large observation volume. Only the quantities in x- and z-direction have to be inverted and an offset in space has to be added. The checks in the following section show that this procedure yields similar accuracies for the particle positions, velocities and velocity derivatives as for the case when both measurements are carried out separately.

2.5 Checks and Verification of Procedures

To ensure that the required spatial resolutions for the 3D-PTV experiments at two different observation volume sizes are met and that the two observation volumes are well synchronized in the setup where both ranges of scales are recorded simultaneously several checks are performed. These checks are based on data from experiments without system rotation.

Velocity derivatives were derived from the measurements using the method introduced by Lüthi et al. (2005). The method also allows to interpolate the Lagrangian data from the 3D-PTV measurements onto an Eulerian grid so that all measured quantities are available in both reference systems. Spatially underresolved velocity derivatives were obtained from the experiment in the large observation volume, while spatially resolved velocity derivatives are available from the data measured in the small observation volume. First, following the approach of Lüthi et al. (2005), statistical checks based on precise kinematic re-

lations are presented to validate our methodology and to assess the accuracy of the measurements of velocity gradients for both 3D-PTV systems individually. These tests can be applied to both data sets, namely in the Lagrangian and Eulerian frame. In the following results are presented for the Lagrangian data set. However, the results for the Eulerian data set are very similar and can be found in Appendix B. The first check involves the Lagrangian acceleration obtained directly through differentiation along particle paths and independently obtained spatial derivatives of the velocity. The Lagrangian acceleration $a_i = Du_i/Dt$, is related to the local acceleration, $a_{l,i} = \partial u_i/\partial t$, and convective acceleration, $a_{c,i} = u_j \partial u_i/\partial x_j$, through the following equation:

$$\frac{Du_i}{Dt} = \frac{\partial u_i}{\partial t} + u_j \frac{\partial u_i}{\partial x_j} \tag{21}$$

Joint PDFs of a_i versus $a_{l,i} + a_{c,i}$ are shown in Figure 9 for the large (top)

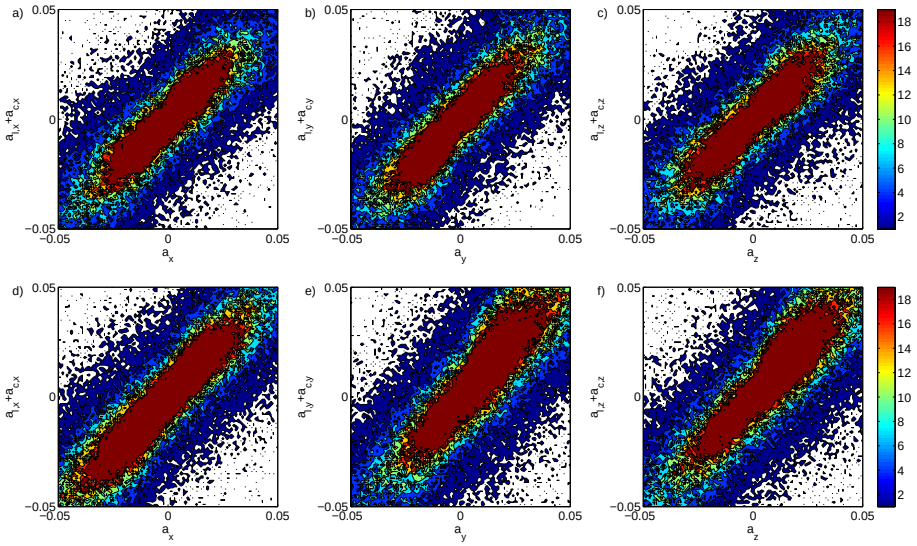

Figure 9: Joint PDFs of $a_{l,i}$+$a_{c,i}$ versus a_i for i=x, y, z for large (top) and the small observation volume (bottom) in the Lagrangian frame.

and the small observation volume (bottom). The data was taken from an experiment where both observation volumes were recorded separately. It can be seen clearly that most points fall onto the diagonal and the aspect ratios of the iso-probability contours are very close to the ones shown in Lüthi et al. (2005). Interestingly, the result looks very similar for both types of experiments indicating that under-resolution might affect Lagrangian acceleration and spatial derivatives of the velocity in a similar fashion so that the balance of Equation 21 is maintained. This indicates that the accuracy of the measured velocity derivatives is comparable for both volumes. The same check was performed for the

experiment where both observation volumes were recorded simultaneously and for the data in the Lagrangian and Eulerian frame. The results are similar and can be found in Appendix B.

Another resolution check involves the second and third invariants of the velocity gradient tensor. While the second invariant relates to the relative strength of enstrophy and strain, $Q = 1/4(\omega^2 - 2s^2)$, the third compares their production terms, $R = -1/3(s_{ij}s_{jk}s_{ki} + 3/4\omega_i\omega_j s_{ij})$. In homogeneous, statistically stationary turbulence the iso-probability contours in the R-Q Joint PDF are known to have a 'tear drop' shape with a distinct region in the second quadrant representing the swirling motion of turbulence ($Q > 0$, $R < 0$) and the 'Vieillefosse Tail', (Vieillefosse (1982)) in the fourth quadrant representing the strong dissipative events that occur in turbulence ($Q < 0$, $R > 0$). A good example of this shape can be seen in Figure 10 (c), where the Lagrangian data recorded in the small observation volume is presented. The Joint PDFs in Figure 10 originate from measurements in which both observation volumes were recorded separately and are displayed for the large (top) and the small observation volume (bottom) as well as for the Lagrangian (left) and Eulerian (right) data set. While the iso-contours from the large observation volume are symmetric and

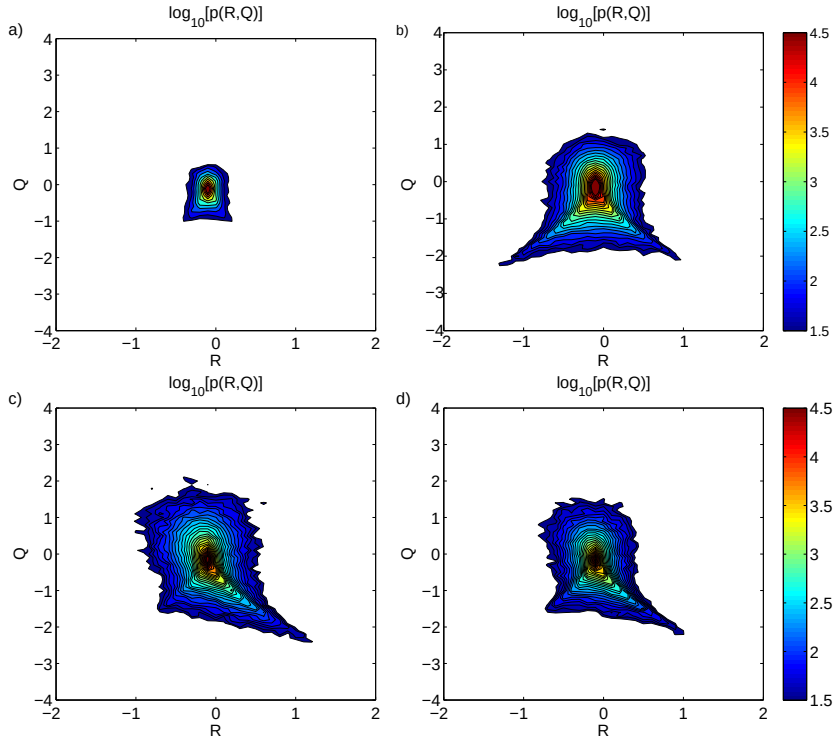

Figure 10: Joint PDF of R versus Q for the large (top) and the small observation volume (bottom) obtained from the Lagrangian (left) and Eulerian (right) data set

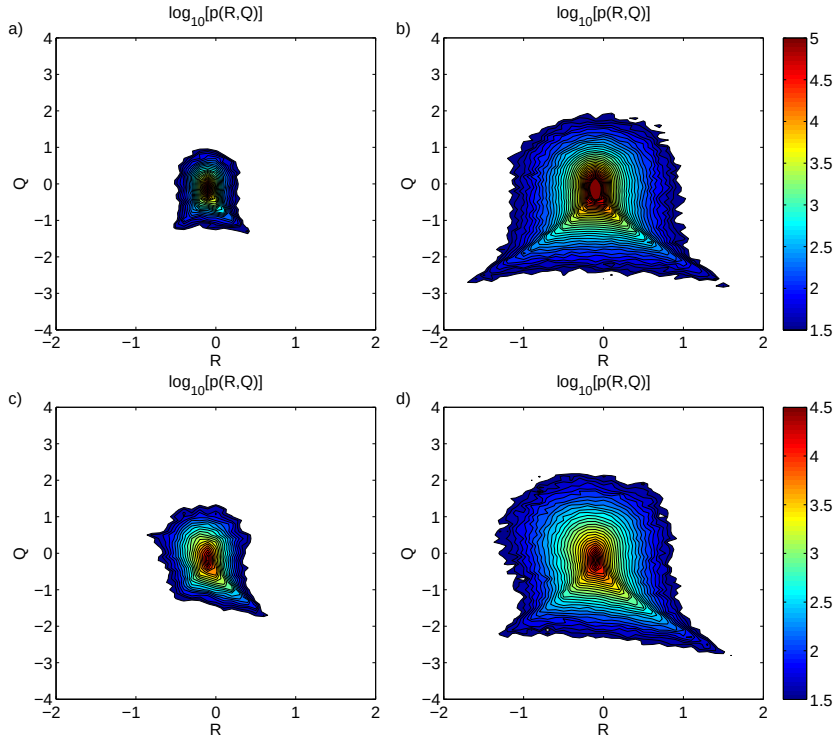

Figure 11: Joint PDF of R versus Q for the large (top) and the small observation volume (bottom) obtained from the Lagrangian (left) and Eulerian (right) data set from a simultaneous two-scale measurement

follow a Gaussian behavior (Figure 10 (a), (b), the results obtained from the higher resolved data set yield the tear-drop shape (Figure 10 c, d). We note that for the spatially under-resolved data the variances of R and Q of the Eulerian data set are higher compared to the Lagrangian data set (Figure 10 (a), (b). Also, the Eulerian data set exhibits more data in the third quadrant, which is attributed to Gaussian noise. Nevertheless the Vieillefosse Tail is also captured in the Eulerian data assuring a satisfactory quality of the measured velocity derivatives.

The corresponding R-Q Joint PDFs for the measurements in which both observation volumes were recorded simultaneously can be found in Figure 11. As before with the acceleration check there is a good agreement between the simultaneous and non-simultaneous data measured with the coarse spatial resolution. However, the lower spatial resolution, which could be achieved in the small observation volume becomes apparent again. While the 'tear-drop' shape is still pronounced in the Lagrangian data with the high resolution, Figure 11 c, it is just distinguishable in the Eulerian data, Figure 11 d. The variances of R and Q of the Eulerian data set are higher compared to the Lagrangian data set for both measurement types.

A drawback of the illumination method used for the simultaneous two-scale measurements becomes apparent when the recorded trajectories are visualized in the y-z-plane (i.e., perpendicular to the laser beam). Trajectories recorded in the large observation volume are shown in Figure 12 (a) from single scale and Figure 12 (b) from simultaneous two-scale measurements. The color coding corresponds to the mean acceleration along the trajectory where red stands for $< |a| > > 0.02m/s^2$ and blue for $< |a| > < 0.02m/s^2$. The trajectories from

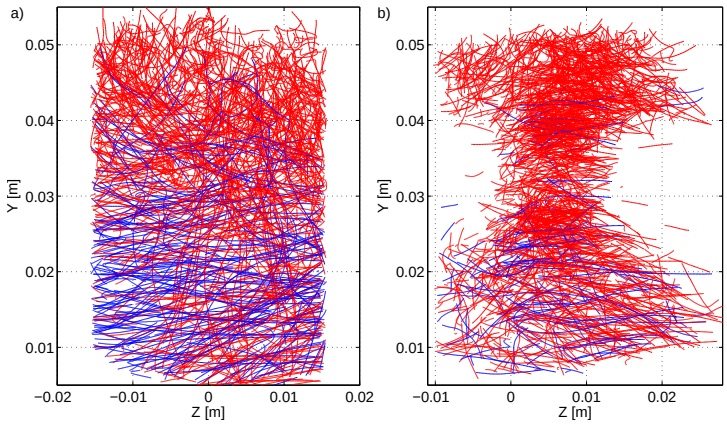

Figure 12: Trajectories visualize in the y-z-plane in the large observation volume from separate (a) and simultaneous two-scale measurements (b)

the simultaneous two-scale measurements exhibit a 'waist' due to the higher light intensity in the center of the observation volume (compare Figure 7 a). The higher light intensities at the center lead to generally bigger particle images that partly hide or overlap with more weakly illuminated particles and therefore prevent smaller particles to be reliably detected in their surroundings.

For the simultaneous two-scale measurements it is not only important to check the performances of the measurements for both observation volumes separately but also to examine the deviation between the two. This was done following the approach of Guala et al. (2008). Namely an experiment in which the color filters were removed from the cameras so that both PTV-systems see the same seeding particles was performed in order to perform a pointwise comparison of the results obtained from both PTV measurement systems. From this experiment the pointwise differences in the particle positions as well as in the measured velocities and accelerations were calculated. Figure 13 illustrates an example of a particle trajectory, which was tracked simultaneously with both PTV-systems. PDFs of the differences in the particle positions, velocities and accelerations, which were obtained simultaneously with both systems are presented in Figure 14. The qualitative comparison of the trajectory shows a good agreement between the particle positions measured in the large (red) and the small (blue) observation volume. The deviation between the curves stems from the additional particle positions outside of the small observation volume that

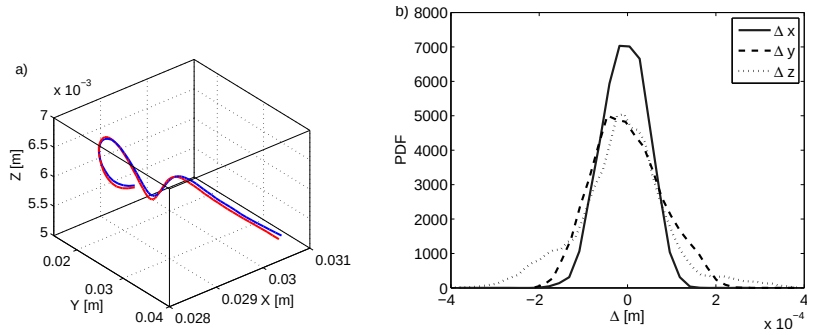

Figure 13: Particle trajectory as recorded simultaneously in the large (red) and the small (blue) observation volume (a) and PDFs of the deviation in the detected particle positions between the two volumes (b)

are known and used for the reconstruction of the trajectory in the large observation volume. The mean spatial difference between the particle locations

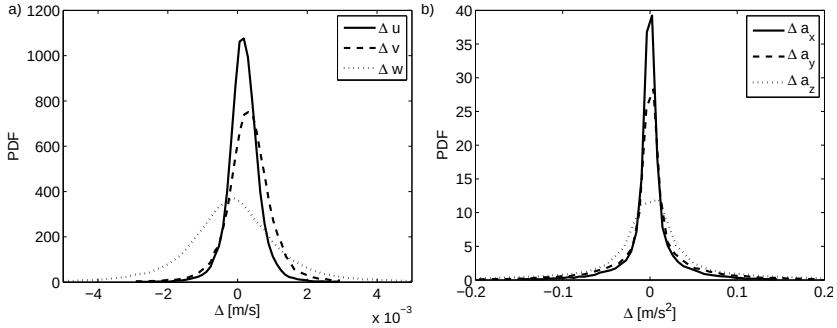

Figure 14: PDFs of the difference in velocity (a) and acceleration (b) measurements between the large and the small observation volume

obtained with the two systems is below 11 μm, which is considerably smaller than the diameter of the seeding particles and the accuracy in the position measurements (see, section 2.3). The differences in the measured velocities and accelerations are of the order of $10^{-3} m/s$ and $10^{-1} m/s^2$ respectively. It thus can be concluded that the use of the two separate systems does not add a bias to the measurements.

2.6 Detection of the Turbulent/Non-Turbulent Interface

We have conducted PIV experiments, where the spreading of turbulence into the irrotational ambient flow region initially at rest is measured. The interface between the turbulent and irrotational flow regions, the so-called turbulent/non-turbulent interface, was detected to determine the speed of growth of the tur-

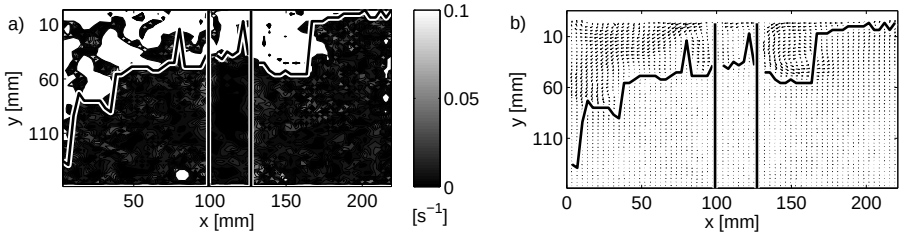

Figure 15: Vorticity magnitude map (a) and velocity vector field and detected TNTI (b) at t=10s

bulent flow region. We detected the turbulent/non-turbulent interface from the 2D-PIV data by using the method based on the out-of-plane vorticity component described in Holzner et al. (2006) with the extension that outliers in the detected turbulent/non-turbulent interface are filtered out. For each time instant t and for each horizontal position, x, the position of the turbulent/non-turbulent interface is the lowest point, $y^*(x,t)$, in which the magnitude of the vorticity signal exceeds a fixed (for all times and x locations) threshold. As in all level-based methods, the threshold has to be set appropriately, but there is no unique, best choice. We adopted the approach of Holzner et al. (2006) (similar methods were used in Westerweel et al. (2002), Bisset et al. (2002)) and determined the value of the threshold by multiplying the rms value of ω_z in the ambient flow (noise level) by a factor of four. The mean position of the turbulent/non-turbulent interface for a given time instance is the average over x of the detected points, i.e. $H(t) =< y^*(x,t) >_x$. Figure 15 shows an example of an instantaneous PIV snapshot. The contours in Figure 15 (a) show the magnitude of ω_z, the vectors in Figure 15 (b) show the direction and the magnitude of the velocity field and the superimposed black line marks the detected turbulent/non-turbulent interface. In general, the turbulent/non-turbulent interface is three dimensional and detection based on only one component of vorticity will inevitably lead to holes in the detected contour where the out-of-plane vorticity is zero, but the other two components are not. Nonetheless, Holzner et al. (2006) showed through comparison of different methods that the mean propagation of the turbulent/non-turbulent interface can be measured with the use of ω_z alone. For example, between the different methods the measured scaling exponents varied within about only 5%. The problem of the appearance of holes could be avoided by using a three dimensional, three component measurement techniques like 3D-PTV or Tomo-PIV but at the cost of a smaller feasible measurement volume. Nevertheless the threshold based turbulent/non-turbulent interface detection method was also implemented for the 3D-PTV data and good agreement with the 2D-PIV data was found (see Figure 16). For all the reasons mentioned above the 2D-PIV technique is adequate for the scope of this work.

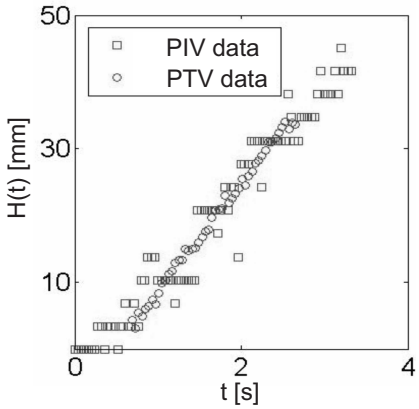

Figure 16: Propagation of the TNTI measured with PIV (□) and PTV (○)

2.7 Detection of the Columnar Vortices

As mentioned above, one of the striking characteristics of turbulence in a rotating system is the occurrence of columnar vortices approximately aligned with the axis of rotation. This section describes how the method introduced by Michard et al. (1997) to detect vortices in 2-D velocity fields is further developed to detect the three-dimensional vortex columns.

The influence of system rotation on the turbulent flow is quantified by the Rossby number, Ro, Equation 18. Ro is the ratio between inertial and rotational forces, i.e., large Ro corresponds to a dominance of inertial forces and hence a negligible influence of rotation and small Ro to a strong influence of the rotational forces. In the proximity of the grid inertial forces dominate, which is reflected in a large Ro and an insignificant influence of the rotational forces. With increasing distance from the grid the inertial forces decrease proportionally to $u\partial u/\partial x$ while the Coriolis force, which depends on the flow velocities becomes smaller with $u \propto y^{-1}$. This causes a dominance of the rotational forces and thus a small Ro. The consequence is a quasi-2D flow, which evolves below a distance $y*$ from the grid where the rotational forces outweigh the inertial ones. As observed in flow visualization experiments presented below (see also, e.g. Hopfinger et al. (1982), Godeferd and Lollini (1998)), this flow region is strongly dominated by columnar vortex structures which we identify based on the method introduced by Michard et al. (1997). The method calculates the mean angular momentum, Γ_1, of the horizontal velocity components u and w at the measured particle locations M around the arbitrary point P (compare Equation 22 and Figure 17).

$$\Gamma_1 = \frac{1}{N} \sum_s \frac{\left(\vec{PM} \times \vec{u}_M\right) \vec{e}_z}{\|\vec{PM}\|.\|\vec{u_M}\|}, \tag{22}$$

where s is the measurement domain and $\vec{e_z}$ the unit vector perpendicular to the

2D-velocity field. According to Michard et al. (1997) the point P is located in the center of a vortex column if $0.9<|\Gamma_1|<1$.

We applied this method to the Lagrangian data recorded through 3D-PTV, while Michard used it for 2D-PIV Eulerian data. The motivation to use the Lagrangian data set was that it allows for direct comparison to other methods based on geometrical properties of particle trajectories. In fact, we were interested to compare the detection based on angular momentum to a method based on the curvature of particle trajectories and to another method based on the angle between the vorticity vector and the axis of rotation. For our data a comparison between the three detection criteria yields a lower threshold of $0.8 < |\Gamma_1| < 1$ for the detection of the vortex column core. The reason might be that the vortex columns are less pronounced in our experiments. When this method is applied to a regular grid of points P, clusters of points with $0.8<|\Gamma_1|<1$ form. We divide the large observation volume into five slices along the y-direction and calculate the clusters for each slice. The line connecting the neighboring centers of gravity of each cluster at different y-planes is defined as the axis of the columnar eddy, an example is shown in Figure 17 (b). In the figure, the black line shows the reconstructed axis for a given time instance, together with measured particle trajectories, which have been tracked for longer than 0.15 s.

The method was tested against ω_y threshold and curvature based methods and good agreement was found between all of them. The different flow states, namely 3D-turbulence and quasi-2D flow, and the columnar structures are well distinguishable in the preliminary visualization experiments using Pearlescence (see section 2.8, Figure 24). From these visualizations, one can estimate number and size of columnar vortices and a comparison with the size of the 3D-PTV observation volume shows that typically one or two columnar eddies can be detected, depending on the rotational velocity.

These visual results also agree well with the Γ_1, ω_z-threshold and curvature method. To find the radius of the vortex columns Michard et al. (1997) calculate the second Galilean invariante, Γ_2, which is utilized to define the boundaries of large scale structures.

$$\Gamma_2 = \frac{1}{N} \sum_s \frac{\left(\vec{PM} \times (\vec{u}_m - \langle \vec{u} \rangle) \right) \vec{e}_z}{\|\vec{PM}\| . \|\vec{u_m} - \langle \vec{u} \rangle \|}, \tag{23}$$

with

$$\langle \vec{u} \rangle = \frac{1}{s} \sum_s \vec{u}_m ds \tag{24}$$

being the mean velocity weighted with the observation area of the measurement, ds. The inner part of the vortex core is defined as the part of the flow where $|\Gamma_2| > 0.6 - 0.7$, Michard et al. (1997). In Figure 18 (a) Γ_2 contours are shown for a rotational velocity of 3.14 rad/s superimposed with the instantaneous Lagrangian velocity vector field, which is obtained in the large observation volume. From the instantaneous Lagrangian velocity field the closest neighbour in the

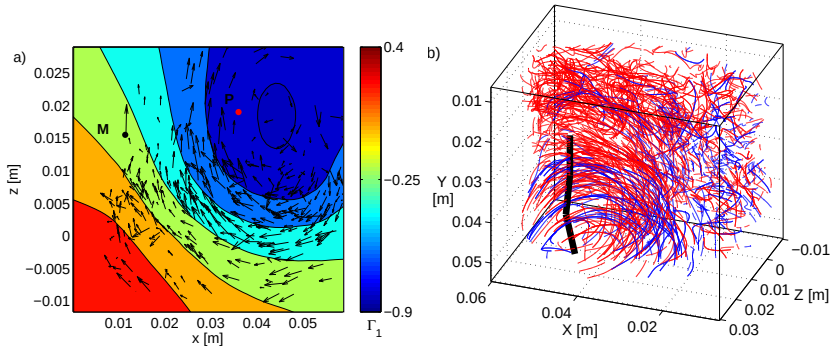

Figure 17: Contourmap of Γ_1 in the large observation volume with superimposed Lagrangian velocity vector field (a) and corresponding trajectories with the detected column center line (b) from an experiment with a rotational velocity of 3.14 rad/s.

mean Eulerian velocity field was subtracted. It can be seen that the velocity vectors are preferentially oriented tangentially to the contour lines. For further comparison Figure 18 (b) illustrates the change in the conditionally averaged flow quantities with distance from the vortex column core, R, for the same rotational velocity. Displayed are the cosines of the angle between the velocity vector and the axis of rotation (which is perpendicular to the x-z plane), between the vorticity vector and the axis of rotation and between the Lagrangian and Coriolis accelerations. It becomes apparent that the alignments all change at roughly the same radial distance from the center of the vortex column. Also note that this radius agrees with the visual impression gained from the velocity vector field on the left side of Figure 18. A detailed analysis of these quantities and what they convey about the flow and the alignments formed by the influence of the rotation will be discussed in section 3.2. However, the comparison between the radial distance, which has been identified as the outer limit of the vortex column and the Γ_2-contours suggest that for the data in this study a threshold of $|\Gamma_2| > 0.4$ seems to be more appropriate.

2.8 Experimental Program

Three different experimental configurations have been employed: (i) experiments in which the grid forcing was started at time t_0 and the turbulent flow could advance freely into the adjacent calm fluid, (ii) experiments in which the turbulent flow was spatially confined by square tubes of different sizes and (iii) experiments in which the spreading of the flow was influenced by rotation. In the experiments of configuration (ii) the domain was confined to 10 mm, 20 mm, 30 mm, 40 mm and 60 mm and for configuration (iii) angular velocities of 3.14 rad/s, 1.57 rad/s, 1.05 rad/s, 0.79 rad/s, 0.39 rad/s and 0.29 rad/s were applied. The fractal grid geometry (see, section 2.1 and Figure 2) was only used for a part of the experiments under the influence of rotation. For all three configura-

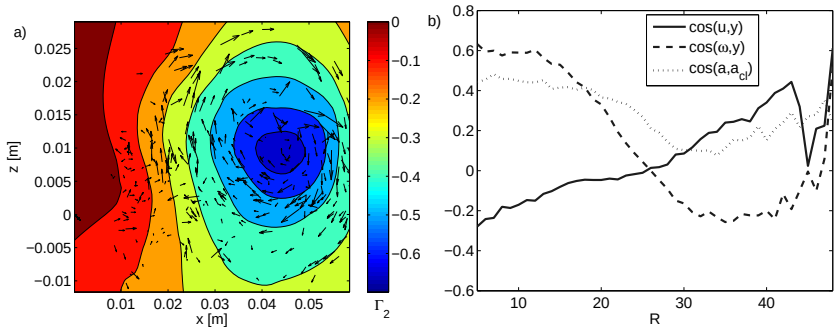

Figure 18: Contourmap of Γ_2 with superimposed Lagrangian velocity vector map in the large observation volume (a) and $< cos(u, y) >$ (solid), $< cos(\omega, y) >$ (dashed) and $< cos(a, a_{cl}) >$ (dotted) conditionally averaged over radial distance from the vortex column core (b) from an experiment with a rotational velocity of 3.14 rad/s.

tions one shot experiments were used to investigate the spreading of turbulence, i.e., the fluid inside the tank was at rest and the recording was started with the onset of the grid movement. For the configurations (i) and (iii) we also conducted experiments where the flow reached a statistically steady state. For the free diffusion experiments this means that the recording was started only 10 minutes after initiation of the forcing. For the rotation experiments the protocol was that the forcing was started 30 minutes after initiation of the rotation and only another 10 minutes later the recording was started. In a first phase all the three experimental configurations have been investigated using visualization experiments based on Pearlescence and velocity measurements via Particle Image Velocimetry. Thereafter, configurations (i) and (iii) were analyzed more thoroughly with three dimensional Particle Tracking Velocimetry. Pearlescence is based on small flakes seeded into the flow and illuminated by a laser sheet, which align with shear and therefore make for a qualitative visualization of the vortical flow structures. From the insights of these visualization measurements the important experimental parameters for the confinement, rotation rates as well as the spin up time needed for solid body rotation were estimated. Next, PIV measurements were carried out with a field of view, which extends over the whole width of the water tank. Finally, 3D-PTV was applied for more detailed analyses of the flow in the experimental configurations (i) and (iii). This was done with two different observation volume sizes, namely a large observation volume of $50 \times 50 \times 40$ mm^3 large enough to capture the large scale features, e.g., columnar eddies for experiment (iii) and a small observation volume of $15 \times 15 \times 15$ mm^3 to measure spatially resolved velocity derivatives. As a first step the PTV measurements were done separately in the two observation volumes. Then two PTV-systems were applied to record both observation volumes simultaneously at the same time. The experiments conducted with the confinement and rotational parameters as well as the measurement techniques, which

Type of experiment	Tube diameter/ angular velocity	Measurement technique	No. of runs No. of runs
case (i)	200 mm (tank width)	PIV	10 one shot
		3D-PTV	1 stationary
		STS 3D-PTV	1 one shot
		STS 3D-PTV	1 stationary
case (ii)	20 mm	PIV	10 one shot
	30 mm	PIV	10 one shot
	40 mm	PIV	10 one shot
case (iii)	3.14 rad/s	STS 3D-PTV	2 stationary
	1.57 rad/s	STS 3D-PTV	4 stationary
	1.04 rad/s	3D-PTV	1 stationary
	1.04 rad/s	STS 3D-PTV	4 stationary
	0.79 rad/s	3D-PTV	2 one shot
	0.79 rad/s	STS 3D-PTV	4 stationary
	0.79 rad/s	PIV	5 one shot
	0.39 rad/s	PIV	5 one shot
	0.29 rad/s	PIV	5 one shot

Table 2: Experimental parameters and number of experiments executed for the three types of experimental configurations (i) free diffusion, (ii) deceleration wave like behavior and (iii) finite turbulence domain under the influence of system rotation

have been used for each case are summarized in table 2.

3 Results

The presentation of the results is split into two parts. The first part deals with the propagation of the turbulent/non-turbulent interface and in the second part the focus is on flow phenomena that occur due to the influence of rotation. This is the first time that the spreading of turbulence is analyzed systematically for the three cases of free diffusion and spreading under the influence of confinement and rotation. The Results obtained via PIV measurements are presented and compared with the theory of Oberlack and Günther (2003).

In the second part turbulence under the influence of system rotation is analyzed in more detail through three dimensional PTV measurements. The measurements were conducted in two different sizes of observation volumes. This allows to capture the large scale motions of the flow and to access velocity gradients and thus quantities like vorticity, Lagrangian and Coriolis acceleration. The presentation of the results, which characterize turbulence under the influence of system rotation, is structured in three main parts: (i) the evolution of the flow characteristics with distance from the grid, (ii) a detailed analysis of the quasi-2D flow regime and (iii) the dependency of the effects caused by system rotation on the rotational velocity.

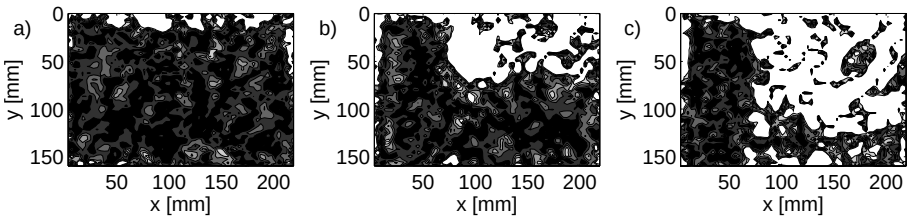

Figure 19: Vorticity magnitude maps for three snap shots (a) t=2 s, (b) t=8 s and (c) t=16 s

3.1 Propagation of the Turbulent/Non-Turbulent Interface

Oberlack and Günther (2003) studied three different cases of shear-free turbulent diffusion applying Lie-group (symmetry) analysis to the infinite series of multi-point correlation equations. In their analysis, turbulence is generated by a planar source of turbulent kinetic energy and diffuses normal to this plane, similar to the oscillating grid experiments described before. They derived: (i) a diffusion like solution, in which turbulence diffuses freely into the adjacent calm fluid, (ii) a deceleration wave like solution when there is an upper bound for the integral length scale and (iii) a finite domain solution for the case when rotation is applied to the system. One of the aims of this work was the experimental validation of these predictions.

In the next section the experimental results obtained via time-resolved 2D-PIV measurements for the propagation of the turbulent/non-turbulent interface in time are presented for the three cases, (i) free diffusion, (ii) fixed integral length scale and (iii) rotation.

3.1.1 Case(i): Free Diffusion

Since the results for the case in which turbulence diffuses freely agree well between the different research groups this experiment is used as a test case for the experimental setup within this study. In the experiments, the turbulence produced by the oscillating grid diffuses freely into the ambient flow below. Figure 19 shows magnitude maps of the vorticity for three snap shots, (a) t=2 s, (b) t=8 s and (c) t=16 s. The locations, where the vorticity magnitude exceeds the threshold value are marked in white color and represent the turbulent regions, whereas the black and gray areas represent irrotational regions. We see that in the initial stage of the experiment the turbulence is mainly confined within small regions in the proximity of the grid (Figure 19 a), whereas a few seconds later turbulent motion has noticeably spread out (Figure 19 b) and at $t = 16s$ the turbulent flow has reached the lower end of the field of view (Figure 19 c).

The propagation of the turbulent/non-turbulent interface is depicted in Figure 20, which shows its mean position, $H(t)$, as a function of time. All the experiments are presented in the form of a mean propagation curve, where the error bars represent the standard deviation between the different runs. Fig-

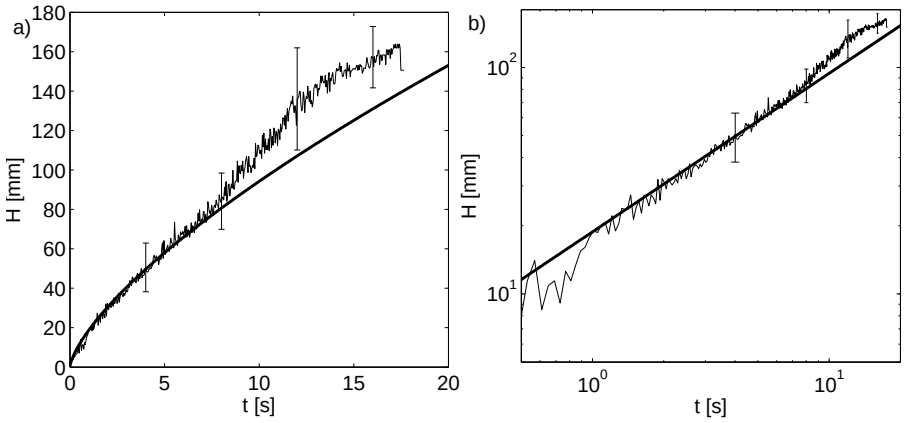

Figure 20: Mean position of the TNTI, H(t), versus time in linear (a) and logarithmic (b) axes, respectively. The data are averaged over the ten experimental runs and the error bars show their standard deviation, lines are the best fit to the data

ure 20 (b) shows that the behavior is of power law type and the data follow a straight line up to about t=10s. After that the behavior changes and this change of trend is due to the influence of the confinement, i.e., tank walls, as will be discussed in the section below. In other words, part of this experiment also belongs to case (ii), where the growth of the integral length scale of turbulence is bounded by the tank walls, which are analogous to a square tube with side length D=200 mm.

We recall that the prediction of Oberlack and Günther (2003) for the case of free diffusion is $H^{alg}(t) = \alpha\ell_0 \left[\frac{(t-t_0)\sqrt{K_0}}{\ell_0}\right]^{1/(m+1)} + y_0$. The measurements were analyzed by using regressional analysis based on this equation. The value of the virtual origin in space and time, y_0 and t_0, was allowed to vary within the interval of one grid oscillation, i.e. $\pm$ 4 mm and $\pm$ 0.11 s, and we excluded $t > 10$ s from the analysis. The parameters ℓ_0 and $\sqrt{K_0}$ were taken from the PIV measurements in the proximity of the grid as in Liberzon et al. (2009) and we obtained $\ell_0 \approx 15$ mm/s and $u' \approx 17$ mm/s, respectively. From the regression we obtained $\alpha = 1.52$, $t_0 \approx 0$, $n = 1/(m+1) = 0.6 \pm 0.1$, $y_0 = -4$ mm and a mean $R = 0.99$. When the virtual origin was fixed at the center of the grid stroke, the values obtained for n were generally closer to n=0.5 obtained by, e.g., Dickinson and Long (1982), Holzner et al. (2006). The results are therefore consistent with earlier measurements and the theory of Oberlack and Günther (2003).

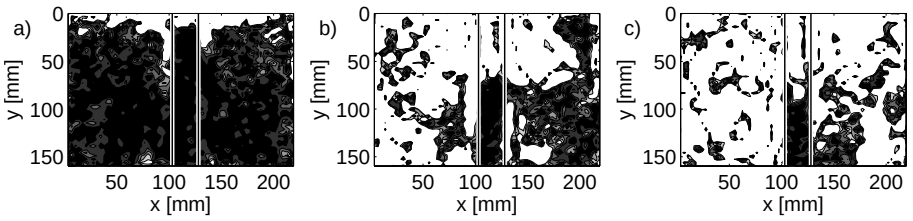

Figure 21: Vorticity magnitude maps for three snap shots a) t=2 s, (b) t=16 s and (c) t=32 s. The diameter of the cylinder placed in the center of the field of view is D=30 mm

3.1.2 Case(ii): Turbulent Diffusion with a Constant Integral Length Scale

Next, we placed a transparent cylinder vertically in the center of the tank and observed the propagation of the turbulent/non-turbulent interface inside the cylinder. The purpose is to limit the growth of the integral length scale of the turbulence, ℓ, through the confinement of the domain. In the initial period of the experiment the turbulent length scales are comparable to the mesh size of the oscillating grid and, as the experiment evolves, the length scales grow. Initially, ℓ is free to grow and the turbulence is expected to diffuse according to a power law, but at some point ℓ will become comparable to the diameter of the cylinder and can not grow beyond it. For a constant integral length scale, Oberlack and Günther (2003) predicted $H(t) \propto \ln(t - t_0)$. We tested three different cylinder diameters, D=20, 30 and 40 mm and, as noted above, the 'free' diffusion experiment is also discussed, D=200 mm. Figure 21 shows magnitude maps of the vorticity for three snap shots of an experiment with D=30 mm: (a) t=2 s, (b) t=16 s and (c) t=32 s. Already in the initial stage (Figure 21 a) we notice differences between the flow in the cylinder and the outer field. While in the outer field turbulent flow regions are visible close to the grid, the flow in the cylinder is mostly irrotational. The difference becomes clearer for later times. In Figure 21 (b) we observe that in the cylinder the turbulent/non-turbulent interface reached approximately one third of the total length, while outside we clearly distinguish turbulent regions beyond that distance. In Figure 21 (c) the turbulent/non-turbulent interface reached about one half of the total length, while outside the flow is in turbulent motion everywhere. The propagation of the turbulent/non-turbulent interface under the influence of confinement is presented in Figure 22 for all four tube diameters (D= 20-200 mm). The arrow plotted in the figure indicates results for increasing tube diameter. Note that the considered time span of the experiments is about one decade longer than in the previous case, because the diffusion of the turbulence inside the tube is much slower than in case (i). It is apparent that for decreasing D the propagation speed decreases. Figure 22 also shows that for D=20, 30 and 40 mm at some point in time the propagation comes to rest, i.e., H(t) reaches a plateau. At these particular locations the local Reynolds number approaches unity (throughout the logarithmic regime, ℓ remains con-

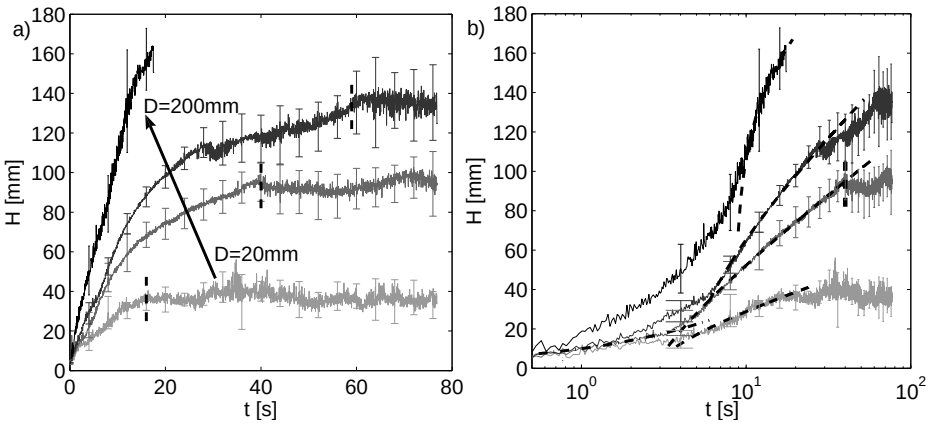

Figure 22: Mean position of the TNTI, H(t), versus time for the four diameters, D=20 mm, D=30 mm, D=40 mm and D=200 mm (from light gray to black) in linear (a) and logarithmic (b) axes, respectively. The lines represent the best fits of equation 32 to the data. The vertical dashed lines indicate the upper bound of the fit interval.

stant, but u' decreases and therefore Re decreases). Thus we assume that the propagation of the turbulent/non-turbulent interface at some point stops because viscous and inertial forces come to a balance. This is also consistent with the arguments of Thompson and Turner (1975)[1] Our attention is on the intermediate regime (between power law and plateau) that becomes more apparent in the semi-logarithmic representation, Figure 22 (b). In this representation, a power law will show positive curvature, whereas a logarithmic behavior will show negative curvature (not a straight line due to the non-zero time offset, t_0). For this case we used $H^{log}(t) = \beta \ell_c \ln\left[\frac{(t-t_0)\sqrt{K_0}}{\ell_c}\right] + y_0$ for the regression analysis in the intermediate regime, whereas a power law was fitted like above for the initial times where a power law applies. The intersection between the two regimes determines the parameters t_0 and y_0, which (together with β and ℓ_c) are free parameters in the regression analysis. As for case(i) the parameter $\sqrt{K_0}$ was taken from the PIV measurements in the proximity of the grid and we obtained $u' \approx 17$ mm/s for all cases. The results from regression analysis are summarized in Table 3 and confirm that the experiments agree very well

[1]Thompson and Turner (1975) proposed that for the case of turbulent diffusion from a planar source, at high Reynolds numbers the energy is dissipated by "inertial shear" and write $du^3/dy = -Bu^3/\ell$, where u and ℓ are the integral velocity and length scales of turbulence and B is a constant of order unity. The LHS of the equation is the divergence of the flux of turbulent energy and the RHS can be interpreted as an eddy viscosity of order $u\ell$ acting on a shear of order u/ℓ, i.e., $u\ell(u/\ell)^2 = u^3/\ell$. With $\ell \propto y$, case (i), the equation yields a power law for the propagation of the turbulent/non-turbulent interface and with $\ell = const$, case (ii), the equation yields a logarithmic law, consistent with the prediction of Oberlack and Günther (2003) and our measurements. At Reynolds number of order unity, $u\ell$ is of order ν, that is, inertial and viscous dissipation are of the same order and the equation given above is no longer valid.

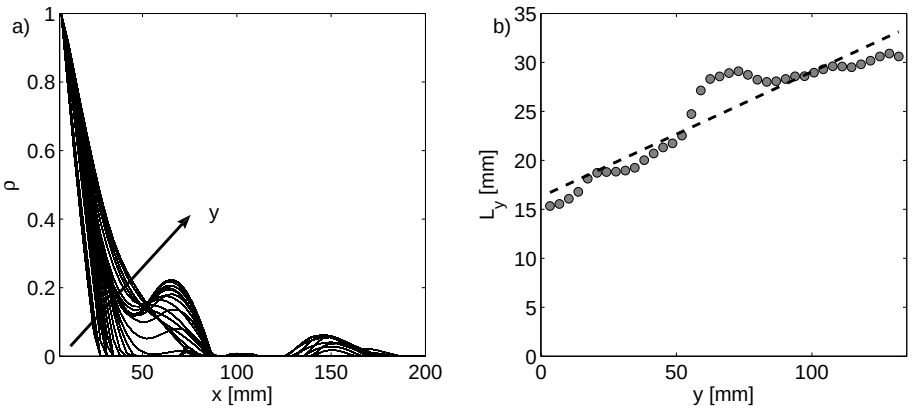

Figure 23: Spatial (horizontal) autocorrelation of the vertical velocity component for increasing distance from the grid (a) and resulting integral length scale with dashed trend line (b)

with the prediction of Oberlack and Günther (2003). The results indicate that ℓ_c and y_0 increase with D, but additional experiments (also for intermediate diameters) are needed to clarify this trend. The results are consistent with the observation that the integral length scale increases with distance from the source (e.g., Liberzon et al. (2009)).

The integral length scale of the turbulence for the case of free diffusion was estimated through spatial autocorrelation of the vertical velocity component. The result is shown in Figure 23 (a) for varying vertical coordinate. Figure 23 (b) displays the resulting integral length scale as a function of the distance to the grid and we note that L increases linearly with distance. This is consistent with the similarity hypothesis (Long (1978)) and related experiments in the literature (e.g., Hopfinger and Toly (1976)).

3.1.3 Case(iii): Turbulent Diffusion under the Influence of Rotation

Finally, we consider the case of rotation applied to the system. We conducted a set of preliminary flow visualization experiments by using Pearlescence. The rotation was started by increasing slowly the angular velocity towards the desired value and the recording was started 15 min after reaching this velocity. In Figure 24 (a) we show a snapshot for t=2 s and note that the spreading is similar to case (i) for the initial moments in time. In the center of the image a starting vortex is visible and indicates that a time span of 15 min is not sufficient for the fluid to reach solid body rotation. In additional visualizations with a span of 30 min this streak disappeared and this is the protocol we used for the PIV measurements presented below. From Figure 24 (b) we note that, similar to the observations of Dickinson and Long (1982), very quickly tube-like structures start to form at the boundary of the turbulent layer. These columnar structures propagate towards the bottom of the tank (see, e.g., Hopfinger et al. (1982)), while the turbulence remains confined within a small region close to

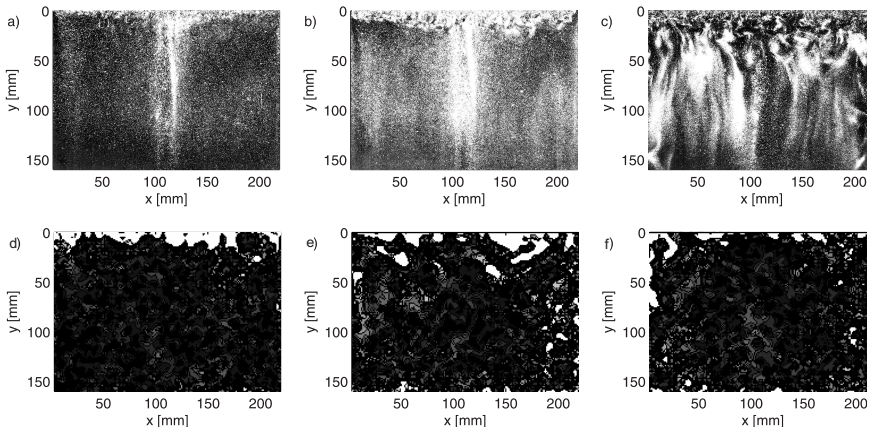

Figure 24: Vorticity magnitude maps (a-c) and Pearlescence visualization (d-f) for three snap shots for the experiment with angular velocity 0.79 rad/s, (a,d) t=2 s, (b,e) t=16 s and (c,f) t=32 s

the grid. The flow was finally observed to reach an equilibrium state between the turbulent region, where the motion is fully three-dimensional and a region governed by waves, where the flow is more characterized by a two-dimensional state (Figure 24 c). More precisely, in all experiments the turbulent region was observed to grow at first (at $t \sim$ 1-10 s), then to slightly retract (at $t \sim$ 10-30 s) and finally to reach an equilibrium depth, y^*. Figure 24 (d-f) shows magnitude maps of the vorticity for three snap shots of an experiment with angular velocity of 0.79 rad/s for three time instances, t=2, 16 and 32 s. In the initial period (Figure 24 d) we observe that the diffusion of the turbulence is similar to case (i). In a second stage due to inertial waves vortical columns start to form. Their axis of rotation is approximately parallel to the axis of rotation of the table, i.e. parallel to the vertical coordinate. Therefore, the out-of-plane vorticity component remains almost unaffected by the waves and can be used to detect the outer edge of the turbulent region, where the motion is fully three-dimensional. This is confirmed by comparing the top (visualization) and bottom (PIV) panels of Figure 24. The vorticity is concentrated in the upper region, whereas in the region governed by waves, only a few noisy patches appear. In Figure 24 (e) we note that the turbulent region reaches about one third of the vertical extent of the field of view. As mentioned before, the turbulent region then retracts and ultimately approaches y^* (Figure 24 f). Figure 25 depicts the propagation of the outer edge of the turbulent region in time for the four angular velocities. We note that after about 10-30 s, depending on the angular velocity, the turbulent region reaches y^*. The faster the rotation, the smaller is y^*. The measured values (Figure 25) of the equilibrium depth are y^*= 12.99, 18.29, 36.80 and 55.06 mm for the angular velocities Ω= 1.57, 0.79, 0.39, and 0.29 rad/s. The prediction of Oberlack and Günther (2003) for case (iii) is $H(t)^{exp} = \delta\tau_\Omega\sqrt{K_0}\exp(-\beta t/\tau_\Omega) + y_0$ and we confirm the theory only in the sense that ultimately an equilibrium depth is reached. Due to the observed

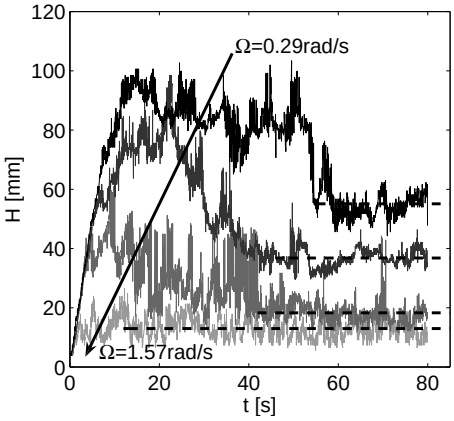

Figure 25: Mean position of the TNTI, H(t),versus time with the table rotating at four constant angular velocities, 0.29 rad/s, 0.39 rad/s, 0.79 rad/s and 1.57 rad/s (from black to light gray)

expansion and later retraction of H(t) the exponential function is not representative of the initial stages of the experiment and therefore we omitted the fit to the data in this case. The discrepancy between experiment and theory could be due to the finite depth of the tank. In fact the observed time, when H(t) starts to retract, roughly matches with the time it takes for the inertial waves to reach the bottom of the container. The local Rossby numbers corresponding to y^*, $Ro(y^*) = u(y^*)/(2\Omega\ell(y^*))$, are 0.37, 0.34, 0.21 and 0.11 for the angular velocities 0.29, 0.39, 0.79 and 1.57 rad/s, respectively.

3.1.4 Summary of the Spreading of Turbulence

In summary, the diffusion of shear-free turbulence away from a planar energy source was investigated experimentally for three different cases: (i) the turbulence diffuses freely into the adjacent fluid at rest, (ii) there is an upper bound for the integral length scale and (iii) rotation is applied to the system. An oscillating grid drives the turbulence and the flow is analyzed by using time resolved 2D-PIV measurements. The results confirm the predictions obtained via symmetry analysis by Oberlack and Günther (2003) for case (i) and (ii). In particular, for case (i) we observe that the turbulent/non-turbulent interface propagates according to a power law, $H \propto t^n$, where n is estimated to be $n = 0.6 \pm 0.1$. For case (ii) we confirm that the behavior changes to a logarithmic law with $H \propto \ell_c ln(t - t_0) + y_0$ and the results indicate that ℓ_c and y_0 increase with D, but additional measurements are necessary to clarify these trends. Finally, for case (iii) we confirm the theory only in the sense that turbulence remains confined within a finite domain. We note that the domain size decreases with increasing angular velocity. The present study is restricted to the validation of the theory in terms of first order quantities only. The verification of correlations as proposed, e.g., in Oberlack and Günther (2003) is demanding

case (i)		200 mm			
	α	1.52			
	ℓ_0 [mm]	15			
	$\sqrt{K_0}$ [mm/s]	17			
	t_0 [s]	0			
	$\frac{1}{(m+1)}$	0.6			
	y_0 [mm]	-4			
	R	0.97			
case (ii)		200 mm	40 mm	30mm	20mm
	β	1.40	0.92	0.96	0.62
	ℓ_c [mm]	22.0	40.0	29.7	19.9
	t_0 [s]	8.5	2.8	1.3	1.8
	$\sqrt{K_0}$ [mm/s]	17	17	17	17
	y_0 [mm]	101.7	25.0	6.4	4.7
	R	0.95	0.99	0.99	0.92
case (iii)		1.57 rad/s	0.79 rad/s	0.39 rad/s	0.29 rad/s
	y_0 [mm]	13	18	37	55

Table 3: Fitting parameters for the three types of experiments (i) free diffusion, (ii) diffusion with constant integral length scale and (iii) diffusion under the influence of rotation

as it relates conventional (purely Eulerian) statistics, e.g. R_{ij} , to conditional statistics, e.g., R_{ij} (i.e., conditional averages with respect to the TNTI). Our measurements are 2D only and preliminary tests showed that a larger (and possibly 3D) data set is needed. Therefore measurements of higher order quantities (e.g., 2nd order correlation tensor) will be part of future work.

3.2 Turbulence under the Influence of System Rotation

This part of the results deals with more general effects, which system rotation has on shear-free turbulence. These effects relate to the spatial transition region from three-dimensional to quasi-2D turbulence and associated columnar structures. The first part illustrates the dependency of large and small scale quantities on the distance from the energy source and a comparison to the non-rotating case is made. The emphasis is on magnitudes of quantities, but also on geometrical statistics, like alignment between certain vectors and the axis of rotation. Thereafter, results on the spatial transition region between three-dimensional and quasi-2D turbulence are presented and compared to its counterpart in the non-rotating case, the turbulent/non-turbulent interface. Next, the quasi-2D flow region and associated columnar vortices are analyzed in more detail. Again, this is done on the level of large and small scale quantities. The last section of the results deals with the influence of the magnitude of the rotational velocity on the alignment of the flow with the axis of rotation as well as on the small scale quantities.

3.2.1 Mean Flow

It is well known that in oscillating grid chambers some weak mean flow can arise. One can decompose the total velocity into mean and fluctuating parts (Reynolds decomposition) as,

$$u^{'} = u - < u > \tag{25}$$

For the case of the regular grid and, generally, in all the experiments where system rotation is applied, the magnitudes of the mean velocities are about an order of magnitude smaller than the fluctuating parts. In the experiments with the fractal grid and without system rotation, however, the mean velocities and fluctuating velocities were found to be of the same order. Therefore, for this experiment we subtracted the mean velocity from the total one, so that only the fluctuating velocity field remained. An instantaneous snapshot of the original velocity field is displayed in Figure 26 (a) with the fluctuating velocity field, $u^{'}$, in Figure 26 (b) for comparison.

3.2.2 Qualitative Effects

The columnar vortices and the spatial transition from 3D in the proximity of the grid to quasi-2D flow in the lower regions of the tank are qualitatively illustrated in Figure 27 by the snapshots from the preliminary Pearlescence flow visualization experiments at angular velocities of 1.57 rad/s (a), 1.05 rad/s (b) and 0.79 rad/s (c), see Table2. The flow was forced with the regular grid, see Section2.1. We note that the 3D turbulent region is confined in a rather narrow region close to the grid. With higher angular velocities the number of columnar vortices appears to increase, while their diameter decreases and (as mentioned above) y* becomes smaller. The aim now is to study the spatial transition

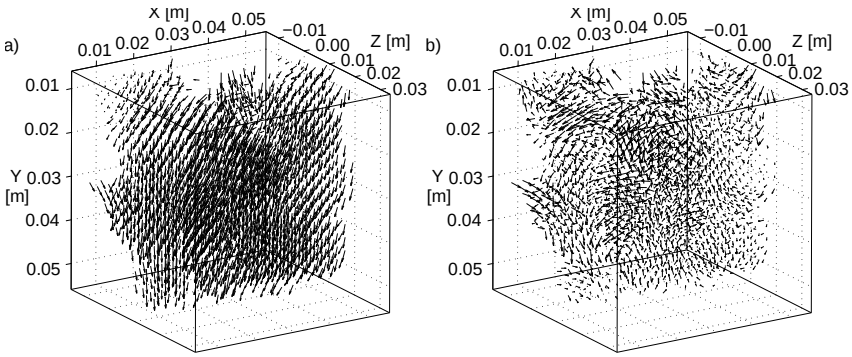

Figure 26: Measured instantaneous velocity field, u, (a) and fluctuating velocity field, $u^{'}$, (b) from an experiment without rotation

region from the 3D turbulent to the quasi-2D flow and therefore we preferred to increase y*, so that the 3D region is better accessible with 3D measurements, while maintaining the same rotation speeds. In principle the 3D region will grow with stronger forcing, but since the limits of the linear motor were already reached we decided to change the grid and use a fractal one. Thus with the same stroke and frequency of the motor, more energy is put into the flow compared to the regular grid.

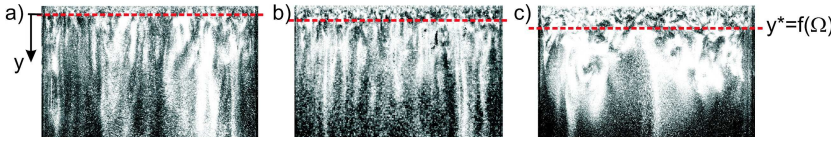

Figure 27: Flow visualization using Pearlescence at rotation rates of 1.57 rad/s (a), 1.05 rad/s (b) and 0.79 rad/s (c)

Now we analyze how this qualitative observations are reflected in detailed measurements of the 3D flow field. While Pearlescence is visualized over the whole width of the tank 3D-PTV is employed in an observation volume, which is located horizontally in the center of the tank and vertically underneath the lowest position of the oscillating grid. The distance y^*, after which the flow is observed to become quasi-2D is located approximately in the vertical center of the observation volumes. First, we compare the results of two 3D-PTV experiments, namely the one in a rotating setting at an angular velocity of 1.05 rad/s and the experiment without rotation, where the flow reached statistical steady state, Table2.

After the whole flow field was visible in Figure 27 the next figure focuses on the region underneath the lowest grid position in the middle of the tank, i.e. the large 3D-PTV observation volume. In order to get a qualitative impression of the effects, which system rotation has on the flow structure, we show two snapshots, one for the non-rotating case (top) and one for a rotational velocity of 1.05 rad/s (bottom) in Figure 28. In both experiments the flow has reached

a steady state. The right hand side shows enstrophy iso-surfaces at a level of $\omega^2 = 8\ s^{-2}$ together with the three dimensional velocity vector field. On the left hand side slices of enstrophy contours with velocity vectors superimposed on the horizontal planes are presented. For the visualization purposes the Eulerian data have been interpolated to a resolution that is about twice as fine as the effective resolution of the measurement. That is, we used a grid spacing that is about half the interparticle distance ($51 \times 51 \times 51$ points). In the data from the experiment without system rotation, regions of high enstrophy are uniformly distributed over the domain. On the other hand, for the case with system rotation (Figure 28 bottom) regions of high enstrophy are mainly located in the upper part of the large observation volume except for a region close to the center, where enstrophy extends into the lower part of the observation volume. The iso-surfaces in the upper half of the domain are qualitatively similar to the non-rotating case and the velocity vector field shows a random orientation. In the lower regions of the observation volume on the other hand, the velocity vectors are primarily aligned in the horizontal plane.

This is the first time that the quasi-2D regime of the flow could be visualized three-dimensionally together with the 3D-turbulent flow in the proximity of the energy source and the transition between the two. At closer examination the horizontally orientated velocity vectors in the quasi-2D region form a vortex column. The region of high enstrophy, which reaches into the lower part of the domain coincides with the center of the vortex column.

3.2.3 Dependence of Quantities on the Distance from the energy source

To analyze the transition from 3D-turbulence to quasi-2D flow in the large observation volume we condition the data on the distance to the energy source, namely the oscillating grid. Therefore the coordinate normal to the oscillating grid, the y-axis, is subdivided into eleven bins and the conditional average is calculated in time and over the horizontal slices, i.e. $< q(y) >=< q(x,y,z,t) >_{x,z,t}$. Also, from each slice a PDF curve is calculated to characterize the change in the distribution of the significant flow quantities with distance from the grid. The gray shading of these curves represents increasing y (see Figure 4). Figure 29 (a) shows the conditional average of the magnitude of the horizontal (black) and vertical (gray) components of velocity over distance from the energy source, $< |u_{hor}(y)| >$ and $< |u_{ver}(y)| >$, for the experiment without rotation (solid) (compare Figure 28 top) and the experiment at an angular velocity of 1.05 rad/s (dashed) (compare Figure 28 bottom). For the former both components of velocity attenuate with distance from the grid, which is in agreement with the findings of Silva and Fernando (1994) who predict a $u \propto y^{-1}$ relationship. On the other hand, under the influence of rotation the horizontal velocity increases over y while the vertical velocity decreases. This behavior illustrates the change in the flow pattern, namely the formation of a quasi-2D regime, which is dominated by columnar structures aligned with the rotational axis. In this regime the vertical velocity is attenuated while the horizontal velocity gets

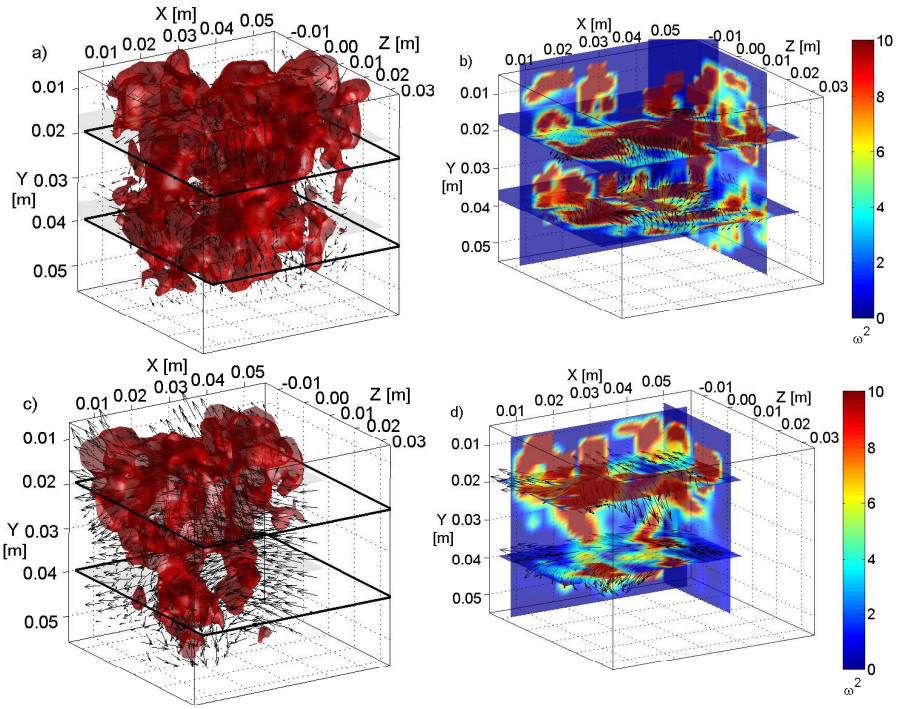

Figure 28: Enstrophy iso-surfaces with superimposed velocity vector field (left) and slices of enstrophy contours with superimposed Eulerian velocity vector field (right) from an experiment without rotation (top) and with a rotational velocity of 1.05 rad/s (bottom).

amplified. The vertical velocity in the proximity of the grid is higher in the rotational experiment solely because the mean flow could only be subtracted from the non-rotating experiment (Section 3.2.1). For a closer examination of the distribution of the velocities the corresponding PDFs are presented in Figure 30 and Figure 31, respectively for the experiment without rotation (a) and for an angular velocity of 1.05 rad/s (b). The data represents the steady states, when the flows in both kinds of experiments are fully evolved. Both the attenuation of the magnitude of the horizontal velocity with distance from the energy source in the experiment without rotation as well as the increase in the rotating experiment are found in the PDFs, Figure 30. The behavior of the horizontal velocity with distance from the grid corresponds to the transition to the quasi-2D region of the flow. This increase also attenuates with distance from the energy source. The magnitude of the horizontal velocity in the proximity of the grid is approximately equal for the two types of experiments. But already for short distances from the grid the magnitude of the horizontal velocity becomes higher in the experiment under the influence of rotation until it is approximately twice as high as in the experiment without rotation in the lower region of the observation volume. This demonstrates that rotation transfers energy to the horizontal

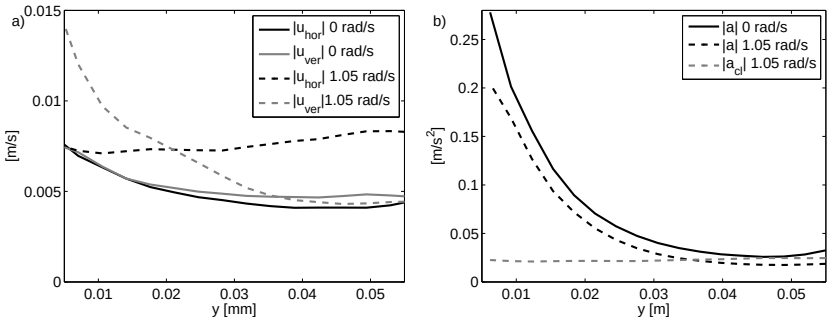

Figure 29: Average of the magnitude of the horizontal and vertical components of velocity (a) and of the magnitude of the Lagrangian and Coriolis accelerations (b) over the direction normal to the forcing plane, y, from an experiment without rotation (solid) and with a rotational velocity of 1.05 rad/s (dashed).

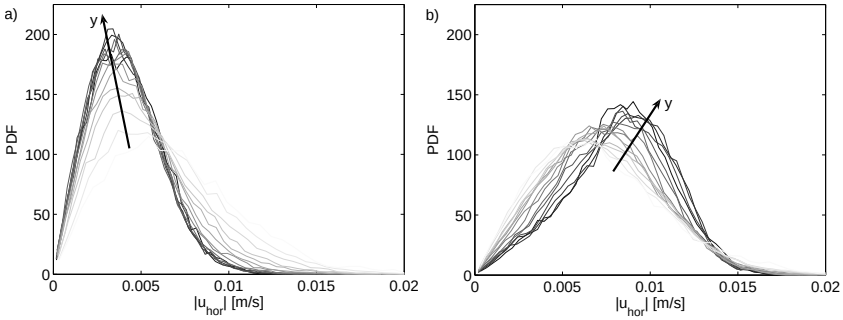

Figure 30: PDF of the magnitude of horizontal velocity from an experiment without rotation (a) and with a rotational velocity of 1.05 rad/s (b). The gray shading represents increasing y, where y is the coordinate normal to the forcing plane and parallel to the axis of rotation.

components.

A strong difference between the non-rotating and the rotating experiment is visible in the PDF curves of the vertical velocity. While this velocity component decreases only slightly with distance from the grid in the experiment without rotation it becomes suppressed with distance from the grid in the rotating data, i.e., the values become more concentrated at lower velocities. This effect does not increase further after a certain distance from the grid, namely in the quasi-2D regime. Therefore it can be assumed that the flow properties do not change significantly after the quasi-2D state has been reached (compare with the following alignments). More evidence for this claim will be shown below, when the results for different angular velocities are presented. The magnitude of the vertical velocity in the proximity of the grid appears higher in the experiment under the influence of rotation. As mentioned above this is caused by the subtraction of the mean flow from the velocity data of the experiment without rotation. The curves for $< |a(y)| >$ and $< |a_{cl}(y)| >$ are displayed in Figure 29 (b) for the

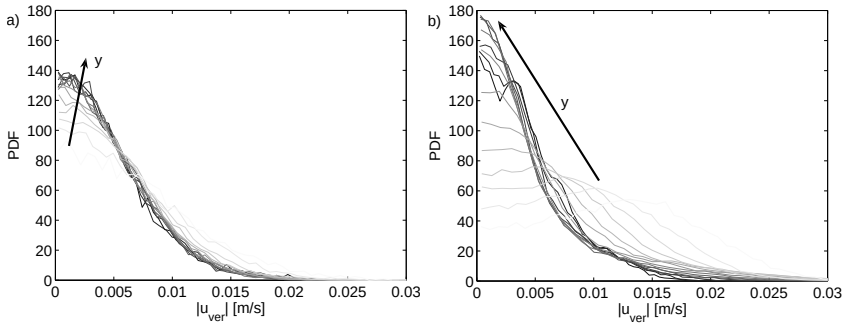

Figure 31: PDF of the magnitude of vertical velocity from an experiment without rotation (a) and with a rotational velocity of 1.05 rad/s (b). The gray shading represents increasing y, where y is the coordinate normal to the forcing plane and parallel to the axis of rotation.

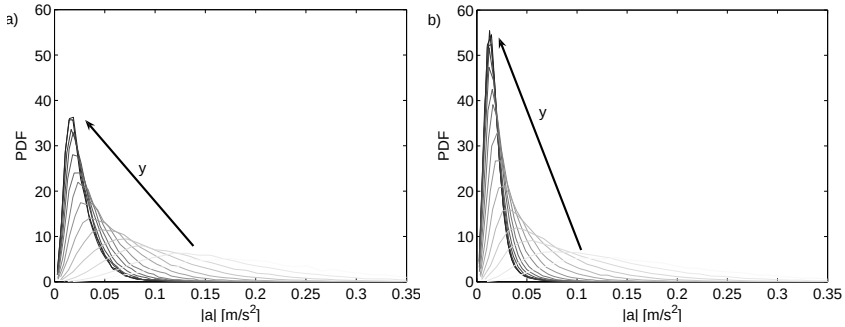

Figure 32: PDF of the magnitude of Lagrangian acceleration from an experiment without rotation (a) and with a rotational velocity of 1.05 rad/s (b). The gray shading represents increasing y, where y is the coordinate normal to the forcing plane and parallel to the axis of rotation.

two types of experiment. While qualitatively similar $< |a(y)| >$ is noticeably lower in the experiment under the influence of rotation. This can also be seen in Figure 32 where the values of the corresponding PDFs go to zero with distance from the energy source. Thus the magnitude of the Lagrangian acceleration declines with distance from the grid. However, the magnitude of the Coriolis acceleration, which is significantly lower than the Lagrangian one in the proximity of the energy source increases with distance from the source. In the lower part of the observation volume the Coriolis acceleration reaches the magnitude of the acceleration in the non-rotating experiment and thus becomes dominant over the Lagrangian acceleration. The corresponding PDFs for the magnitude of the Coriolis acceleration can be found in Figure 36 (a).

The cosine of the angle between the vectors of velocity and the axis of rotation is close to zero if the velocity is predominately aligned in the horizontal direction and towards plus/minus one if the alignment coincides with the axis of rotation, i.e., the vertical axis. The same is true for the cosine of the angle

between the vectors of vorticity and the axis of rotation. It is zero for a vortex, which spins around the horizontal axis and plus/minus one for a vortex, which spins around a vertical axis. Therefore these two invariants are utilized to identify alignments of the flow, namely the vortex columns, which are formed by the rotational forces. The conditional average of the cosine of the angle between the

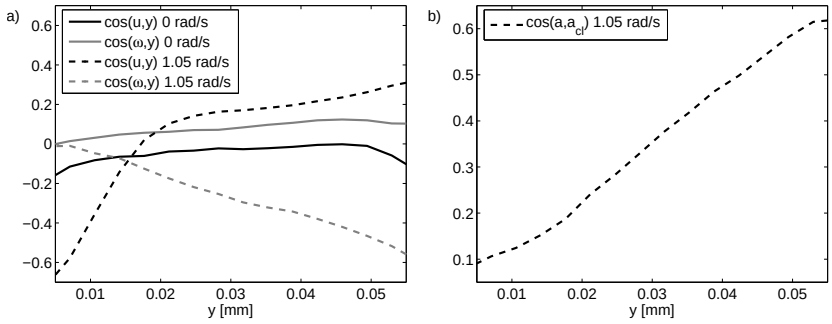

Figure 33: Average of the magnitude of the cosine of the angle between the vectors of velocity and the axis of rotation and vorticity and the axis of rotation (a) and between the vectors of Lagrangian and Coriolis acceleration (b) over the direction normal to the forcing plane, y, from an experiment without rotation (solid) and with a rotational velocity of 1.05 rad/s (dashed).

vectors of velocity and rotational axis (black) and vorticity and rotational axis (gray) over distance from the energy source, $< cos(u, y) >$ and $< cos(\omega, y) >$, for non-rotating (solid) and of the rotational (dashed) experiment are presented in Figure 33 (a). For the experiment without rotation the curves for both invariants lie close to zero, which suggests that both $cos(u, y)$ and $cos(\omega, y)$ are randomly distributed. The corresponding PDFs in Figure 34 (a) reveal that this is in fact the case since the values are almost equally distributed over the whole range of the cosine. However, The velocity vector is slightly more aligned with the vertical direction.

In Figure 33 (a) the curve of $< cos(u, y) >$ is negative in the proximity of the energy source but then increases and becomes slightly positive. The corresponding PDFs in Figure 34 (b) reveal that the cosines become shifted towards zero for increasing y. The maxima in the functions around zero, which increase with distance from the energy source reflect the preferential alignment of the velocity vector with the plane normal to the axis of rotation. This result can be interpreted as an influence of the columnar structures, since the velocity is primarily orientated in the horizontal plane inside the vortex columns. The mean flow in the quasi-2D region of the large observation volume is away from the grid because the centers of the PDFs are positive. This is in agreement with the detected anticyclonic vortex column and the downwards fluid transport, which is associated with them, Godeferd and Lollini (1998). The same analysis has been performed on the level of small scale quantities, i.e. vorticity. In addition to the conditionally averaged curves in Figure 33 (a) PDFs of the angle between

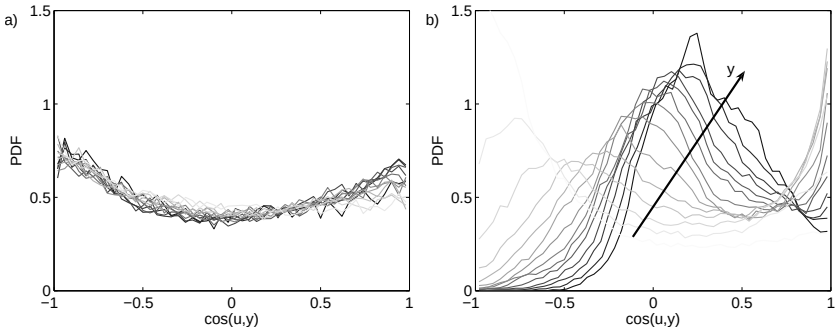

Figure 34: PDF of cosine of the angle between the vectors of velocity and axis of rotation from an experiment without rotation (a) and with a rotational velocity of 1.05 rad/s (b). The gray shading represents increasing y, where y is the coordinate normal to the forcing plane and parallel to the axis of rotation.

the vorticity vector and the axis of rotation for data from an experiment without and with rotation are shown in Figure 35 (a) and (b), respectively. For the non-rotating data the PDFs are almost flat but some degree of forcing imprint seems to be maintained even at the small scale level. Similarly to the alignment of the velocity this shows that the conditional average of the cosine of the angle between the vectors of vorticity and the axis of rotation is close to zero because the data are randomly distributed over the whole range of the cosine. Under the influence of system rotation, Figure 35 (b), this behavior changes drastically and the PDFs become more and more skewed towards minus one for increasing y, illustrating the preferential alignment of the vorticity vector with the axis of rotation in the quasi 2D region of the flow. This behavior is also visible in the corresponding curve for the conditional average, $< cos(\omega, y) >$, which goes towards minus one. The result is consistent with the previous one, the vorticity vector being normal to the velocity by definition. A quantitative impression

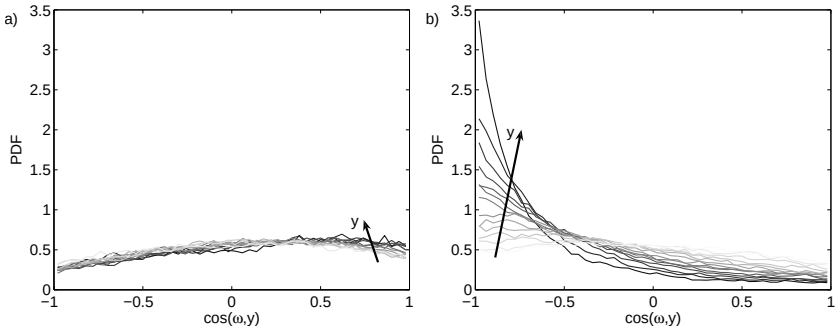

Figure 35: PDF of the cosine of the angle between the vectors of vorticity and axis of rotation from an experiment without rotation (a) and with a rotational velocity of 1.05 rad/s (b). The gray shading represents increasing y, where y is the coordinate normal to the forcing plane and parallel to the axis of rotation.

of the influence, which rotation has on the acceleration can be obtained from the cosine of the angle between the vectors of Lagrangian and Coriolis accelerations. Here a value of one corresponds to an alignment between the two accelerations and thus a cumulative influence, which rotation has on the fluid's motion. On the other hand if this cosine turns zero both accelerations are not aligned and inertial forces, e.g., directed by pressure gradients or the energy source, are dominant. Thus the transition from 3D to quasi 2D can be further characterized by the alignment of these vectors, i.e. the Lagrangian and Coriolis acceleration. The conditional average, $< cos(a, a_{cl}) >$, is given in Figure 33 (b) for the experiment under the influence of rotation. The curve increases with y, which demonstrates that the alignment between the two accelerations grows with distance from the energy source. Also the corresponding PDFs in Figure 36 are increasingly skewed towards one for increased distance from the grid. Thus Lagrangian and Coriolis acceleration are strongly aligned with each other in the quasi-2D part of the flow. However, also in the nominally 3D-turbulent part of the flow the orientation of the two vectors is not completely random but slightly aligned with each other. This slight alignment in the proximity of the grid can also be observed in the PDFs of $cos(\omega, y)$ in Figure 35 (b), which suggest that the small scales are effected more by system rotation, i.e. at higher Rossby numbers than the large scale quantities.

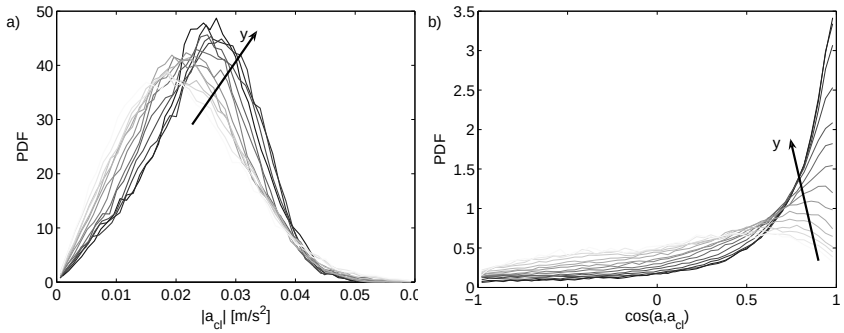

Figure 36: PDF of the magnitude of Coriolis acceleration (a) and cosine of the angle between the vectors of Lagrangian and Coriolis acceleration (b) from an experiment with a rotational velocity of 1.05 rad/s. The gray shading represents increasing y, where y is the coordinate normal to the forcing plane and parallel to the axis of rotation.

So far the behavior of the large scale quantities and geometrical alignments with distance from the grid have been characterized for experiments without and with the influence of rotation. Next we look at small scale quantities like enstrophy and strain. The small scale quantities are analyzed from the highly resolved measurement taken in the small observation volume. The first small scale quantity to be examined is entrophy, ω^2. The PDFs illustrating the distribution of enstrophy are presented in Figure 37 (a) for the non-rotating experiment and at a rotational velocity of 3.14 rad/s in Figure 37 (b). For both experiments the

curves demonstrate that enstrophy decreases with distance from the grid. It is also apparent that the enstrophy level is considerably lower in the experiment under the influence of rotation.

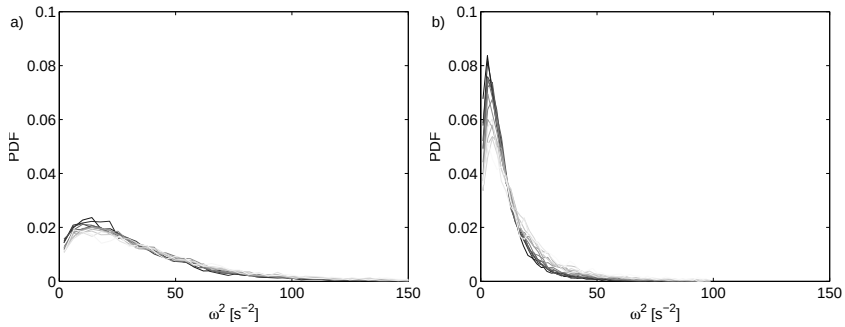

Figure 37: PDF of enstophy from an experiment without rotation (a) and with a rotational velocity of 3.14 rad/s (b). The gray shading represents increasing y, where y is the coordinate normal to the forcing plane and parallel to the axis of rotation.

In homogeneous 3D-turbulence enstrophy and strain are connected by a factor of two, $< \omega^2 >= 2 < s^2 >$. The following figures show strain multiplied by a factor of two to allow for an estimate on how 3D-turbulent the flow is. Qualitatively the behavior of $2s^2$ is exactly the same as for enstrophy. The ratio between enstrophy and strain, $\omega^2/2s^2$, is 0.93 for the non-rotating experiment and 0.97 under the influence of rotation. Both ratios are close to the theoretical value of one. However, the direct comparison reveals that the magnitude of strain is slightly higher under the influence of rotation. The corresponding PDFs for strain can be found in Figure 38. These lower magnitudes of enstrophy and strain in the experiment under the influence of rotation are an indicator for a lower turbulent energy in the flow. They therefore show the organizing effect, which rotation has on the small scales. The question arises how system rotation influences the vortex stretching mechanism. The PDFs of the cosine of the angle between the vorticity and the vortex stretching vectors, $cos(\omega, W)$, are presented in Figure 39 (a) for the non-rotating and in Figure 39 (b) for the rotating experiment. In the former the PDFs are skewed towards one, which reflects the dominance of vortex stretching for three dimensional turbulence. The PDFs for the different distances from the grid all fall on top of each other, i.e. $cos(\omega, W)$ is independent of distance from the grid, y, in this region of the flow. In general the PDFs of $cos(\omega, W)$ from the experiment under the influence of rotation are less skewed towards one and become almost symmetric around zero (an effect which is discussed further below with analogous plots from experiments at higher rotational velocities). The decrease of the positive skewness implies an increase of vortex compression at the expense of vortex stretching events. Both effects are already present in the upper part of the small observation volume and become more pronounced with further distance from the

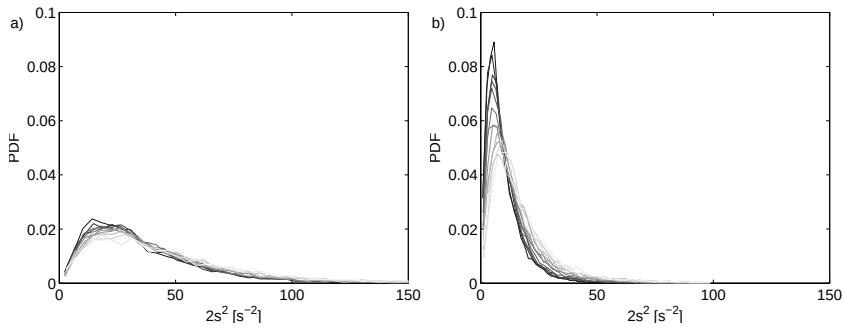

Figure 38: PDF of strain by a factor of two from an experiment without rotation (a) and with a rotational velocity of 3.14 rad/s (b). The gray shading represents increasing y, where y is the coordinate normal to the forcing plane and parallel to the axis of rotation.

grid, i.e. in the quasi-2D region of the flow. As described in Section 1.4, vorticity,

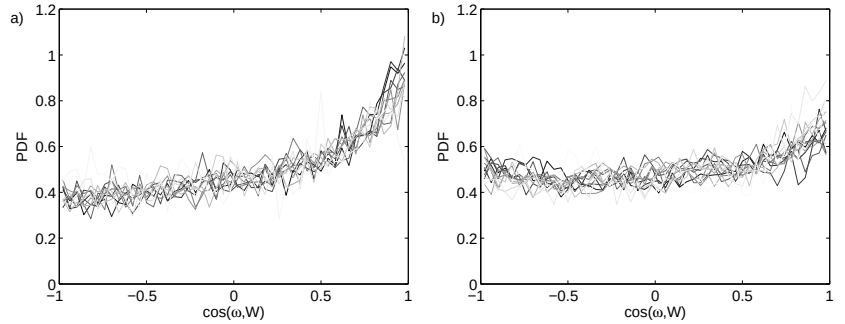

Figure 39: PDF of the cosine of the angle between the vorticity and the vortex stretching vectors from an experiment without rotation (a) and with a rotational velocity of 3.14 rad/s (b). The gray shading represents increasing y, where y is the coordinate normal to the forcing plane and parallel to the axis of rotation.

enstrophy production, vortex stretching and the strain eigenframe are connected by the equation $\omega_i\omega_j s_{ij} = \omega^2\Lambda_i cos^2(\omega,\lambda_i) \equiv \omega \cdot W = \omega W cos(\omega, W)$. Therefore the PDFs of $cos(\omega,\lambda_i)$ in Figure 40 (left) and Λ_i in Figure 40 (right) provide information for a deeper insight into the vortex stretching and compression mechanisms. Graphs are displayed for an experiment without rotation (solid) and at a rotational velocity of 3.14 rad/s (dashed). For the experiment under the influence of rotation the PDFs were calculated for different distances from the grid and the corresponding curves are presented for the top (Figure 40 a, b), mid (Figure 40 c, d) and bottom (Figure 40 e, f) plain of the small observation volume.

The PDFs from the experiment without rotation display the alignments known for 3D-turbulence as they were discussed in Section 1.4: (i) the vorticity vector is predominantly aligned with the intermediate strain eigenvector, (ii) the

alignment between ω and λ_1 is larger than between ω and λ_3, (iii) $\Lambda_1 > 0$, Λ_2 features both positive and negative values but is positively skewed and $\Lambda_3 < 0$ (see, Siggia (1981), Ashurst et al. (1987) and Tsinober (1998)). Hence enstrophy production and vortex stretching are positive in this flow. However the PDFs of $cos(\omega, \lambda_i)$ are normally further separated than the curves in Figure 40 (left), i.e. the alignment between ω and λ_1 is usually stronger. The reason might be the spatial resolution, which is still low for the measurement of these second order quantities. Nevertheless the curves are still in agreement to others (e.g.,Lüthi (2002), Tsinober (2001)) and therefore reliable for qualitative interpretation. Figure 40 (a) compares the alignments close to the grid. The PDFs

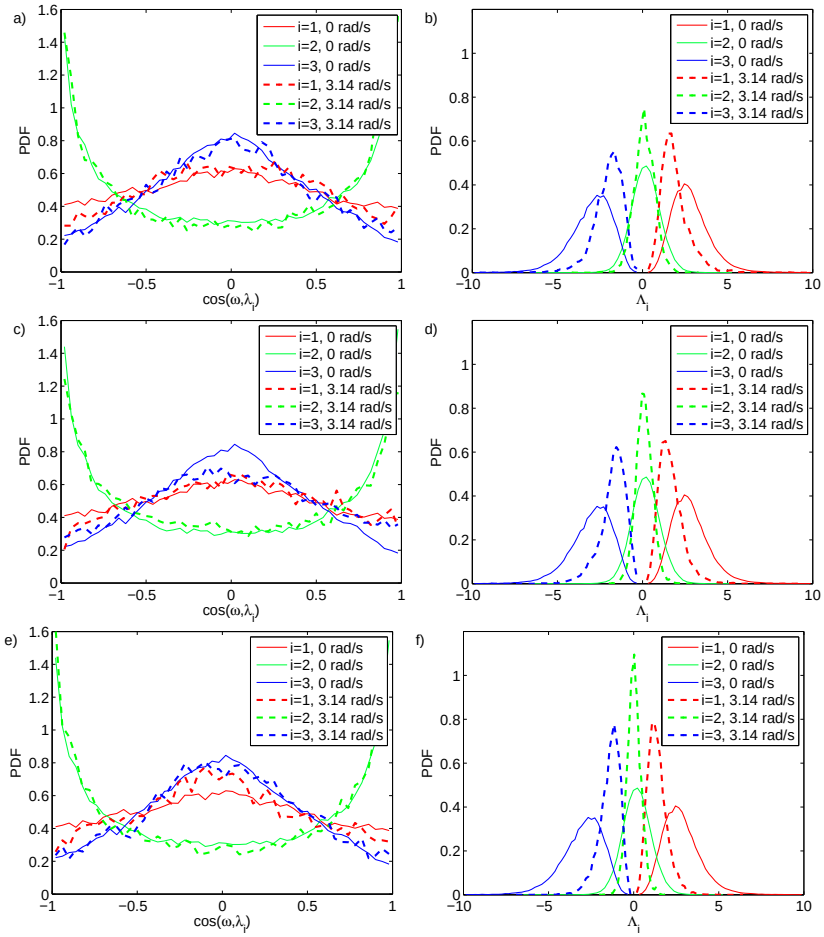

Figure 40: PDFs of the cosine of the angle between the vorticity vector and the strain eigenvectors, λ_i (left) and PDFs of the eigenvalues (right) from an experiment without rotation (solid) and an experiment at an angular velocity of 3.14 rad/s (dashed). The data represent the flow 20mm (top), 27 mm (middle) and 35 mm from the grid.

	0 rad/s		3.14 rad/s	
	all	top	middle	bottom
$< \Lambda_1 >$	2.66	1.87	1.72	1.38
$< \Lambda_2 >$	0.18	0.12	0.11	0.02
$< \Lambda_3 >$	-2.83	-1.99	-1.83	-1.41
$< \omega^2 \Lambda_1 cos^2(\omega, \lambda_1) >$	23.05	7.23	6.26	3.11
$< \omega^2 \Lambda_2 cos^2(\omega, \lambda_2) >$	2.77	1.58	1.30	0.53
$< \omega^2 \Lambda_3 cos^2(\omega, \lambda_3) >$	-16.81	-5.92	-6.43	-2.83
$< \omega^2 \Lambda_1^2 cos^2(\omega, \lambda_1) >$	67.34	16.77	15.31	5.04
$< \omega^2 \Lambda_2^2 cos^2(\omega, \lambda_2) >$	10.92	4.60	2.73	1.38
$< \omega^2 \Lambda_3^2 cos^2(\omega, \lambda_3) >$	51.25	14.13	14.73	4.89

Table 4: Contribution of the terms associated with Λ_i to the mean enstrophy production, $< \omega_i \omega_j s_{ij} >$, and the magnitude of the vortex stretching vector, W^2, for a non-rotating experiment and three different heights at an angular velocity of 3.14 rad/s.

for the rotating experiment look rather noisy since they were calculated from a subset of the data, whereas for the non-rotating case the full data-set is used. Nevertheless the PDFs fall on top of each other, which shows that the flow in the rotating experiment is still 3D-turbulent in the proximity of the energy source. The alignments between ω and λ_i change from the 3D-turbulent to the quasi-2D case with distance from the grid, y. In the data from the mid-section of the small observation volume the alignment between ω and λ_3 has increased while the alignments between vorticity and the first two eigenvectors remain approximately the same. With further distance from the grid the alignment between ω and λ_3 decreases again and also the alignment between ω and λ_1 is reduced. This is visible in the PDFs for $cos(\omega, \lambda_1)$ and $cos(\omega, \lambda_3)$, which fall on top of each other as the probability of events has increased at the origin, Figure 40 (e). The PDF of $cos(\omega, \lambda_2)$ on the other hand is slightly more skewed towards plus/minus one.

The PDFs of Λ_i show that similar to the 3D-turbulent case $\Lambda_1 > 0$, Λ_2 features both positive and negative values and $\Lambda_3 < 0$ in the rotating experiment. However, it becomes immediately apparent that the magnitude of the Eigenvalues is smaller compared to the experiment without rotation. More significantly the positive skewness of Λ_2 ($< \Lambda_2 > > 0$), which is a genuine feature of 3D turbulence becomes suppressed in the rotating experiment, Figure 40 (f). Both the decrease in magnitude of the Eigenvalues and positive skewness of the second Eigenvalue grow stronger with distance from the energy source.

The analysis of the alignment between vorticity and the eigenframe yields that the flow in the proximity of the grid is similar for the two types of experiments. Although the influence of rotation is already visible in the reduced magnitudes of the Eigenvalues. With distance from the energy source there is first a region where vortex compression occurs to a larger degree and afterwards

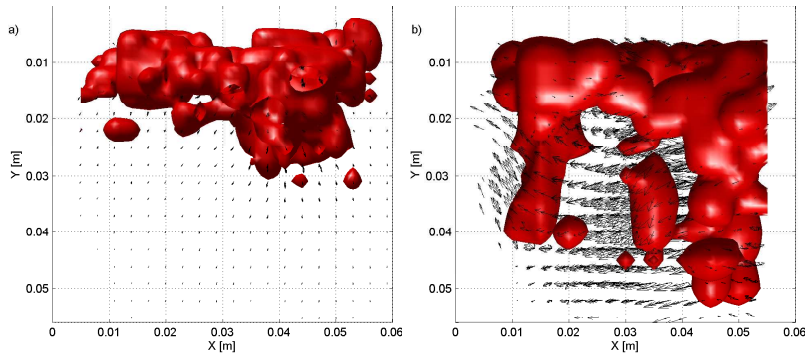

Figure 41: Enstrophy iso-surfaces ($\omega^2 = 8\ s^{-2}$) with superimposed velocity vectors for the turbulent/non-turbulent interface in an experiment without rotation at $t = 0.6s$ (a) and in the 3D/quasi-2D transition-zone in an experiment at a rotational velocity of 3.14 rad/s (b).

a region where both vortex stretching and compression are attenuated. This suggests that after a transition zone a quasi-2D regime is formed. This is in agreement with the PDF of Λ_2 losing its 3D-turbulent characteristic, i.e. its positive skewness. The conditionally averaged magnitudes of the Eigenvalues, Λ_i, the enstrophy production, $\omega_i\omega_j s_{ij} = \omega^2\Lambda_i cos^2(\omega, \lambda_i)$ and the vortex stretching vector, $W^2 = \omega^2{\Lambda_i}^2 cos^2(\omega, \lambda_i)$, are summarized in Table 4 for the data from the non-rotating experiment and the three different planes from the rotating experiment. The numbers clarify that enstrophy production is significantly lower in the 3D-region of the rotating flow than in the non-rotating experiment and decreases further in the quasi-2D regime. The positive skewness of the Λ_2-PDF on the other hand is still present in the 3D-region but has nearly vanished in the quasi-2D regime. The magnitude of the vortex stretching vector is also strongly reduced compared to the non-rotating experiment even more so in the quasi-2D region. Also the magnitude of the first and third component of the vector, ${W_1}^2$ and ${W_3}^2$, become almost the same, which suggests that vortex stretching and compression occur equally often in the quasi-2D flow.

3.2.4 Comparison Between the 3D/Quasi-2D Transition and the Turbulent/Non-Turbulent Interface

In the last subsections the development of the large and small scale quantities with distance from the the grid was illustrated. Next, the actual transition zone, which separates the 3D turbulent region from the quasi-2D regime will be compared to the turbulent/non-turbulent interface, which separates 3D turbulent from adjacent calm fluid in the experiment without rotation. In the first part of the analysis the 3D/quasi-2D transition zone has reached a statistically steady state, whereas the turbulent/non-turbulent interface only exists when the flow is still evolving. The second part of the analysis deals with a comparison of the temporal development of the transition region on the one hand and

the interface on the other.

Enstrophy iso-surfaces for $\omega^2 = 8\ s^{-2}$ with superimposed velocity vectors are presented in Figure 41 (a) for an experiment without rotation and at a rotational velocity of 3.14 rad/s in Figure 41 (b). For the experiment without rotation the flow is presented at $t = 0.6$ s with $t_0 = 0$ s being the onset of the grid movement. At this time the turbulent region fills approximately the upper third of the large observation volume. In the snapshot of the rotating experiment enstrophy is also confined to approximately the upper third of the large observation volume except for two fingers of high enstrophy, which reach into the lower part of the domain. A comparison with Figure 46 (a) where iso-surfaces of the vorticity component in direction of the rotational axis are displayed for the same experiment at the same time reveals that these two fingers of high enstrophy correspond to the centers of two vortex columns. Next, the conditional average of the enstrophy is calculated over horizontal slices but not over time, i.e. $< q(y,t) >=< q(x,y,z,t) >_{x,z}$. The corresponding curves for the two snapshots of Figure 41 are displayed in Figure 42 (a). For the experiment without rotation the enstrophy level is approximately 40 s^{-2} in the proximity of the grid and then declines rapidly with increasing y. Comparison with the enstrophy iso-surface and velocity vector field in Figure 41 (a) indicates that this drop in the enstrophy magnitude corresponds to the turbulent/non-turbulent interface, which is located on average 20 mm away from the grid at $t = 0.6\ s$. The spatial decay in the enstophy curve is less sharp in comparison to DNS data where a clear cut over the interface has been observed by Holzner et al. (2007). The sharp interface is smeared out by the simple average in the horizontal planes and we find a more distinct cut in the enstrophy curve when we condition the average on the turbulent/non-turbulent interface instead. However, for comparison with the data of the rotating case we constrain the analysis to the horizontal average and although this blurs the effects the corresponding curve from the rotating experiment is very different. Not only is the enstrophy lower in the proximity of the grid its magnitude becomes also higher with further distance from the energy source. This is an indicator that there is no sharp interface between the 3D-turbulence and the quasi-2D flow, which evolves under the influence of rotation. The lower enstrophy level close to the grid suggests that while the flow appears to be completely three dimensional it is already influenced by the aligning effect of the Coriolis force. The higher enstrophy level in the quasi-2D region compared to the calm fluid underneath the turbulent/non-turbulent interface was to be expected due to the ω_y-component, which is concentrated in the vortex columns.

For a closer examination the conditionally averaged curves for enstrophy and the squares of the three components of vorticity are depicted in Figure 43 (a) for the non-rotating and in (b) for the flow under the influence of rotation. Both flows have reached a statistically steady state, i.e. the turbulent/non-turbulent interface no longer exists. In the non-rotating experiment the three components of vorticity are all approximately equal with only ω_y being slightly lower. Interestingly all three vorticity components are also present in the quasi-2D part of the rotational flow. Therefore the square of the vorticity component in di-

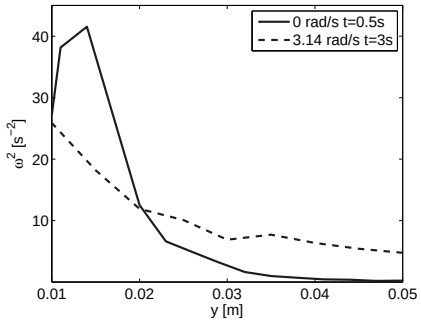

Figure 42: Enstrophy across the turbulent/non-turbulent interface (solid) and 3D/quasi-2D transition-zone (dashed)

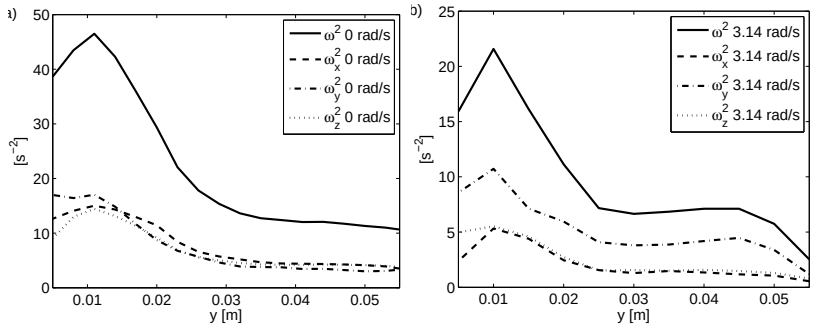

Figure 43: Enstrophy (solid), ω_x (dashed), ω_y (dot dashed) and ω_z (dotted) in the 3D-turbulent flow (a) and 3D/quasi-2D transition-zone at a rotational velocity of 3.14 rad/s (b).

rection of the rotational axis, ω_y, stays smaller than the enstrophy. However, ω_y is dominant over the horizontal components of vorticity, ω_x and ω_z. The comparison between the two types of experiments shows that the magnitude of enstrophy is considerably lower under the influence of rotation and also in the proximity of the energy source.

Now that the general qualitative behavior of mean enstrophy over the turbulent/non-turbulent interface and the transition zone from 3D to quasi-2D flow has been discussed, Figure 44 investigates its development over time. Figure 44 (a) displays the conditionally averaged enstrophy, $< \omega^2(y) >$, for an experiment without rotation, while the corresponding curves for an experiment with a rotational velocity of 0.79 rad/s are given in Figure 44 (b). The gray shading corresponds to increasing time, i.e., $0 < t < 2$ s for the non-rotating and $0 < t < 3$ s for the rotating case. The different time spans, which are presented for the two experiments already give a hint that the flow evolves slower under the influence of rotation. In Figure 44 (a) the mean enstrophy curves

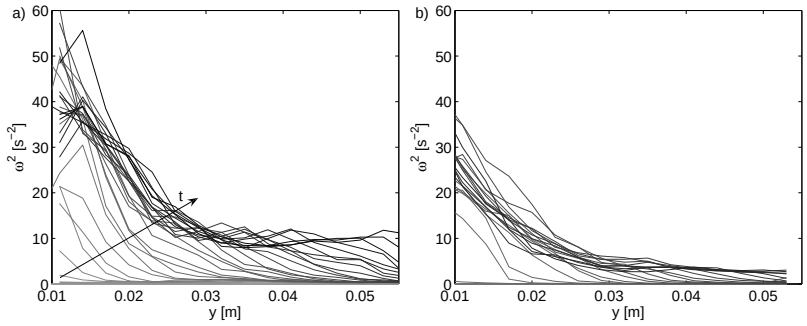

Figure 44: Temporal development of the conditionally averaged enstrophy magnitude for a non-rotating experiment (a) and at an angular velocity of 0.79 rad/s (b). The gray shading represents increasing time.

illustrate the propagation of the turbulent/non-turbulent interface through the large observation volume. The energy in the proximity of the grid and hence the mean enstrophy increases right after the start of the grid oscillation. For later times $< \omega^2(y) >$ gradually decreases with distance from the grid. However, the corresponding curves exhibit a kink, which corresponds to the position of the turbulent/non-turbulent interface (see Holzner et al. (2006)). In the rotating experiment the magnitude of enstrophy also increases after the onset of the grid oscillation. Also the propagation of the turbulent front through the observation volume is distinguishable in the enstrophy curves of the first time steps. However, these curves indicate some effects, which are not visible in the data from the experiment without rotation. The first effect is the jump in the mean enstrophy level, which occurs in the beginning of the experiment when the turbulent flow is spreading in the region of $0.01\ m < y < 0.02\ m$. Secondly, the magnitude of the conditionally averaged enstrophy decreases again for later times. For further insight the $< \omega^2(y) >$-curves at the times $t = 0.25$ s (dotted), $t = 0.5$ s (dashed) and $t = 3$ s (solid) are selected from Figure 44 (a) and (b) and displayed in Figure 45 (a).

At $t = 0.25$ s the curves for the averaged enstrophy for both types of experiments fall on top of each other. This suggests that the effects caused by the Coriolis force need time to develop. At $t = 0.5$ s there are first small deviations between the curves of the two experiments without (black) and with (gray) rotation. The dotted lines represent the mean enstrophy level at $t = 3$ s, i.e., for the steady state case when both flows are fully developed. The mean enstrophy level is lower under the influence of rotation and decreases towards a finite value, which is reached at a position $y \approx 0.03$ m. The curve calculated from the non-rotating data on the other hand exhibits a continuous decay.

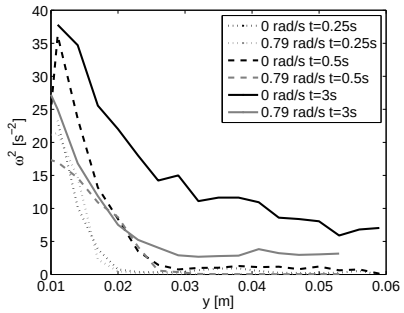

Figure 45: Mean entrophy over distance from the grid for an experiment without rotation (black) and at a rotational velocity of 0.79 (gray) rad/s at times 0.25 s (dotted), 0.5 s (dashed) and 3s (solid).

3.2.5 Summary of the Flow Characteristics with Distance from the Grid

The evolution of the flow characteristics with distance from the oscillating grid has been investigated by means of 3D-PTV. Large scale alignments were measured in a large observation volume and spatially resolved measurements of the velocity gradient tensor were taken in a small observation volume in the center of the tank underneath the lowest position of the oscillating gird. The results show that the 3D-turbulent flow remains confined to a distance $y < y^*$ and becomes quasi-2D for larger distances from the grid. The corresponding Rossby number was estimated to be $Ro(y^*) \approx 0.3$.

System rotation influences the two velocity components in different ways. The horizontal velocity component increases slightly with distance from the grid while it decreases in the experiment without rotation. The vertical component of velocity on the other hand is strongly suppressed in the quasi-2D region of the flow. For the large scales the main focus was on the manifestation of the influence of rotation on geometrical statistics. Alignment between (i) the velocity and the axis of rotation, (ii) vorticity and the axis of rotation and (iii) the Lagrangian and Coriolis acceleration were found. We find that in the quasi-2D region the orientation of the velocity vector becomes primarily normal to the axis of rotation, vorticity is predominantly aligned with the axis of rotation and the acceleration of fluid particles is preferentially aligned with the Coriolis acceleration. The magnitude of the Coriolis acceleration increases with distance from the energy source and becomes dominant over the Lagrangian acceleration, which decreases with distance from the grid. In the 3D-region of the turbulent flow, under the influence of rotation, the PDFs for the alignments of these quantities are close to the PDFs of the experiment without rotation. However, also in the 3D-regime the first effects of rotation are visible in the PDFs demonstrating the regulative effect of the rotational forces.

Spatially resolved measurements of the small scale quantities were only obtained in the small observation volume. The two horizontal components of

vorticity are still present in the quasi-2D part of the flow but they are strongly reduced. The vertical vorticity is dominant and its magnitude depends on the angular velocity. Both enstrophy and strain are considerably lower in the quasi-2D region of the flow but still satisfy the relation $< \omega^2 >= 2 < s^2 >$. Without rotation the magnitude of both quantities changes only slightly over the distance of the small observation volume, while there is a significant decrease in the magnitude of both enstrophy and strain under the influence of rotation. Also, vortex stretching occurs less often, while vortex compression increases in the quasi-2D region of the flow, as the distribution of $cos(\omega, W)$ suggests. Both effects grow stronger with distance from the grid. An examination of the PDFs of $cos(\omega, \lambda_i)$ and Λ_i reveal that enstrophy production and vortex stretching are reduced in the 3D-region in the proximity of the grid but still qualitatively similar to the experiment without rotation. In the quasi-2D region on the other hand both vortex stretching and enstrophy production are even further reduced and also differ qualitatively from the non-rotating case. More importantly, the positive skewness of the Λ_2-PDF, which is characteristic for 3D-turbulence, is only present in the proximity of the grid and almost disappears in the quasi-2D regime. The magnitude of the vortex stretching vector, W^2, implies that vortex stretching and compression occur equally often in the quasi-2D regime.

The analysis of the region between the 3D and quasi-2D flow confirms that the transition from one flow state to the other is continuous and not abrupt as for the turbulent/non-turbulent interface, which occurs in the free turbulent diffusion without rotation. Some differences in the spreading behavior of the turbulent flow between the rotating and non-rotating experiment become apparent when the averaged enstrophy is plotted over distance from the grid and time. Two main effects can be accounted for: (i) a jump in the magnitude of the conditionally averaged enstrophy at early times, (ii) after the flow has spread out the magnitude of the conditionally averaged enstrophy starts to decrease again before it stays constant.

3.2.6 Characterization of the Quasi-2D Flow Regime

The PDFs of the geometrical alignments with distance from the grid do not converge to the values, which would be found if the flow was fully two dimensional. This suggests the presence of three-dimensional flow regions in the lower part of the observation volume and this is why we call this region quasi-2D. More can be learned by further examination of the vortex columns as well as the regions between the them. In the following, results of this investigation are shown exemplarily for an experiment under the influence of a rotational velocity of 3.14 rad/s, but qualitatively similar results are obtained at lower rotation rates and some of them will be shown further below. A typical flow pattern can be seen in Figure 46 where two vortex columns are visualized at a given time.

In Figure 46 (a) iso-surfaces of ω_y at the levels of $+0.4s^{-1}$ (red) and $-0.9s^{-1}$ (blue) are depicted together with the superimposed three-dimensional velocity vector field. The ω_y iso-surfaces allow for a clear visualization of the two columnar vortices. Contrary to the experiments at the lower rotational velocities in

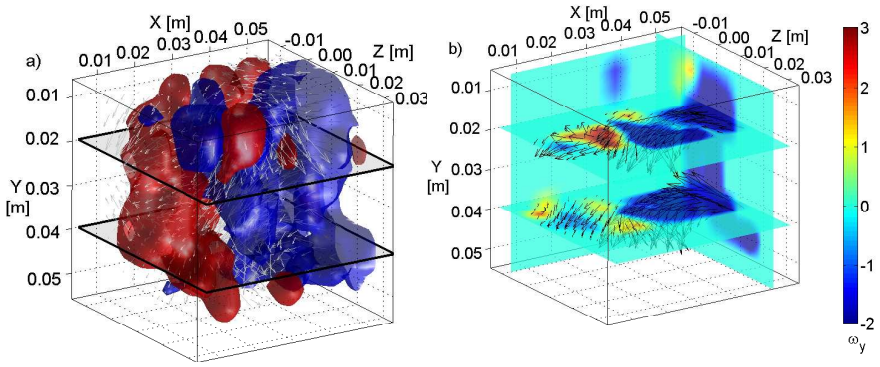

Figure 46: Positive (red) and negative (blue) ω_y iso-surfaces with superimposed velocity vector field (a) and slices of ω_y contours with superimposed Eulerian velocity vector field (b) from an experiment at a rotational velocity of 3.14 rad/s.

which usually only one columnar vortex is visible at a time the flow topology featuring two vortex columns inside the large observation volume is commonly observed in the experiments at the rotational velocity of 3.14 rad/s. The reason is that the number of vortex columns increases and their size decreases with rotation speed. In the experiments at a rotational velocity of 3.14 rad/s the diameter of the vortex column as it is estimated from the Γ_2-criterion is of the order of 30mm and thus smaller than the width of the large observation volume. Also, the two objects seem to fill almost the whole volume, i.e. the 'intermediate' region, where ω_y is weak, is comparatively small in volume. Similar to the visualizations above, slices of ω_y-contours are presented in Figure 46 (b). The velocity vector field is superimposed in the horizontal planes (x-z). A cyclonic and an anticyclonic columnar vortex are visible as red and blue patches in the ω_y-contours and their rotating motion can be recognized in the velocity vector field. The location of the vortex cores agrees well with the velocity and vorticity data.

The centers of the vortex columns were detected using the method described in Section 2.7 and their motion was traced in time. Differentiating the trace produces the average horizontal velocity with which the vortex cores move inside the tank. For the anticyclonic vortex column this velocity was calculated to be 5.2 mm/s, compare Table 6. Nevertheless the vortex columns hardly leave the area of the observation volume during the duration of the experiment. Such persistency is in agreement with the experimental findings of, e.g., Ruppert-Felsot et al. (2005). From the visualization experiments using Pearlescence it can be observed that this behavior only applies for the vortex columns in the center of the tank while the columnar structures in the outer regions display more movement. An exemplary path, which the anticyclonic vortex core describes within the large observation volume during the recording time is depicted in Figure 47 (a). The time derivative of this path, i.e. the magnitude of the horizontal velocity of the vortex core as a function of time can be observed in Figure 47 (b). After detecting the vortex columns as described in 2.7 the flow

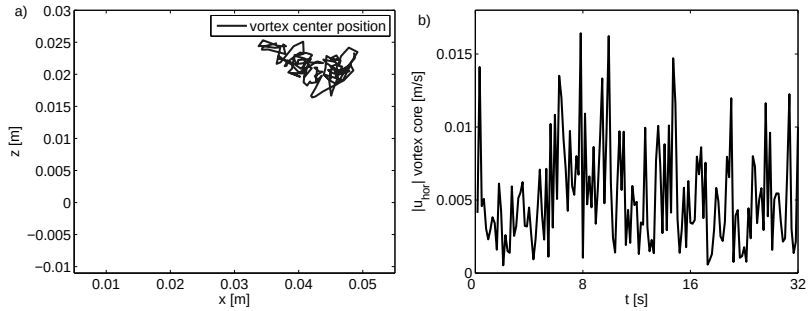

Figure 47: Path of the anticyclonic vortex column (left) and magnitude of the horizontal velocity with which the vortex column travels (right) for an experiment at a rotational velocity of 3.14 rad/s.

field can be divided into regions for different values of the angular momentum Γ_1. According to our definition, regions where $|\Gamma_1|$ lies in the interval between 0.8 and 1 correspond to the center of cyclonic and anticyclonic vortices, respectively. In the experiment Γ_1 ranges from -0.9 to 0.6 and PDFs of the geometrical alignment with distance from the center of the vortex tubes have been calculated for sixteen Γ_1-regions with 0.1 increments. The gray shading of the PDF curves represents increasing Γ_1. The curves corresponding to the PDFs at Γ_1= -0.9 (black), 0 (gray) and 0.6 (light gray) are plotted thicker than the curves at the steps in between these values.

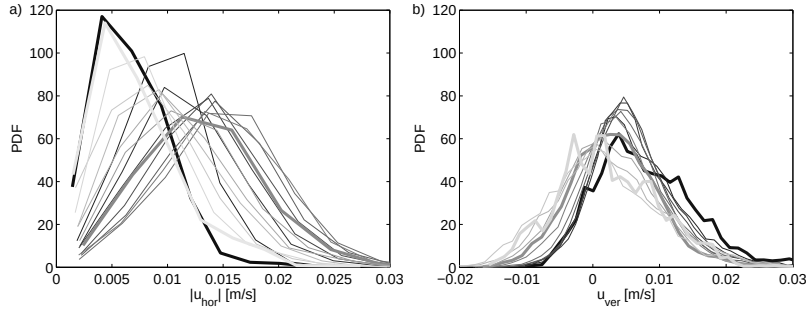

Figure 48: PDF of the magnitude of the horizontal (a) and the vertical velocity (b). The gray shading represents increasing Γ_1, where Γ_1 depends on the radial distance from the core of a vortex column.

The PDFs of the magnitude of the horizontal velocity and vertical velocity are displayed in Figure 48 (a) and (b), respectively. The magnitude of the horizontal velocity is noticeably smaller in the center of the vortex columns (i.e., for $|\Gamma_1| > 0.8$) than in the outer regions of the vortex tubes. The magnitude of the vertical component of velocity is significantly smaller than the horizontal component and also approximately four times smaller than without rotation. In contrast to the horizontal velocity the highest vertical velocities occur in the centers of the columnar vortices. The vertical velocity is negative in the center

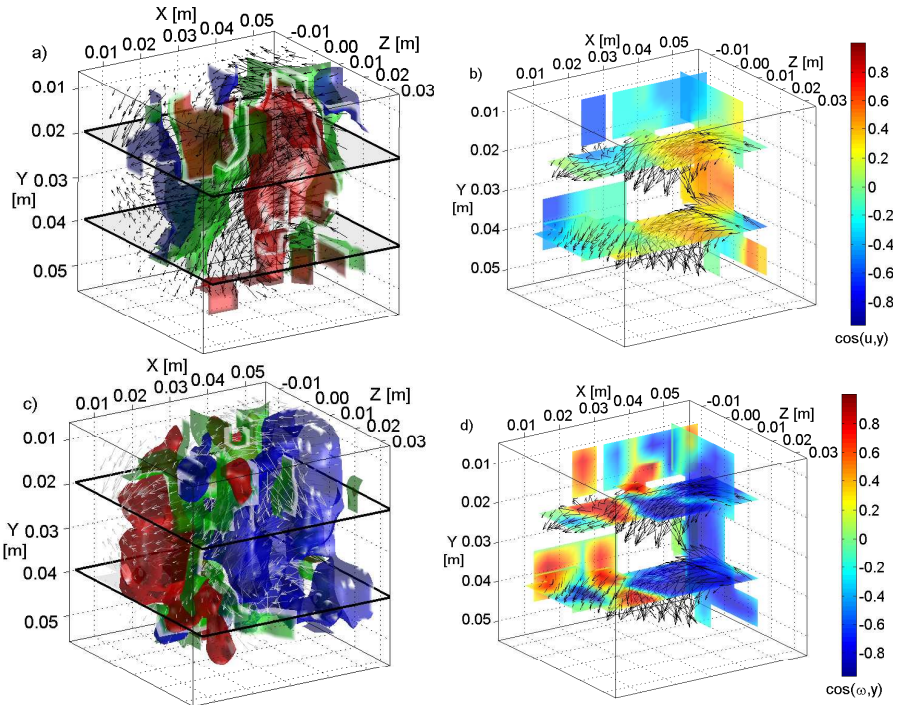

Figure 49: Positive (red), zero (green) and negative (blue) iso-surfaces of $cos(u, y)$ (a) and $cos(\omega, y)$ (c) with superimposed velocity vector field and slices of $cos(u, y)$ (b) and $cos(\omega, y)$ (d) contours with superimposed Eulerian velocity vector field from a run with a rotational velocity of 3.14 rad/s.

of cyclonic vortex columns (towards the grid) and positive in the center of anti-cyclones (away from the grid). This demonstrates the fluid transport inside the columnar structures due to the Ekman pumping effect.

In the results discussed earlier the cosine of the angle between the vectors of velocity and the axis of rotation and the cosine of the angle between the vectors of vorticity and the axis of rotation have proven to be appropriate to describe the flow patterns, which form the vortex columns. Figure 49 visualizes the cosine of the angle between the vectors of velocity and the axis of rotation as well as the cosine of the angle between the vectors of vorticity and the axis of rotation for the flow. On the left hand side of Figure 49 iso-surfaces of $\cos(u, y)$ (a) and $\cos(\omega, y)$ (c) with superimposed velocity vector fields are visible. The iso-surface levels for both cosine functions are +0.8 (red), 0 (green) and -0.6 (blue). On the right hand side contour plot slices of $\cos(u, y)$ (b) and $\cos(\omega, y)$ (d) are shown. The velocity vector field is again superimposed in the horizontal planes (x-z). Comparison with Figure 46 allows to assign regions where the values of the cosines go towards one, minus one or zero to the different structures in the flow field, i.e., to link the alignments, which occur in the flow due to the influence of rotation to the pattern of the columnar structures. The cosine of the angle

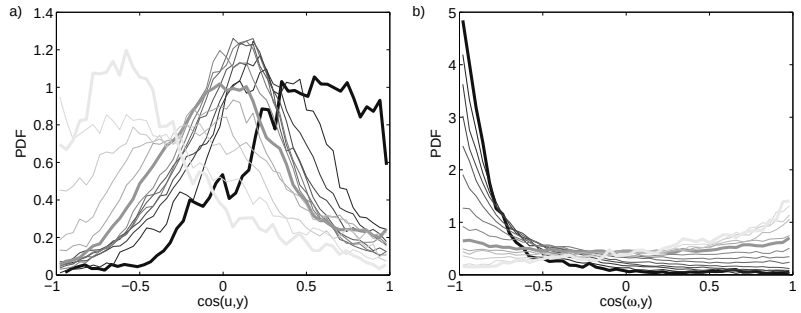

Figure 50: PDF of the cosine of the angle between the vectors of velocity (a) and vorticity (b) and the axis of rotation. The gray shading represents increasing Γ_1, where Γ_1 depends on the radial distance from the core of a vortex column.

between the vectors of velocity and the axis of rotation is positive in the core region of the anticyclonic and negative in the core of the cyclonic vortex column. This is caused by fluid being transported upwards inside the cyclonic vortex columns and downwards inside the anticyclonic vortex columns. in between the two vortex columns there is a region in which $cos(u, y)$ is zero. This is a results of the horizontal orientation of the velocity vector in the outer regions of the vortex columns. The visualization of the cosine of the angle between the vectors of vorticity and axis of rotation shows again the position of the cyclonic and anticyclonic vortex columns. Regions of positive and negative cosine are inverse for $\cos(u, y)$ and $\cos(\omega, y)$ since the direction of the fluid transport inside the columns is in the opposite direction to the vorticity vector. The regions where $\cos(\omega, y)$ is zero are located in between the vortex columns.

The PDFs of $cos(u, y)$ are presented in Figure 50 (a) for $-0.9 < \Gamma_1 < 0.4$. Three different flow regions are distinguishable in the PDF curves, namely the outer region of the cyclonic vortex columns ($\Gamma_1 > 0.2$) where the PDFs are skewed towards minus one, a region, which corresponds to the area between the vortex columns ($-0.2 < \Gamma_1 < 0.2$) where the PDFs are almost centered around zero and a region, which represents the flow influenced by the anticyclonic vortex column ($\Gamma_1 < -0.8$) where the PDFs are skewed towards one. In agreement with earlier findings by Hopfinger et al. (1982) this also confirms that fluid is transported upwards in cyclonic and downwards in anticyclonic columnar vortices. In the outer region of the vortex column the velocity is orientated nearly horizontally, i.e. the highest probabilities are at an angle normal to the rotation axis. The imprints of the cyclonic and anticyclonic vortices are also clearly distinguishable in the PDFs of Figure 50 (b). Here the cosine of the angle between the vectors of vorticity and the axis of rotation is clearly skewed towards one for the region of the cyclonic and towards minus one for the region of the anticyclonic columnar vortices. Interestingly, distributions from the region, which corresponds to $\Gamma_1 \approx 0$ do not feature any preferential alignments, where the curve being very flat. This suggests that the flow in between the vortex columns is three dimensional. The change between the regions seems to be not abrupt but continuous. The same picture is drawn by the PDFs of the

curvature, which are presented in Figure 51 (b). The curvature is larger within the vortex columns than in the region between the vortex columns and its mean value agrees well with the reciprocal of the vortex column radius.

The alignment between Lagrangian and Coriolis acceleration, which can be seen in Figure 51 (a) where PDFs of the cosine of the two quantities are depicted decreases with increasing Γ_1. Therefore this alignment, while being present in the whole 2D-flow domain, seems to be strongest in the anticyclonic and weakest in the cyclonic vortex columns.

From the different alignments we define three qualitatively different regions: (i) $|\Gamma_1| > 0.8$ for the core region of the cyclonic and anticyclonic vortex columns where fluid is transported upwards and downwards, respectively, (ii) $0.2 < |\Gamma_1| < 0.8$ for the outer region of the vortex columns where the velocity vector is mainly in the horizontal plane and (iii) $|\Gamma_1| < 0.2$ for the region in between the vortex columns, where the alignments remain random distributed.

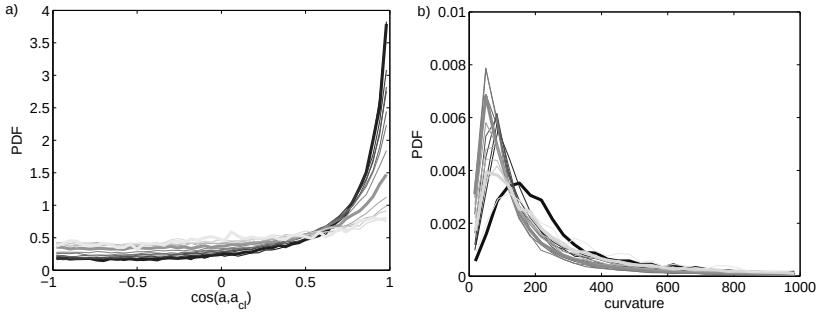

Figure 51: PDF of the cosine of the angle between the vectors of Lagrangian and Coriolis acceleration (a) and curvature (b). The gray shading represents increasing Γ_1, where Γ_1 depends on the radial distance from the core of a vortex column.

So far the large scale alignments, which form the flow patterns in the quasi-2D regime have been illustrated. Next the influence of the Coriolis forces on further small scale quantities will be presented. The first two quantities to be analyzed are enstrophy and strain.

As before, Figure 52 (left) shows iso-surfaces of enstrophy (a) and strain (c) with the three-dimensional velocity vector field superimposed, while Figure 52 (right) presents contour slices with superimposed velocity fields for these two quantities. Iso-surfaces are plotted at a level of $10s^{-2}$ for enstrophy and $8s^{-2}$ for strain, respectively. Both enstrophy and strain are high in the upper part of the observation volume which corresponds to the 3D-turbulent region in the proximity of the grid. In the quasi-2D region of the flow however, high levels of enstrophy seem to be confined to the regions of the vortex tube cores. Regions of high strain on the other hand are predominantly located in between the vortex columns. However, the PDFs of enstrophy and strain, which are given for regions of $-0.9 < \Gamma_1 < 0.4$ in Figure 53 (a) and (b) demonstrate that the differences between the Γ_1 regions are marginal. These results indicate that

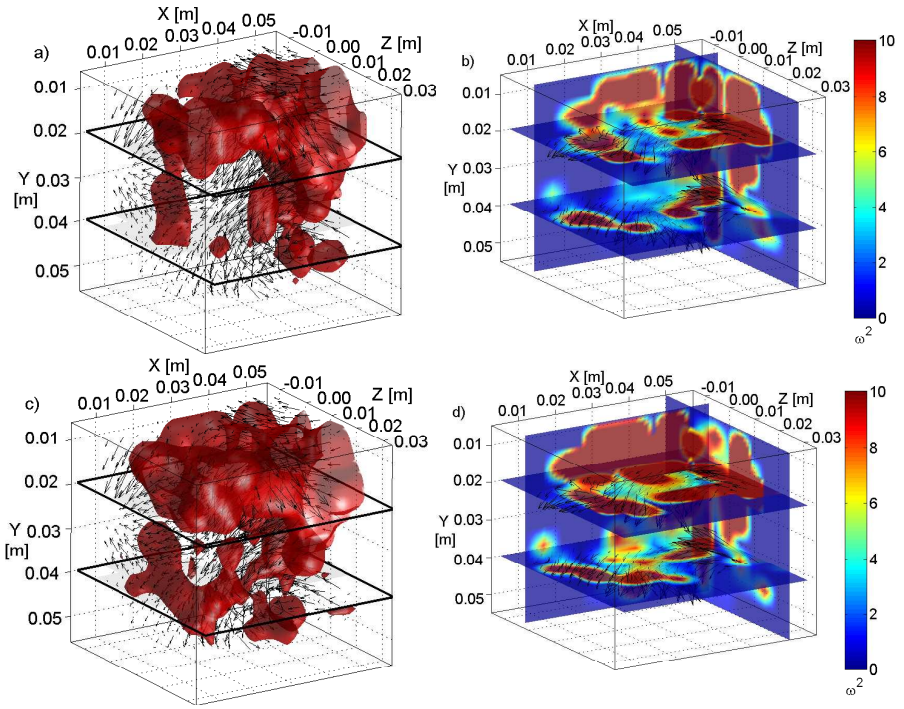

Figure 52: Enstrophy (a) and strain (c) iso-surfaces with superimposed velocity vector field and slices of enstrophy (b) and strain (d) contours with superimposed Eulerian velocity vector field from a run with a rotational velocity of 3.14 rad/s.

the flow inside the vortex columns is less turbulent. Although the flow in the center of the vortex columns is primarily vertical it generates enstrophy, i.e. experiences a rotational movement on top of the vertical flow. The high strain level in between the vortex columns indicates a three-dimensional, turbulent flow. Similar to the approach in Section 3.2.3 the effects of vortex stretching and compression are analyzed for the different regions of the quasi-2D flow. Firstly, the alignment of vorticity with the vortex stretching vector is presented in Figure 54. The PDFs show the cosine of the angle between the vectors of the two quantities and the gray shading corresponds to the position between the cores of the anticyclonic and cyclonic vortices, namely $-0.9 < \Gamma_1 < 0.4$. The curves are less skewed towards one and exhibit more data around minus one in comparison to the PDFs from the experiment without rotation, which are displayed in Figure 39 (a). This demonstrates again that vortex stretching occurs less and vortex compression more often in the quasi-2D region of the flow. The differences between the Γ_1-regions are marginal. To gain further knowledge of the vortex stretching and compression, which occur inside and in between the vortex columns the cosine of the angle between the vorticity vector and the strain eigenvectors is examined for the regions of $\Gamma_1 = -0.8$ (Figure 55 a), $\Gamma_1 = -0.7$ (Figure 55 c) and $\Gamma_1 = 0$ (Figure 55 e), i.e. for the region of the vortex column

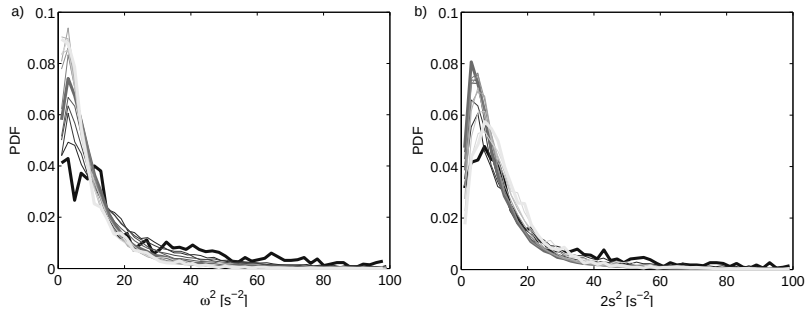

Figure 53: PDF of enstrophy (a) and strain by a factor of two (b). The gray shading represents increasing Γ_1, where Γ_1 depends on the radial distance from the core of a vortex column.

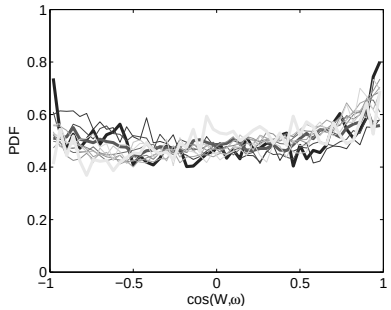

Figure 54: PDF of the cosine of the angle between the vorticity and the vortex stretching vectors. The gray shading represents increasing Γ_1, where Γ_1 depends on the radial distance from the core of a vortex column.

core, the outer vortex column and in between the vortex columns. Again the PDFs for the experiment without rotation (solid) are displayed for comparison and the PDFs for the experiment under the influence of a rotational velocity of 3.14 rad/s (dotted). In the core region of the vortex columns $cos(\omega, \lambda_i)$ behaves similar to the results found for the average behavior of the whole quasi-2D region of the flow in section 3.2.3. Namely, the dominance of the intermediate mode $cos(\omega, \lambda_2)$ is increased while both vortex stretching, $cos(\omega, \lambda_1)$, and compression, $cos(\omega, \lambda_3)$, occur less in comparison to the experiment without rotation. In the outer regions of the columnar vortices on the other hand vortex compression increases, while vortex stretching remains low. The effect is clearest in the PDFs for the region of $\Gamma_1 = -0.7$ but the results are qualitatively the same for the whole outer region of the vortex columns, $0.2 < |\Gamma_1| < 0.8$.

The PDFs for the region in between the vortex columns, $|\Gamma_1| < 0.2$, feature a shape which is again close to the PDFs of the non-rotating experiment. This confirms that the flow remains three-dimensionally turbulent in between the vortex columns. However, vortex compression occurs slightly more often in the region between the columnar vortices compared to the flow in the experiment without rotation. Also, the magnitudes of the eigenvalues and the positive

skewness of Λ_2 are decreased in all three Γ_1-regions compared to the experiment without rotation. The lowest magnitudes are observed for the outer region of the vortex columns. The conditionally averaged magnitudes of the Eigenvalues, Λ_i,

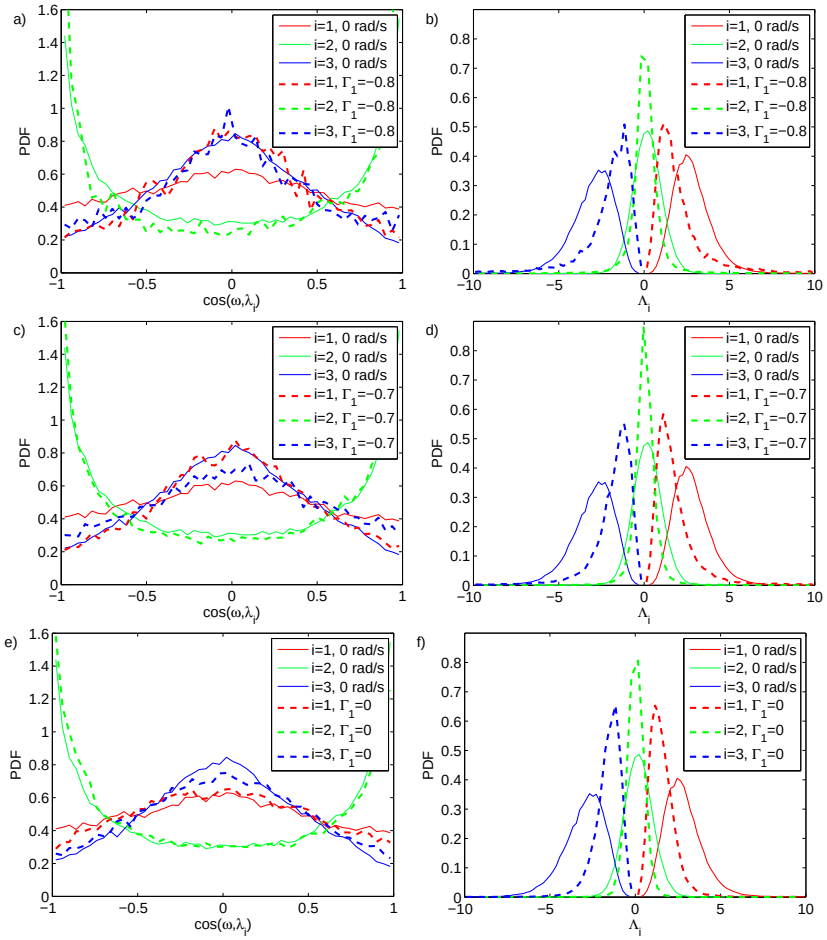

Figure 55: PDF of the cosine of the angle between the vorticity vector and the strain eigenvectors, λ_i, (left) and PDF of the eigenvalues (right). The data represents the flow at regions of Γ_1= -0.8, -0.7 and 0.

the enstrophy production, $\omega_i\omega_j s_{ij} = \omega^2\Lambda_i cos^2(\omega, \lambda_i)$ and the vortex stretching vector, $W^2 = \omega^2{\Lambda_i}^2 cos^2(\omega, \lambda_i)$, are summarized in Table 5 for the data from the non-rotating experiment and the three different Γ_1-regions from the rotating experiment. The positive skewness of the Λ_2-PDFs, which is characteristic for 3D-turbulence, has nearly vanished not only in the region occupied by the vortex columns but also in between. However, both in the core and the outer region of the columnar structures vortex compression and hence enstrophy destruction (λ_3-direction) are slightly higher than enstrophy production in λ_1-direction. In

	3.14 rad/s bottom		3.14 rad/s	
		$\Gamma_1 = -0.8$	$\Gamma_1 = -0.7$	$\Gamma_1 = 0$
$<\Lambda_1>$	1.38	1.72	1.63	1.55
$<\Lambda_2>$	0.02	0.07	0.04	0.03
$<\Lambda_3>$	-1.41	-1.79	-1.66	-1.58
$<\omega^2\Lambda_1 cos^2(\omega,\lambda_1)>$	3.11	6.92	6.46	3.88
$<\omega^2\Lambda_2 cos^2(\omega,\lambda_2)>$	0.53	1.03	0.17	0.27
$<\omega^2\Lambda_3 cos^2(\omega,\lambda_3)>$	-2.83	-7.50	-6.94	-3.18
$<\omega^2\Lambda_1^2 cos^2(\omega,\lambda_1)>$	5.04	17.13	15.45	8.15
$<\omega^2\Lambda_2^2 cos^2(\omega,\lambda_2)>$	1.38	4.53	3.62	1.58
$<\omega^2\Lambda_3^2 cos^2(\omega,\lambda_3)>$	4.89	19.25	16.59	6.77

Table 5: Contribution of the terms associated with Λ_i to the mean enstrophy production, $<\omega_i\omega_j s_{ij}>$, and the magnitude of the vortex stretching vector, W^2, for a non-rotating experiment and three different Γ_1-positions at an angular velocity of 3.14 rad/s.

the outer region of the columns the sum of the three components of the enstrophy production becomes even negative. On the other hand the ratio of enstrophy production in λ_1 and λ_3-direction is again closer to the one in the 3D-turbulent flow for the region in between the vortex columns.

3.2.7 Summary of the Characterization of the Quasi-2D Flow Regime

A closer examination of the quasi-2D regime has demonstrated that this region can be divided into three parts: (i) the core of the vortex columns, (ii) the outer region of the vortex columns and (iii) the flow in between the columnar structures. The horizontal component of velocity grows with distance from the vortex core while the magnitude of the vertical velocity is largest in the center of the columnar vortices. The sign of the vertical component of velocity is opposite for the centers of cyclonic and anticyclonic vortices and confirms that fluid is transported upwards in cyclones and downwards in anticyclones. This fluid transport is also clearly represented in the alignment between the velocity vector and the axis of rotation as PDFs of $cos(u, y)$ are skewed towards one for the core region of anticyclonic vortices and minus one for cyclonic cores, respectively. For the outer regions of the vortex columns this quantity shows that the flow is basically aligned with the horizontal direction. The pattern of the cyclonic and anticyclonic vortex columns are also captured in the alignment between the vorticity and the axis of rotation as PDFs of $cos(\omega, y)$ are skewed towards one in the region of cyclones and minus one for anticyclones, respectively. Interestingly, the skewness decreases with distance from the vortex cores until the values of the cosine are randomly distributed over the whole range of the cosine for the region in between the columnar structures. This is an indicator that the flow remains three-dimensional in this region. A different behavior can be observed in the

alignment between the Coriolis and Lagrangian acceleration. Both accelerations are aligned with each other in the whole 2D-regime, i.e. the PDFs of $cos(a, a_{cl})$ are all skewed towards one. The highest alignment occurs in the center of the anticyclones from where it decreases until it reaches its lowest value in the region of the cyclonic vortex columns.

For the level of small scale quantities high levels of enstrophy seem to be confined to the regions of the vortex tube cores. Regions of high strain on the other hand are predominately located in between the vortex columns. However both quantities are significantly lower than in the non-rotating flow. The positive skewness of the Λ_2-PDFs, which is characteristic for 3D-turbulence, nearly vanishes not only in the region occupied by the vortex columns but also in between. However, both in the core and the outer region of the columnar structures vortex compression and hence enstrophy destruction (λ_3-direction) are slightly higher than enstrophy production in λ_1-direction. In the outer region of the columns the sum of the three components of the enstrophy production becomes even negative. On the other hand the ratio of enstrophy production in λ_1- and λ_3-directions is again closer to the one in the 3D-turbulent flow for the region in between the vortex columns.

3.2.8 Comparison of Different Rotational Velocities

The previous sections have illustrated some effects, which rotation can have on turbulent flows and also compared them to the flow topology of an experiment without rotation. This section analyses the dependency of these effects on the rotational velocity. Therefore PDFs of the large and small scale quantities, which were calculated previously for different distances from the grid, y, and different distances from the vortex column cores are now calculated from all data available in the small observation volume for experiments at different rotational velocities. In the following these PDFs are compared with each other.

Figure 56 (a) and (b) depicts PDFs of the magnitude of the horizontal and the vertical components of velocity respectively for rotational velocities from 0.79 rad/s to 3.14 rad/s. PDFs from an experiment without rotation are displayed for comparison. The curves are calculated from the whole data available in the small observation volume. The PDFs of the horizontal component of velocity tend to be shifted further towards large magnitudes with higher rotational velocities. The vertical velocity component remains unaffected for higher rotational velocities. This shows that system rotation influences the two velocity components in different ways. While an increase in the Coriolis force causes the magnitudes of the horizontal velocity component to increase, the vertical component of velocity is equally shifted to lower values for all rotational velocities. Only the lowest rotational velocity of 0.79 rad/s deviates slightly from the other rotational velocities. However, also for the lowest rotational velocity the vertical component of velocity is strongly reduced. The significance of the shift in the vertical velocity to lower values becomes apparent when comparing the PDFs to data without rotation. The PDFs derived for the two components of velocity from the experiment without rotation differ from the curves presented

rotational velocity [rad/s]	0.79	1.05	1.57	3.14
$\|u_{hor}\|$ [mm/s] core region	8.1	9.1	9.6	12.6
u_{ver} [mm/s] core region	9.5	7.9	6.0	5.8
$\|u_{hor}\|$ [mm/s] outer region	8.0	9.8	11.6	13.2
u_{ver} [mm/s] outer region	2.8	0.88	0.8	1.8
$\|u_{hor}\|$ [mm/s] in between region	8.5	9.8	9.2	9.9
u_{ver} [mm/s] in between region	-1.2	-0.13	-0.8	0.0
$\|u_{hor}\|$ [mm/s] vortex core	14.1	6.4	7.4	5.2

Table 6: Magnitude of the horizontal and vertical velocities for the core, the outer region and the region in between the columnar vortices at rotational velocities of 0.79 rad/s, 1.05 rad/s, 1.57 rad/s and 3.14 rad/s

in section 3.2.3 as the mean velocity field was not subtracted from the data in Figure 56. This was done to allow for a better comparison with the data from the experiments at low rotational velocities. Table 6 lists the horizontal

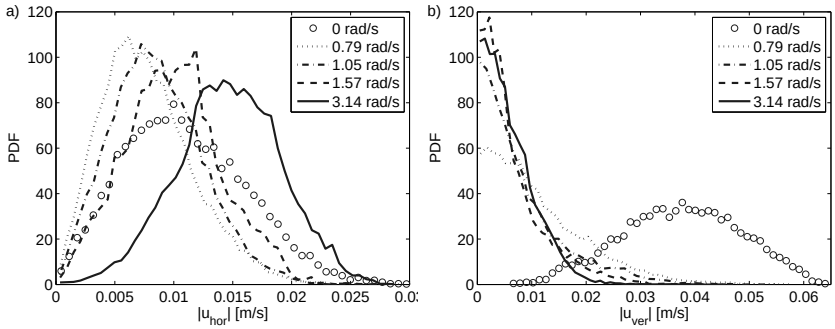

Figure 56: PDF of the horizontal (a) and vertical (b) component of the magnitude of velocity for rotational velocities of 0 rad/s (○), 0.79 rad/s (dotted), 1.05 rad/s (dot dashed), 1.57 rad/s (dashed) and 3.14 rad/s (solid).

and vertical velocities for the core and the outer region of the vortex columns as well as for the region in between the columns. The values are given for four different rotational velocities from 0.79 rad/s to 3.14 rad/s. The flow in the core of the vortex columns and in between the columns is relatively unaffected by a change in the rotational velocity. The horizontal velocity in the outer region of the columnar vortices on the other hand increases with the rotational velocity.

The influence of the rotational velocity on the magnitude of the acceleration is presented in Figure 57 (a). The magnitude of the acceleration is generally lower in the experiments under the influence of rotation than in the experiment without rotation. The influence of the rotation is such that it decreases the magnitude of the acceleration. This indicates that the columnar structures formed by the Coriolis force reduce the level of turbulence and thus the magnitude of

the accelerations, which occur in the flow. The importance of the Coriolis acceleration and its dependence on the rotational velocity can be determined from Figure 57 (b). The figure presents the alignment between the Lagrangian and Coriolis accelerations, $cos(a, a_{cl})$, for four different rotational velocities. The PDFs become more skewed towards one with increasing rotational velocity, indicating an increase in the alignment between the two accelerations. However, the curves for the rotational velocity of 3.14 rad/s is only slightly higher than for the second highest velocity of 1.57 rad/s. This suggests that the alignment grows asymptotically towards a finite value. The influence of the rotational

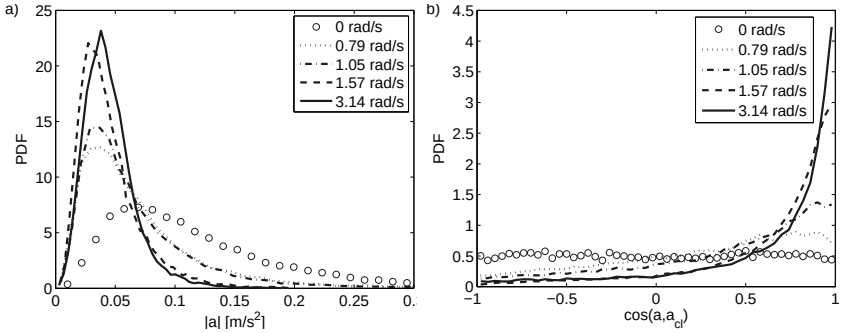

Figure 57: PDF of the magnitude of the Lagrangian acceleration (a) and the cosine of the angle between the vectors of Lagrangian and Coriolis acceleration (b) for rotational velocities of 0 rad/s (∘), 0.79 rad/s (dotted), 1.05 rad/s (dot dashed), 1.57 rad/s (dashed) and 3.14 rad/s (solid).

velocity on the alignments in the flow is even more distinct in the PDFs of the cosine of the angle between the vectors of velocity and the axis of rotation and in the PDFs of the cosine of the angle between the vectors of vorticity and the axis of rotation, respectively. The corresponding PDF curves are presented in Figures 58 (a) and (b), respectively. On the left hand side of the figure it becomes apparent how the primary alignment of the velocity vector with the horizontal direction becomes more pronounced with increasing rotational velocity. Therefore the PDF curves exhibit a maximum around zero. However, they remain slightly skewed towards one. This skewness of the PDFs is more pronounced at low rotational velocities and represents the vertical flow caused by the high solidity in the middle of the grid as well as the fluid transport inside the anticyclonic vortex columns. The cosine of the angle between the vectors of vorticity and axis of rotation is displayed in Figure 58 (b). The PDFs of this invariant become more skewed towards minus one with increasing rotational velocity. This reflects the dominance of the vertical component of vorticity and hence the columnar vortices. The PDF for the non-rotating experiment has a small maximum close to zero and is almost symmetric. This tendency of the vorticity to be slightly more aligned with the horizontal axis in the small observation volume is also caused by the grid forcing. The last quantity for which the influence of the rotational velocity shall be discussed is the cosine of the

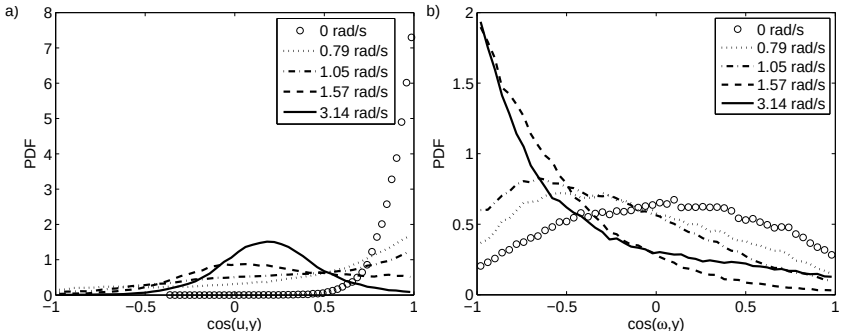

Figure 58: PDF of the cosine of the angle between the vectors of velocity and the axis of rotation (a) and vorticity and the axis of rotation (b) for rotational velocities of 0 rad/s (○), 0.79 rad/s (dotted), 1.05 rad/s (dot dashed), 1.57 rad/s (dashed) and 3.14 rad/s (solid).

angle between the vorticity vector and the vortex stretching vector. The corresponding PDF is skewed towards one for the non-rotating experiment, which results from the dominance of the vortex stretching mechanism in turbulent flows. With increasing rotational velocity the skewness towards one becomes less pronounced and the negative values of the PDF curves grow. Therefore not only vortex stretching is suppressed by the effect of rotation but also vortex compression takes place. Both effects grow stronger with increasing rotational velocity. However, only for the highest rotational velocity does the curve deviate significantly from the experiment without rotation.

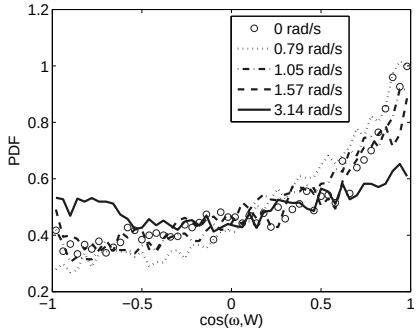

Figure 59: PDF of the cosine of the angle between the vectors of vorticity and the axis of rotation for rotational velocities of 0 rad/s (○), 0.79 rad/s (dotted), 1.05 rad/s (dot dashed), 1.57 rad/s (dashed) and 3.14 rad/s (solid).

Since the transition zone occurs at $Ro \approx 0.3$ its position with respect to the grid depends on the rotation rate, i.e., the distance between the grid and the transition region decreases with increasing rotational velocity. This can be seen qualitatively in Figure 27 where pictures from the visualization experiments using Pearlescence are presented at the rotational velocities 1.57 rad/s (a), 1.05

rad/s (b) and 0.79 rad/s (c). Quantitatively the effect of rotation on the transition from 3D to 2D turbulence can be examined when the evolutions of the mean flow quantities with distance from the grid are compared for different rotational velocities. The graphs in Figure 60 (a) display the conditional aver-

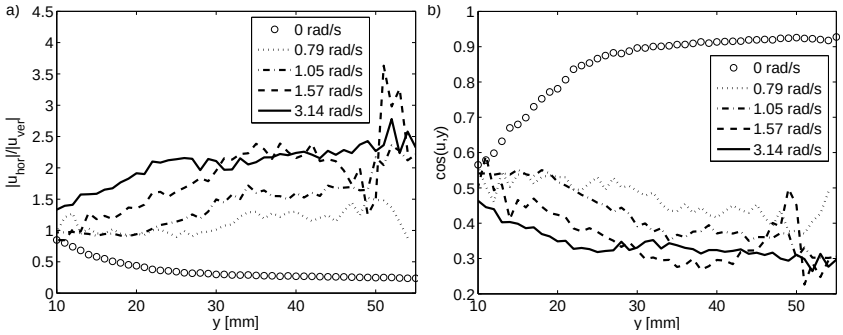

Figure 60: Conditional averages of the ratio of the horizontal over the vertical velocity (a) and of the cosine of the angle between the vectors of velocity and the axis of rotation (b) over distance from the grid for rotational velocities of 0 rad/s (○), 0.79 rad/s (dotted), 1.05 rad/s (dot dashed), 1.57 rad/s (dashed) and 3.14 rad/s (solid).

age of the ratio $< |u_{hor}|/|u_{ver}| >$ over the distance from the grid for the four different rotational velocities from 0.79 rad/s to 3.14 rad/s. The corresponding curve from an experiment without rotation has been added for comparison. The mean velocity field was not subtracted hence the vertical component of velocity becomes dominant in the experiment without rotation. For the experiments under the influence of rotation the horizontal velocity component was higher than the vertical velocity component. The ratio increases with distance from the grid and reaches a plateau. With increasing rotational velocities the level of the plateau increases and the position where the plateau is reached is located closer to the grid. However, there is only a slight difference between the levels of the plateaus at the highest rotational velocities. This general behavior can also be observed in Figure 60 (b) where the corresponding graphs are shown for $< cos(u, y) >$.

3.2.9 Summary of the Influence of the Rotational Velocity

The influence of system rotation on turbulence has been investigated for four different angular velocities and compared to the non-rotating case. The results show that system rotation influences the two velocity components in different ways. While an increase in Coriolis force causes the magnitudes of the horizontal velocity component to increase, the vertical component of velocity is equally suppressed for different rotational velocities. The magnitude of the Lagrangian acceleration on the other hand decreases with increasing angular velocity. The large scale alignments in the flow increase with the rotational velocity, namely

the primary alignment of the velocity vector with the horizontal direction, of the vorticity vector with the axis of system rotation and between the Lagrangian and Coriolis accelerations become more distinct. Further results on the level of small scales are a decrease in vortex stretching and an increase in vortex compression with increasing angular velocity.

The conditionally averaged curves of the ratio of the horizontal over the vertical velocity component as well as of the cosine of the angle between the vectors of velocity and the axis of rotation seem to reach a plateau with distance from the grid. This implies that the flow pattern becomes uniform after a certain distance from the grid, namely in the quasi-2D regime. With increasing rotational velocity the levels of these plateaus increase, i.e. the alignments grow stronger and the positions where the plateaus are reached are located closer to the grid. Interestingly, there is only a slight difference between the levels of the plateaus at the two highest angular velocities, which allows for the assumption that the effects, that rotation has on turbulence have an upper limit.

4 Conclusions

In this thesis, we add to the understanding of some specific, but fundamentally and practically very important aspects of turbulence. Namely, shear-free turbulence under the influence of confinement and rotation has been analyzed experimentally. The measurements have been carried out in a water tank placed on a rotating table and the flow is mechanically forced from the top by an oscillating grid. The confinement was realized in the experiment by using a thin-walled transparent tube. The tube was placed in the center of the tank, so that the growth of the turbulent integral length scales of the flow inside the tube was confined by its diameter. The influence of the confinement was systematically investigated with tube diameters ranging from 10 mm to 60 mm. After that, whole setup was placed on a rotating table to analyze the influence of rotation on the turbulent flow. The table has a diameter of 1m and was used at rotational velocities ranging from 0.29rad/s to 3.14 rad/s. The measurement techniques, which have been employed to study the flow are visualization experiments using Pearlescence and quantitative measurements using Particle Image Velocimetry and three-dimensional Particle Tracking Velocimetry. The first two measurement techniques (Pearlescence and PIV) were carried out with a field of view, which covers the whole midsection of the tank. They are therefore adequate to investigate the global behavior of the flow. The size of the observable volume, which was feasible in 3D-Particle Tracking Velocimetry is smaller and therefore used to zoom into special regions of the flow to investigate local characteristics and, in particular, quantities associated with the gradients of the velocity field. Measurements were conducted with two different volume sizes, namely a large observation volume allowing to capture the large scale motions of the flow and a small observation volume, in which the spatial resolution was sufficient to assess nine components of the velocity gradient tensor. One of the main achievements of this work is the simultaneous measurement of the large and small observation volumes using two synchronized Particle Tracking Velocimetry systems and two types of seeding particles, whose emitted and scattered light can be separated with filters. This allows for a direct coupling of the large- and small scale information.

The spreading of turbulence in time has been investigated experimentally for three different cases, i.e. (i) free turbulent diffusion, (ii) spreading of turbulence under the influence of confinement and (iii) spreading of turbulence under the influence of rotation. One motivation for this part was the validation of the Lie-group (symmetry) predictions of Oberlack and Günther (2003).

- Oberlack and Günther (2003) derived (i) a diffusion like solution, in which turbulence diffuses freely into the adjacent calm fluid. Our measurements confirm this solution and we observe that the turbulent/non-turbulent interface propagates according to a power law, $H \propto t^n$, where n is estimated to be $n = 0.6 \pm 0.1$ in agreement with earlier findings by Dickinson and Long (1982) and Holzner et al. (2006).

- For case (ii) when there is an upper bound for the integral length scale the

Lie-group analysis predicts a deceleration wave like solution. For this case the measurements confirm that the behavior changes to a logarithmic law with $H \propto \ell_c ln(t - t_0) + y_0$ and the results also indicate that ℓ_c and y_0 increase with the confinement length, D, however additional measurements are necessary to clarify these trends.

- A finite domain solution is predicted for case (iii) when rotation is applied to the system. For this case the measurements confirm the theory only in the sense that turbulence remains confined within a finite domain. We note that the size of the three-dimensional turbulent flow decreases with increasing angular velocity.

From the analysis of 3D-PTV results on turbulence under the influence of system rotation we conclude that

- Rotation was found to cause a structural change in the sense that after a distance y^* the flow pattern becomes quasi-2D in the sense that the orientation of the velocity vector becomes primarily normal to the rotation axis. The transition to the quasi-2D regime was observed to occur at a local Rossby number on the order of 0.3. Thus the distance y^* depends on both forcing and rotational velocity. The pattern of this quasi-2D flow is dominated by columnar vortex structures, which are aligned with the vertical axis.

- The results show that system rotation influences the two velocity components in different ways. While the magnitudes of the horizontal velocity component increases in the quasi-2D region of the flow, the vertical component of velocity is strongly suppressed.

- Alignment between (i) the velocity and the axis of rotation, (ii) vorticity and the axis of rotation and (iii) the Lagrangian and Coriolis acceleration were found. We find that in the quasi-2D region the orientation of the velocity vector becomes primarily normal to the axis of rotation, vorticity is predominantly aligned with the axis of rotation and the acceleration of fluid particles is preferentially aligned with the Coriolis acceleration.

- The transition from the 3D turbulent flow where the angles between the vectors are random to the quasi-2D flow where they are aligned is gradual. This transition is thus different from the turbulent/non-turbulent interface, which is associated with steep gradients in several flow quantities like the vorticity.

- On closer examination also the 3D region has some imprints from system rotation.

- On the level of small scale quantities both the magnitudes of enstrophy and strain decrease in the quasi-2D region of the flow but still satisfy the relation $< \omega^2 >= 2 < s^2 >$, which is known for homogeneous turbulent flows. Also, vortex stretching occurs less, while vortex compression

increases in proportion in the quasi-2D region of the flow. The positive skewness of the Λ_2-PDF, which is characteristic for 3D-turbulence is only present in the proximity of the grid and almost disappears in the quasi-2D regime.

- A closer examination of the quasi-2D regime shows three qualitatively distinct regions: (i) the core of the vortex columns, (ii) the outer region of the vortex columns and (iii) the flow in between the columnar structures.
- When the alignments in the flow are conditioned on Γ_1 they show the pattern of the columnar structures and confirm that fluid is transported upwards in cyclonic and downwards in anti-cyclonic vortex columns due to Ekman pumping. The alignments between the vorticity vector and the axis of rotation also demonstrate that the flow in the intermediate regions remains 3D.
- In the quasi-2D region of the flow high magnitudes of enstrophy are concentrated in the center of the vortex columns while high magnitudes of strain are present in the region between the columns.
- The positive skewness of the Λ_2-PDFs, which is characteristic for 3D-turbulence, is strongly reduced not only in the region occupied by the vortex columns but also in between. Vortex compression and hence the magnitude of enstrophy destruction are approximately as high as the magnitude of enstophy production in the core and even slightly higher than the magnitude of enstrophy production in the outer region of the columnar structures.
- The results show that the magnitude of system rotation influences the two magnitudes of the velocity components in different ways. While an increase in Coriolis force causes the magnitudes of the horizontal velocity component to increase, the vertical component of velocity is equally suppressed for different rotational velocities. The alignments in the flow increase with the rotational velocity. Further results on the level of small scales are a decrease in vortex stretching and an increase in vortex compression with increasing magnitude of angular velocity.

References

Ashurst, W., Kerstein, A., Kerr, R., and Gibson, C. (1987). Alignment of vorticity and scalar gradients with strain rate in simulated Navier-Stokes turbulence. *Phys. Fluids*, 30:2343–2353.

Bisset, D., Hunt, J., and Rogers, M. (2002). The turbulent / non-turbulent interface. *J. Fluid Mech.*, 451:383–410.

Davidson, P. A. (2007). *Turbulence, An Introduction For Scientists And Engineers*. Oxford University Press.

Davidson, P. A. and Graham, W. R. (2003). Evolution of a vortex in a rotating conducting fluid. *J. Fluid Mech.*, 493:181–190.

Davidson, P. A., Staplehurst, P. J., and Dalziel, S. (2006). On the evolution of eddies in a rapidly rotating system. *J. Fluid Mech.*, 557:135–144.

Dickinson, S. and Long, R. (1978). Laboratory study of the growth of a turbulent layer of fluid. *Phys. Fluids*, 21(10):1698Ű–1701.

Dickinson, S. and Long, R. (1982). Oscillating-grid turbulence including effects of rotation. *J. Fluid Mech.*, 126:315–333.

Feynman, R. P., Leighton, R. B., and Sands, M. L. (1963). *The Feynman Lectures on Physics, Vol. 1.* Addison-Wesley.

Godeferd, F. and Lollini, L. (1998). Direct numerical simulations of turbulence with confinement and rotation. *J. Fluid Mech.*, 393:257–308.

Guala, M., Liberzon, A., Hoyer, K., Tsinober, A., and Kinzelbach, W. (2008). Experimental study of clustering of large particles in homogeneous turbulent flow. *J. of Turbulence*, 9(34):1–20.

Heijst, G. and Clercx, H. (2007). Two-dimensional turbulence on a confined domain with no-slip walls. *Advances in Turbulence*, 11:159–163.

Holzner, M., , Lüthi, B., Kinzelbach, W., and Tsinober, A. (2009). Acceleration, pressure and related quantities in the proximity of the turbulent/nonturbulent interface. *J. Fluid Mech.*, 639:153–165.

Holzner, M., Liberzon, A., Guala, A., Tsinober, A., and Kinzelbach, W. (2006). Generalized detection of a turbulent front generated by an oscillation grid. *Exp. In Fluids*, 41(5):711–719.

Holzner, M., Liberzon, A., Nikitin, N., Kinzelbach, W., and Tsinober, A. (2007). Small scale aspects of flow in proximity of the turbulent/nonturbulent interface. *Phys. of Fluids*, 19, 071702.

Hopfinger, E. J., Browand, F. K., and Gagne, Y. (1982). Turbulence and waves in a rotating tank. *J. Fluid Mech.*, 125:505–534.

Hopfinger, E. J. and Toly, J. A. (1976). Spatially decaying turbulence and its relation to mixing across density interfaces. *J. Fluid Mech.*, 78:155–177.

Hoyer, K., Holzner, M., Lüthi, B., Guala, M., Liberzon, A., and Kinzelbach, W. (2005). 3D scanning particle tracking. *Exp. In Fluids*, 39(7):923–934.

Hunt, J. C. R., Eames, I., and Westerweel, J. (2006). Mechanics of inhomogeneous turbulence and interfacial layers. *J. Fluid Mech.*, 554:449–519.

Hurst, D. and Vassilicos, J. (2007). Scaling and decay of fractal-generated turbulence. *Phys. Fluids*, 19, 035103.

Kolmogorov, A. (1941a). Dissipation of energy in locally isotropic turbulence,. *Dokl. Akad. Nauk SSSR*, 32:19–21.

Kolmogorov, A. (1941b). The local structure of turbulence in incompressible viscous fluid for very large Reynolds numbers. *Dokl. Akad. Nauk SSSR*, 30:299–303.

Liberzon, A., Holzner, M., Lüthi, B., Guala, M., and Kinzelbach, W. (2009). On turbulent entrainment and dissipation in dilute polymer solution. *Phys. Fluids*, 21:035107.

Long, R. (1978). Theory of turbulence in a homogeneous fluid induced by an oscillating grid. *Phys. Fluids*, 21(10):1887–1888.

Lüthi, B. (2002). *Some Aspects of Strain, Vorticity and Material Element Dynamics as Measured with 3D Particle Tracking Velocimetry in a Turbulent Flow.* PhD Thesis.

Lüthi, B., Tsinober, A., and Kinzelbach, W. (2005). Lagrangian measurement of vorticity dynamics in turbulent flow. *J. Fluid Mech.*, 528:87–118.

Maas, H. (1996). Contributions of digital photogrammetry to 3D PTV. *Three-dimensional Velocity and Vorticity Measuring and Image Analysis Techniques.*

Maas, H., Gruen, D., and Papantoniou, D. (1993). Particle tracking velocimetry in three-dimensional flows. *Exp. In Fluids*, 15:133Ű146.

Melling, M. (1997). Tracer particles and seeding for particle image velocimetry. *Meas, Sci. Technol.*, 8:1406–1416.

Messio, L., Morize, C., Rabaud, M., and Moisy, F. (2008). Experimental observation using particle image velocimetry of inertial waves in a rotating fluid. *Exp. In Fluids*, 44:519–528.

Michard, M., Graftieaux, L., Lollini, L., and Grosjean, N. (1997). Identi cation of vortical structures by a non-local criterion: Applications to p.i.v. measurements ans d.n.s results of turbulent rotating flows. *Proc. Eleventh Symp. on Turbulent Shear Flows, Grenoble.*

Mininni, P. D., Alexakis, A., and Pouquet, A. (2009). Scale interactions and scaling laws in rotating flows at moderate Rossby numbers and large Reynolds numbers. *Phys. Fluids*, 21:015108.

Morize, C. and Moisy, F. (2006). Energy decay of rotating turbulence with confinement effects. *Phys. Fluids*, 18:065107.

Morize, C., Moisy, F., and Rabaud, M. (2005). Decaying grid-generated turbulence in a rotating tank. *Phys. Fluids*, 17:095105.

Nobach, H. and Bodenschatz, E. (2009). Limitations of accuracy in PIV due to individual variations of particle image intensities. *Exp. In Fluids*, 47:27–38.

Oberlack, M. and Günther, S. (2003). Shear-free turbulent diffusion, classical and new scaling laws. *Fluid Dynamics Research*, 33:453–476.

Pedlosky, J. (1987). *Geophysical Fluid Dynamics*. Springer-Verlag.

Pope, S. B. (2000). *Turbulent Flows*. Cambridge University Press.

Raffel, M., Willert, C., and Kompenhans, J. (1998). *Particle Image Velocimetry: A Practical Guide*. Springer-Verlag, Heidelberg.

Ruppert-Felsot, J. E., Proud, O., Sharon, E., and Swinney, H. L. (2005). Extraction of coherent structures in a rotating turbulent flow experiment. *Physical Review*, E72:16311.

Savas, O. (1985). On flow visualisation using reflective flakes. *J. Fluid Mech.*, 152:235–248.

Scorer, R. S. (1978). *Environmental Aerodynamics*. Halsted Press, New York.

Siggia, E. (1981). Numerical study of small-scale intermittency in three-dimensional turbulence. *J. Fluid Mech.*, 107:375–406.

Silva, I. D. and Fernando, H. (1994). Oscillating grids as a source of nearly isotropic turbulence. *Phys. Fluids*, A 6(7):2455–2464.

Squires, K., Chasnov, J., Mansour, N., and Cambon, C. (1994). The asymptotic state of rotating homogeneous turbulence at high reynolds number. *74th Fluid Dynamics Symposium, on "Application of Direct and Large Eddy Simulation to Transition and Turbulence"*, 74:4–1.

Thompson, S. and Turner, J. (1975). Mixing across an interface due to turbulence generated by an oscillating grid. *J. Fluid Mech.*, 76:349.

Townsend, A. A. (1976). *The Structure of Turbulent Shear Flow*. Cambr. Univ. Press.

Tropea, C., Yarin, A., and Foss, J., editors (2007). *Handbook of Experimental Fluid Mechanics*. Springer.

Tsinober, A. (1998). Is concentrated vorticity that important? *Eur. J. Mech., B/Fluids*, 17:421–449.

Tsinober, A. (2001). *An Informal Introduction to Turbulence*. Kluwer Academic Publishers.

van Bokhoven, L., Clercx, H., van Heijst, G., and Trieling, R. (2009). Experiments on rapidly rotating turbulent flows. *Phys. Fluids*, 21:096601.

Vieillefosse, P. (1982). Local interaction between vorticity and shear in a perfect incompressible fluid. *le journal de physique*, 43:837–842.

Westerweel, J., Hoffmann, T., Fukushima, C., and Hunt, J. (2002). The turbulent/non-turbulent interface at the outer boundary of a self similar jet. *Exp. In Fluids*, 33:873–878.

A Theoretical Background

In the following the theoretical results of the Lie-Group analysis will be briefly outlined and the relevant equations will be written in normalized form to allow for comparison to the experimental data. For further details the reader is referred to Oberlack and Günther (2003) and references therein. Three different similarity solutions, generally called group invariant solutions, will be briefly outlined. However, we will be limiting the presented results to the two-point correlation tensor $R_{ij}(\mathbf{r},\mathbf{x},t) = \overline{u_i'(\mathbf{x},t)u_j'(\mathbf{x}+\mathbf{r},t)}$. For the present flow geometry R_{ij} only depends on $\mathbf{r}$, t and y, where y is the direction normal to the source of energy. In all of these cases the latter set of five independent variables is reduced to four. It is important to note that these similarity solutions, in turbulence usually called scaling laws, are valid for the infinite set of multi-point correlations.

Oberlack and Guenther derived first (i) a diffusion like solution for the case in which the turbulence can diffuse freely into the adjacent fluid at rest. The similarity form for R_{ij} yields

$$\begin{aligned} R_{ij}(y,t,\boldsymbol{r}) &= (y-y_0)^{-2m}\tilde{R}_{ij}(\widetilde{y},\tilde{\boldsymbol{r}})\,, \ \text{with} \\ \widetilde{y} &= \frac{y-y_0}{(t-t_0)^{1/(m+1)}}\,, \ \ \tilde{\boldsymbol{r}} = \frac{\boldsymbol{r}}{y-y_0}\,, \end{aligned} \tag{26}$$

where here and in all subsequent cases $\tilde{R}_{ij}$ refers to the new dependent variable, the constants y_0 and t_0 label the two virtual origins of space and time and m is a measure of the decay rate. All of them are to be determined e.g. from boundary conditions. Results for both one-point quantities as well as for the statistics of the TNTI evolution may be determined from (26). In the limit $t \to \infty$ the Reynolds stresses $\overline{u_i'u_j'}$ and the integral length scale

$$\ell = \frac{1}{K}\int_{V_r} R_{kk}\mathrm{d}\Omega\mathrm{d}r \tag{27}$$

reduce to

$$\begin{aligned} \overline{u_i'u_j'}(y) &= (y-y_0)^{-2m}\mathcal{C}_{ij}^{alg} \ \text{ and} \\ \ell(y) &= \gamma_1(y-y_0), \end{aligned} \tag{28}$$

where K represents the total turbulent kinetic energy, Ω is the solid angle and $\mathcal{C}_{ij}^{alg}$ and γ_1 are constants.

In order to understand the statistics of the TNTI evolution from (26) we may normalize R_{ij} in equation (26) using the factor $(y-y_0)^{-2m}$. Even without knowing the detailed form of the function we may physically deduce that $\tilde{R}_{ij}$ is a ramp-like function which is constant from $\widetilde{y} \geq 0$ until a smooth transition region - the statistics of the TNTI - and from then on converging to zero for $\widetilde{y} \to \infty$. From the definition of $\widetilde{y}$ we observe that the position of the TNTI, subsequently denoted by $H(t)$, moves in positive y direction according to an

algebraic or power law

$$H^{alg}(t) = \alpha \ell_0 \left[\frac{(t-t_0)\sqrt{K_0}}{\ell_0} \right]^{1/(m+1)} + y_0, \tag{29}$$

where α is a constant and ℓ_0 and $\sqrt{K_0}$ are a length and velocity scale used to obtain a dimensionally correct scaling law. It is natural to use the integral length scale and turbulent kinetic energy in the proximity of the grid to determine ℓ_0 and $\sqrt{K_0}$ respectively.

The second case (ii) represents a deceleration wave like solution most concisely characterized by the constant integral length scale downstream of the grid. The similarity form for R_{ij} is given by

$$\begin{aligned} R_{ij}(y,t,\boldsymbol{r}) &= \mathrm{e}^{-2\frac{y}{\ell_c}} \tilde{R}_{ij}(\widetilde{y},\tilde{\boldsymbol{r}}), \text{ with} \\ \widetilde{y} &= y - \ell_c \ln(t-t_0), \ \tilde{\boldsymbol{r}} = \boldsymbol{r}, \end{aligned} \tag{30}$$

Considering the limit $t \to \infty$ and similarly to case (i) we derive the one-point quantities

$$\begin{aligned} \overline{u_i' u_j'}(y) &= \mathrm{e}^{-2\frac{y}{\ell_c}} \mathcal{C}_{ij}^a \text{ and} \\ \ell(y) &= const., \end{aligned} \tag{31}$$

with $\mathcal{C}_{ij}^a$ being a constant tensor of dimension velocity squared. Here ℓ_c is supposed to be proportional to the integral length scale, which, as shown below, is also proportional to the constant external length scale that prevents the integral length scale from growing. In the experiment this is realized by implementing a tube with a given diameter below the oscillating grid. Note that due to the exponential form of $\overline{u_i' u_j'}$ the spatial off-set is hidden in $\mathcal{C}_{ij}^a$ or in $\tilde{R}_{ij}$ in (30).

As above in case (i) the statistics of the TNTI are to be deduced from $\widetilde{y}$. Again ℓ_c and $\sqrt{K_0}$ are utilized to derive a dimensionally correct TNTI scaling law. Hence we may derive the corresponding scaling behavior

$$H^{log}(t) = \beta \ell_c \ln \left[\frac{(t-t_0)\sqrt{K_0}}{\ell_c} \right] + y_0, \tag{32}$$

where β is a constant. In the last case (iii) a "finite turbulence domain solution" has been observed by Oberlack and Günther (2003) for the case when rotation is applied to the system revolving about the direction of diffusion. Here an external time scale is given by the frame rotation ($\tau_\Omega = 1/\Omega_1$). In this case we have the similarity solution

$$\begin{aligned} R_{ij}(y,t,\boldsymbol{r}) &= (y-y_0)^2 \tilde{R}_{ij}(\widetilde{y},\tilde{\boldsymbol{r}}), \text{ with} \\ \widetilde{y} &= (y-y_0)\mathrm{e}^{-\frac{t}{\tau}}, \ \tilde{\boldsymbol{r}} = \frac{\boldsymbol{r}}{y-y_0} \dots, \end{aligned} \tag{33}$$

where τ is supposed to be proportional to τ_Ω. In the limit of $t \to \infty$ we obtain the one-point quantities

$$\begin{aligned} \overline{u_i' u_j'}(y_1) &= (y-y_0)^2 \mathcal{C}_{ij}^b \text{ and} \\ \ell(y) &= \gamma_2 (y-y_0). \end{aligned} \tag{34}$$

Similarly to the two cases above we employ $\widetilde{y}$ for the TNTI statistical scaling law. For this an additional length scale is needed which is to be taken from the given time-scale τ_Ω and, as above, the velocity scale is determined by the turbulent kinetic energy at the grid K_0

$$H(t)^{exp} = \delta\tau_\Omega\sqrt{K_0}\exp(-\varphi t/\tau_\Omega) + y_0, \tag{35}$$

where δ and φ are constants.

B Further Checks

B.1 Acceleration Checks

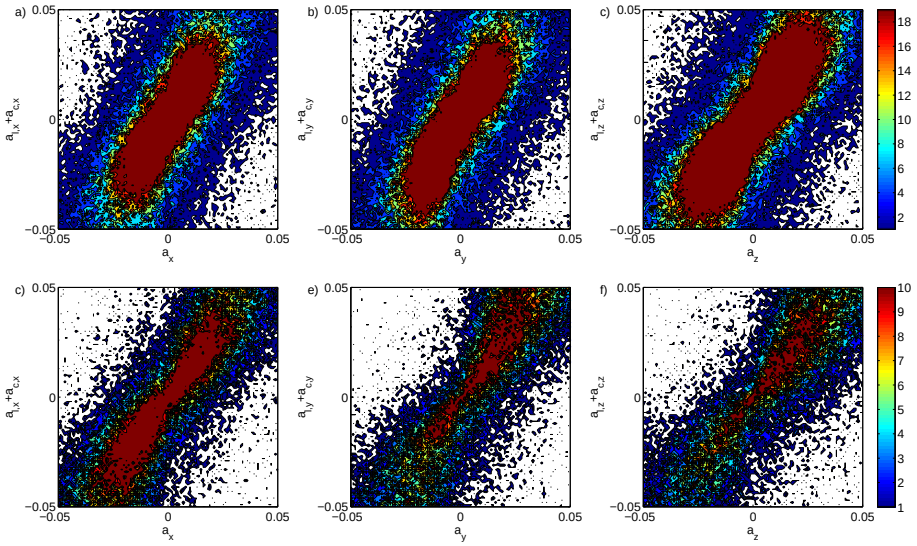

Figure 61: Joint pdf of $a_{l,i}$+$a_{c,i}$ versus a_i for i=x, y, z for the large (top) and the small observation volume (bottom) in the Eulerian frame.

B.2 Comparison Between the Large and the Small Observation Volume

The accuracies, which were achieved in the different observation volumes was discussed in section 2.5. Now the influence of these accuracies on the results obtained for the main flow quantities as well as for the alignments in the flow shall be addressed. This is important since these alignments had to be computed from the data of the large observation volume in order to resolve the change over distance from the grid, y in the previous section, section 3.2.3. However, these results are effected by the coarse spatial resolution of the large observation volume. Therefore PDF of the flow quantities discussed in section 3.2.3 are calculated from the data measured in the small observation volume and from the corresponding area of the large observation volume from an experiment in which both data sets were measured simultaneously. The experiment was conducted at a rotational velocity of 3.14 rad/s thus the alignments due to the rotation, which were illustrated earlier are pronounced. PDF of the magnitude of the horizontal and vertical velocity obtained in the small (.) and the corresponding region in the large observation volume (-) are compared in Figure 64 a and b, respectively. Since the curves were measured in the two different observation volumes the

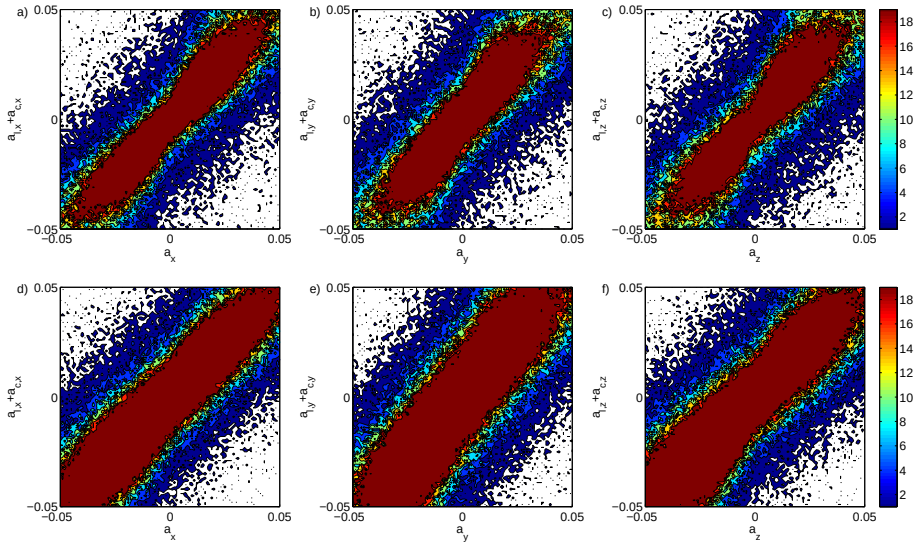

Figure 62: Joint pdf of $a_{l,i}+a_{c,i}$ versus a_i for i=x, y, z for the large (top) and the small observation volume (bottom) from a simultaneous two-scale measurement in the Lagrangian frame.

spatial resolution of both data sets is different. The PDF in Figure 64 show that there is a good quantitative agreement between the two data sets on the level of velocities despite the different spatial resolution. The same comparison is done for the PDF of the magnitude of acceleration in Figure 65. While these PDF agree on a qualitative level the magnitude of accelerations measured in the large observation volume are higher. A likely explanation is the lower spatial resolution, which misses events with low acceleration.

The effect of the spatial resolution on the geometric alignments becomes apparent when PDFs of the cosine between the velocity vector and the axis of rotation (Figure 66 a) and the vorticity vector and the axis of rotation (Figure 66 b) are displayed for data from the small (.) and the corresponding region of the large observation volume (-). The PDFs of the former show a good quantitative agreement between the data obtained in large and small observation volume, since the curves of Figure 66 (a) lie almost exactly on top of each other. For the alignment of vorticity with the axis of rotation on the other hand there is only a qualitative agreement between the large and the small observation volume because the data from the large volume seems to overestimate the alignment of the vorticity vector with the axis of rotation. This is presumably due to the under-resolution in the large observation volume, since a coarse-grained measurement of vorticity is only able to capture the vorticity of the large scale columnar vortices, which is expected to show a strong alignment with the axis of rotation. The last two alignments for which the influence of the spatial resolution is checked are the cosine between Lagrangian and Coriolis acceleration in Figure 67 (a) and the cosine between the vortex stretching

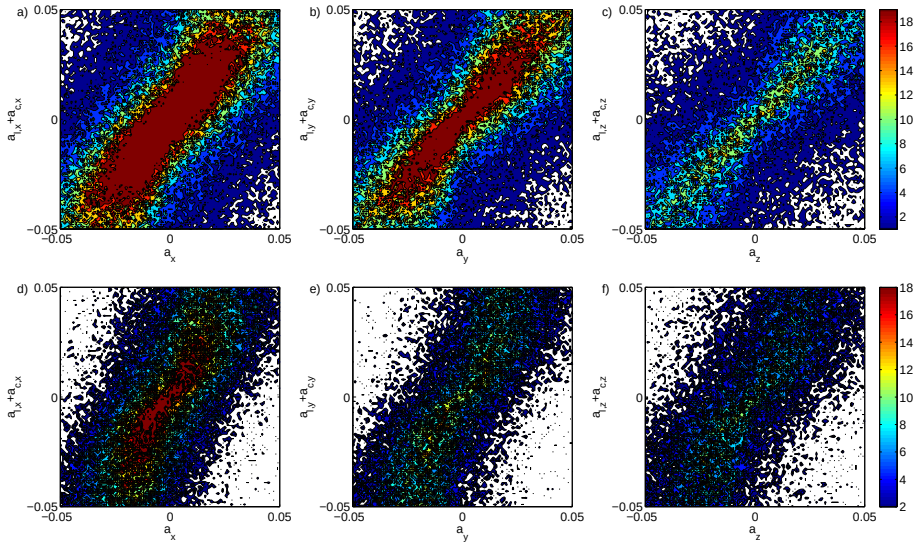

Figure 63: Joint pdf of $a_{l,i}+a_{c,i}$ versus a_i for i=x, y, z for the large (top) and the small observation volume (bottom) from a simultaneous two-scale measurement in the Eulerian frame.

vector and the vorticity in Figure 67 (b). The PDF of the former agree well, also on a quantitative level. This suggests that small scale quantities, which are obtained along particle trajectories, i.e., in the Lagrangian frame (e.g., the Lagrangian acceleration) are also resolved well in the large observation volume. The Coriolis acceleration, $a_{cl} = u \times \Omega$, is based on large scale quantities and can thus be measured reliably in the large observation volume as well. The alignment between the vortex stretching vector and the vorticity is again over predicted in the large observation volume, which shows that the small scale information which involve spatial derivatives between different particle trajectories can not be captured accurately with the low spatial resolution of the large observation volume. Nevertheless, the qualitative agreement between the two different spatial resolutions is clearly there.

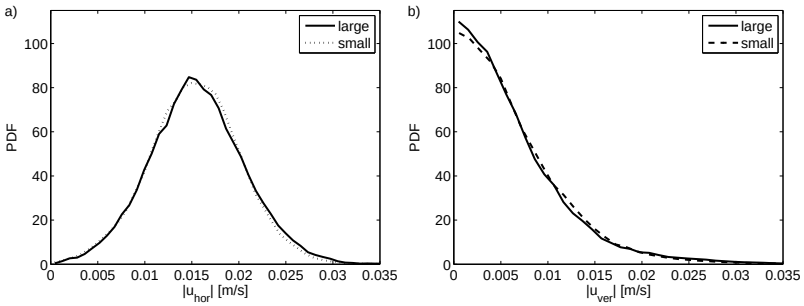

Figure 64: PDF of the magnitude of horizontal (a) and vertical (b) velocity measured in the small (dashed) and the corresponding region in the large (solid) observation volume

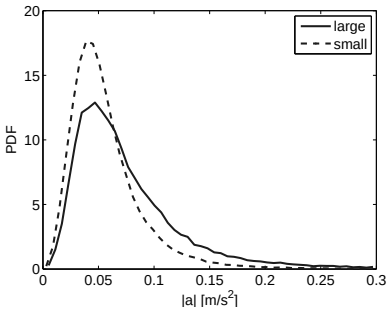

Figure 65: PDF of the magnitude of acceleration measured in the small (dashed) and the corresponding region in the large (solid) observation volume

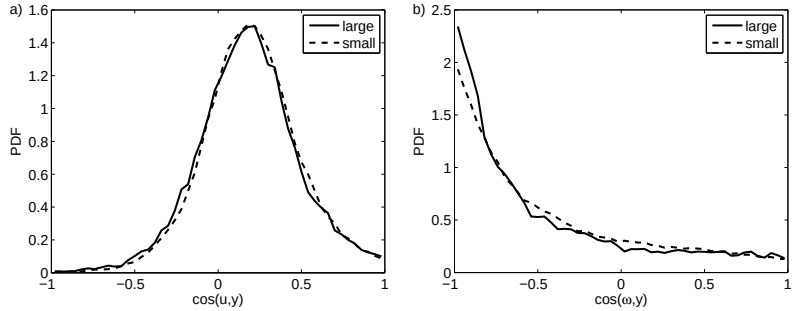

Figure 66: PDF of the cosine between the velocity (a) and vorticity (b) vector and the axis of rotation measured in the small (dashed) and the corresponding region in the large (solid) observation volume

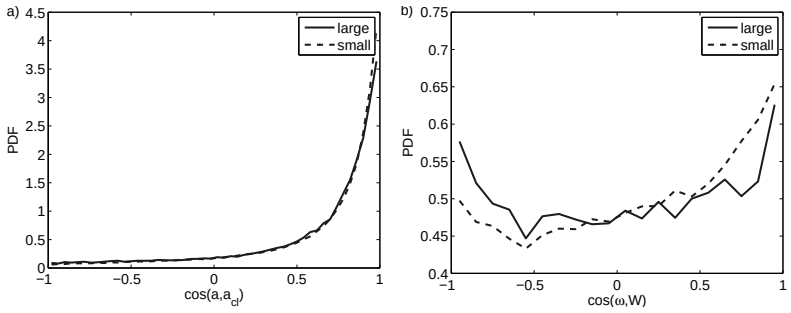

Figure 67: PDF of the cosine between the Lagrangian and Coriolis acceleration (a) and the vortex stretching vector and vorticity (b) measured in the small (dashed) and the corresponding region in the large (solid) observation volume

Matthias Kinzel

Technische Universitaet Darmstadt
Fluid Mechanics and Aerodynamics
Petersenstrasse 30
64287 Darmstadt

Phone: +49 6151 16-3354
Fax: +49 6151 16-4754
Email: m.kinzel@sla.tu-darmstadt.de

Personal

Born on June 05, 1982

German

Education

12/2006–03/2010, Ph.D. in Mechanical Engineering, Technische Universitaet Darmstadt, Darmstadt, Germany

11/2003–11/2006, M.Sc. in Mechanical Engineering, Technische Universität Darmstadt, Darmstadt, Germany

10/2005–04/2006, Semester abroad for Dipl.-Ing research project, Cornell University, Ithaca, USA

10/2001–10/2003 cand. Ing. in Mechanical Engineering Technische Universität Darmstadt, Darmstadt, Germany

Employment

2010–present, postdoctoral scholar at the California Institute of Technology, Pasadena, USA

05/2006–10/2006 Internship at Rolls Royce, Dalewitz, Germany

01/2005–04/2005 Research assistant at Institute of Fluid Mechanics and Aerodynamics, Technische Universitaet Darmstadt, Darmstadt, Germany

05/2004–12/2004 Research assistant at Institute of Gas Turbines and Aerospace Propulsion, Technische Universitaet Darmstadt, Darmstadt, Germany

07/2003–08/2003 Internship at Hasenclever & Sohn, Battenberg, Germany